Device, Interface, Process and Electrode Engineering Towards Low Cost and High Efficiency Polymer Solar Cells in Inverted Structure

JINGYU ZOU

A DISSERTATION

SUBMITTED IN PARTIAL FULFILLMENT OF THE

REQUIREMENTS FOR THE DEGREE OF

DOCTOR OF PHILOSOPHY

Reading Committee:

Alex K.-Y. Jen, Chair

Fumio Ohuchi

Marco Rolandi

Program Authorized to Offer Degree:

Materials Science and Engineering

Abstract

As a promising technology for economically viable alternative energy source, polymer solar cells (PSCs) have attracted substantial interests and made significant progress in the past few years, due the advantages of being potentially easily solution processed into large areas, flexible, light weight, and have the versatility of material design. In this dissertation, an integrated approach is taken to improve the overall performance of polymer solar cells by the development of new polymer materials, device architectures, interface engineering of the contacts between layers, and new transparent electrodes.

First, several new classes of polymers are explored as potential light harvesting materials for solar cells. Processing has been optimized and efficiency as high as 6.24% has been demonstrated. Then, with the development of inverted device structure, which has better air stability by utilizing more air stable, high work function metals, newly developed high efficiency polymers have been integrated into inverted structure device with integrated engineering approach.

A comprehensive characterization and optical modeling based on conventional and inverted devices have been performed to understand the effect of device geometry on photovoltaic performance based on a newly developed high performance polymer poly(indacenodithiophene-*co*-phananthrene-quinoxaline) (PIDT-PhanQ). By modifying anode with a bilayer combining graphene oxide (GO) and poly(3,4-ethylenedioxylenethiophene):poly(styrenesulfonic acid) (PEDOT:PSS) as hole transporter/electron blocker, it further improved device performance of inverted structured to 6.38%.

A novel processing method of sequentially bilayer deposition for active layer has been conducted based on a low band-gap polymer poly[2, 6-(4, 4-bis-(2-ethylhexyl)-4*H*-cyclopenta

[2,1-b;3,4-*b*′] dithiophene)-*alt*-4,7-(2, 1, 3- fluorobenzothiadiazole)] (PCPDT-FBT). Inverted structure devices processed from bilayer deposition shows even higher performance than bulk-heterojunction. Polymer and fullerene distribute uniformly throughout the layer in vertical direction. Better electron mobility and better crystallinity in inverted bilayer film bas been observed, which can contribute to the higher IQE in inverted bilayer device.

Metal grid/conducting polymer hybrid transparent electrode has been proved can be an alternative to ITO in inverted structure with similar device performance. Further, a novel protocol to fabricate highly transparent ultra thin silver films as transparent electrode on both glass and plastic substrates also has been demonstrated, based on ZnO/Ag/ZnO tri-layer structure and self-assembled monolayer interfacial modification. Sophisticated interfacial engineering method is applied at necessary interfaces to functioning the ultra thin silver film as a platform for polymer solar cells, and superior device performance that even exceeds using ITO has been achieved.

Acknowledgments

I would like to thank Professor Alex Jen for his support and training throughout my Ph.D. studies. I am thankful for all the resources and guidance that he has provided to allow me to conduct my research her at the University.

I would like to thank Dr. Hin-Lap Yip for his discussions and suggestions on improving the quality and success of my projects.

Thanks to Professor Fumio Ohuchi and Professor David Ginger for allowing me to preform experiments in their laboratory. I am appreciative of Xiaohao Zheng for his help and discussion on X-ray photoelectron spectroscopy measurements.

I am truly grateful for all the past and present Jen Group members who have made this journey a memorable one. Dr. Steven Hau, Dr. Kirsty Leong, Dr. Su Huang, Dr. Orb Acton, Dr. Yong Zhang, Dr. Chang-Zhi Li, Dr. Chu-Chen Chueh, Dr. Jingdong Luo, Dr. Sei-Hum Jang, Dr. Hong Ma, Dr. Zhengwei Shi, Dr. Zhongan Li, Dr. Shane Boyd, Dr. Jeremy Intemann, Dr. Yunxiang Xu, Dr. Ying Wang, Dr. Chih-Yu Chang, Kung-Shih Chen, Kevin O'Malley, Guy Ting, NamChul Cho, You-Jung Cheng, Yongxi Li, Xi Yang, Yan Gao, Ying Sun, Nathan Cernetic, Lijian Zuo. This journey would not have been the same without you all being here as a strong support system.

Thanks to Professor Fumio Ohuchi and Professor Marco Rolandi for their comments and critiques of this dissertation.

Thanks Dr. Alec Pakhomov at the Nanotechnology User Facility for his assistance in helping me with x-ray diffraction and ellipsometry measurements. For

I would like to thank the financial support provided by the following funding agencies in helping me achieve my research goals: National Science Foundation (DMR-0120967), the

Department of Energy (DE-FC3608GO18024/A000), the Air Force Office of Scientific Research (FA9550-09-1-0426), the Asian Office of Aerospace R&D (FA2386-11-1-4072), Office of Naval Research (N00014-11-1-0300).

I would like to thank all my friends in Seattle, WA who have helped make this entire graduate experience more pleasurable: Yeping Yuan, Ling Luo, Wei Shi, Kaishi Wang, Jin Wang, Pinyi Yang, Yufeng Hou, Xiaoji Chen, Qianru Deng, Yuan Gao, Xiaoyue Zheng, Angke Chen, Jiaxing Li, Hong Chen, Jing Hong, Yuting Lin, Wenjun Jiang, Yan Huang, Ruichan Shao, Xuan Wang, Yingxin Deng.

More than everything, I would like to thank my parents for all their love and support throughout this process, my father, Yongsheng Zou, and my mother, Hongyan Zhang, A special thanks to my husband for his love, support, encouragement and understanding throughout the entire process of graduate school.

Chapter 1. INTRODUCTION

1.1 INTRODUCTION

The continued depletion of fossil fuel energy resources has led to the rise in energy production costs on the global scale. [1]–[3] Currently, the continuous power consumption is over 13 terawatts (TW) in a year in the world and its demand is continuing to grow. Because of the dilemma, the growing concern for economically viable alternative energy sources has become more apparent. One alternative energy source of particular interest is solar energy. The limitless energy from the sun may be utilized for its conversion to electrical energy. The amount of energy generated by the sun in one hour of sunlight is the enough to supply the entire global energy consumption for the year. Research efforts have significantly increasing in finding, developing and processing new materials and device structure for the efficient conversion of solar energy to electricity.

Solar energy technologies include solar thermal systems and photovoltaic. Photovoltaic cells are semiconductor devices that convert light directly to electricity. Comparing with solar thermal systems, photovoltaic cells have several advantages, such as the ability to work under diffuse light, scalable installation, and well suited for distributed application.[1] However, it is not economical competitive enough with traditional energy sources. In order to meet the U.S. Department of Energy cost goal of \$0.33/W or \$0.05-0.06/KWh for utility-scale production, PV modules would need to be manufactured at a cost of \$50/m^2 or less. [4]

1.2 BASIC PHOTOVOLTAIC SOLAR CELL CONCEPT AND PARAMETERS

The photovoltaic (PV) cell is an electrical diode that generates additional current when it is illuminated with light. Solar cells and modules are usually characterized according to the IEC norm under standard test conditions, which correspond to 1kW/m^2 (100mW/cm^2) direct

perpendicular irradiance under a air mass 1.5 global (AM 1.5G) spectrum at 25°C cell temperature. The AM 1.5G spectrum is the standard solar spectrum (Figure 1-1) at sea level taking into account absorption from oxygen and nitrogen that hits the earth's surface at an oblique angle of 48.2° from the zenith.[5]

The mechanism in a photovoltaic cell can be described as follow: (1) light absorbed by the material, (2) spatial separation of holes and electrons generated by the light in the material, (3) charges has been collected by the electrode to generate current.

The active material in the photovoltaic cell is the material that absorbs light, and it will only absorb photons which have energy larger than its bandgap. When light is absorbed in a semiconductor, the incoming photo will excited the electron from the valence band to the conduction band, and leaves behind a hole in the valence band. If these two charges can be separate efficiently, they will move to the opposite sides of the cell, and be collected by the electrode to produce current. The efficiency of light absorption, charge generation, separation and collection determines the power conversion efficiency (PCE) of PV cell.

The PCE of the cell is the power density delivered at operation point as a fraction of the incident light power density, P_0, and is characterized by three key performance parameters, open circuit voltage (V_{oc}), short circuit current density (J_{sc}) and fill factor (FF) as:

$$\eta_{PCE}=\frac{V_{oc}\times J_{sc}\times FF}{P_o}\times 100 \qquad \textit{Equation-1}^{[5]}$$

Figure 1-2 shows current density-voltage (J-V) curves of a PV cell and its performance parameters. The open circuit voltage is the point where current is equal to zero or where there is no current flow; the short circuit current is the photo-induced current produced by illumination and is the point at which the voltage is equal to zero; and the fill factor is defined as the ratio of

the area of maximum power generated to the area of the area of the Voc×Jsc, which is given by the equation:

$$FF = \frac{J_m V_m}{J_{sc} V_{oc}} \qquad \textit{Equation 1-2}$$

which describes the 'squareness' of the J-V curve. In order to have an efficient device, the V_{oc}, J_{sc}, and FF must be optimized and increased.

Shunt resistance (R_{sh}), also known as parallel resistance (R_p), and series resistance (R_s) are another two important parameters for PV cell characterization. For an ideal diode, $R_{sh}=\infty$ and $R_s=0$. Therefore, maximizing the R_{sh} and minimizing R_s of PV cell will be important to achieve high performance devices.

Except the current-voltage characteristic of PV, another important characterization for solar cells is external quantum efficiency (EQE), which is the measure of how efficient incoming photons at a given wavelength are being converted to electron. The integral of the EQE multiplied by the AM1.5 spectrum should match the short circuit current output of PV cell.

The current-voltage (I-V) characteristics of photovoltaic devices usually measured in laboratory with a solar simulator with an AM1.5 G filter. A reference cell is often used to calibrate the light intensity of the solar simulator, the power of the solar simulator was adjusted to make the short-circuit current (I_{SC}) of the reference cell under simulated sun light as high as it was under the calibration condition. The test solar cell often has a different spectral response with the reference cell, which can lead to errors. The amount of error, referred to the mismatch factors (M) is defined as:

$$M = \frac{\int_{\lambda_1}^{\lambda_2} E_{Ref}(\lambda) S_R(\lambda) d\lambda}{\int_{\lambda_1}^{\lambda_2} E_{Ref}(\lambda) S_T(\lambda) d\lambda} \frac{\int_{\lambda_1}^{\lambda_2} E_S(\lambda) S_T(\lambda) d\lambda}{\int_{\lambda_1}^{\lambda_2} E_S(\lambda) S_R(\lambda) d\lambda}$$ *Equation 1-3*

Where $E_{Ref}(\lambda)$ is the reference spectral irradiance (AM1.5), $E_S(\lambda)$ is the source spectral irradiance, $S_R(\lambda)$ is the spectral responsivity of the reference cell, and $S_T(\lambda)$ is the spectral responsivity of the test cell, each as a function of wavelength (λ). [6]

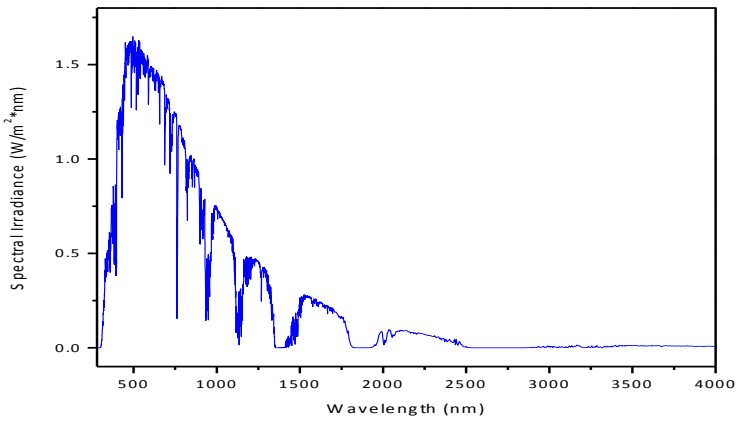

Figure 1-1 Solar spectrum at air mass 1.5G.

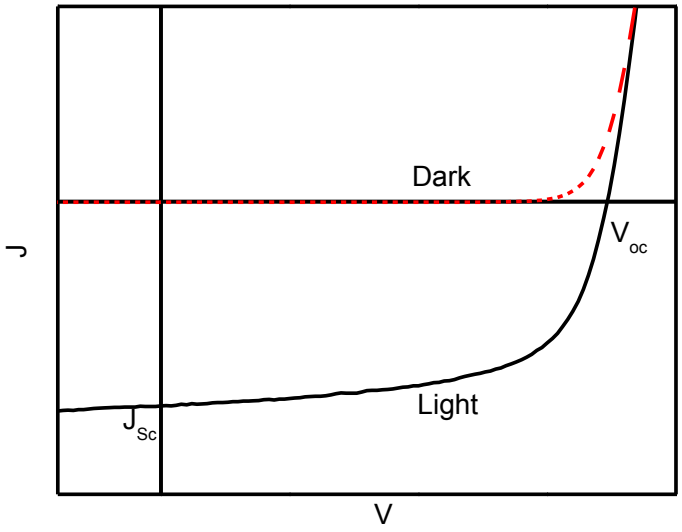

Figure 1-2 Dark and illuminated J-V curves of a typical photovoltaic diode.

1.3 DEVELOPMENT OF POLYMER SOLAR CELLS (PSCS)

PV cells can be categorized into three different types: inorganic solid-state semiconductor cells, photo-electrochemical cells based on interfaces between semiconductors and molecules (dye-sensitized solar cells), and organic based semiconductor solar cells. The organic based semiconductor solar cells also include vacuum deposited small molecules solar cells, and solution processed PSCs. My research is mainly focused on solution processed PSCs.

Polymer based materials have the advantages of being potentially easily solution processed into large areas, inexpensive, light weight, compatible to flexible substrates, and have the versatility of material design. Depending on the demand of applications, PSCs show the potential to be processed onto flexible substrates with large-scale roll-to roll printing process. [1][7][8]

The main difference between organic PV cells and inorganic semiconductors solar cells is organic solar cells do not generate free charge carriers upon photo-excitation, but rather a bound electron-hole pair, which is called exciton, with a binding energy of ~0.2-0.4eV. Exciton can be separated with the presence of high electric field. Such local fields can be supplied via externally applied electrical fields as well as via interfaces, which can provide sufficient energy level offset. At an interface, where abrupt changes of the potential energy occur, strong local electrical fields are possible. Photo-induced charge transfer can occur when the exciton has reached such an interface within its lifetime. Otherwise, excitons decay via radiative or nonradiative pathways (geminate recombination) before reaching the interface, and their energy is lost for power conversion.[9] To provide sufficient band offset at interfaces and increase the charge transport mobility, active layer with two different materials have introduced by C.W.Tang in 1985.[10] Those two different materials should have offset energy band to play a role as so called “donor”, which is a hole transporting materials, and “acceptor”, which is a electron transporting

materials. Exciton diffusion lengths in polymers are usually around 10-20 nm. To efficiently dissociate excitons, the exciton diffusion length should be on the same order of magnitude as the donor acceptor phase separation length. If the exciton dissociates into free charge carriers, the materials will transport the charge carriers to their respective electrodes for charge collection. During the transport, if the different or very low mobility exists between the donor and acceptor materials, then charges may potentially recombine (non-geminate recombination) which will also lead to photocurrent loss. Additionally, energy level needs to be match at interface between active layer and electrode to have a good device performance.

The most basic device structure is based on a single polymer photoactive layer sandwiched between two electrodes. The single layer structure PSCs consists of only one semiconductor materials and is often known as a Schottky type diode in which one of the electrode interfaces is in ohmic contact with the semiconductor, while the other interface has a Schottky contact where the charge separation occurs. The limited absorption from a single semiconductor material and high recombination of charges from the low transport mobility of the charges hinders the performance of single layer structure devices.

The first bilayer heterojunction solar cell was reported by Tang in 1986 with 1% power conversion efficiency (PCE),[20] the bilayer structure is based on a p-type and n-type hetero-junction. In this device structure, exciton generate within 10-20nm of the interface can be separated, and the n-type materials will transport electrons and p-type material will transport holes to electrodes. But the limited interface between donor and acceptor was considered as the disadvantage of the structure to limit the PCE.

Currently, bulk-heterojunction (BHJ), which is a blend of the donor and acceptor components in a bulk volume (Figure 1-3), has been proved to be the most efficient structure and

attract most attention in research. A bulk-heterojunction (BHJ) active layer often consists of a blend of an electron-rich conjugated polymer donor and an electron-deficient fullerene acceptor to form a bi-continuous interpenetrating network via solution processing.[7][8] Compare to the simple planar heterojunction, the BHJ geometry is supposed to provide greater interface area to enhance the dissociation of excitons, with the formation nano-scale phase separation. The nanoscale interpenetrating network increases the interface area between donor and acceptor, thus dramatically increasing the chance of exciton separation. To form the favored phase separation as well as bi-continuous interpenetrating network, the morphology of BHJ film need to be well controlled. Significant efforts have been focused on this area and vigorous progress has been made, by controlling thermal annealing, solvent annealing, the rate of solvent evaporation and adding additives.[9]–[16] Combining with newly developed polymer of better optical absorption and improved charge mobility, the state-of-art PSCs have achieve power conversion efficiency (PCE) over 9%. [9][17]–[19]

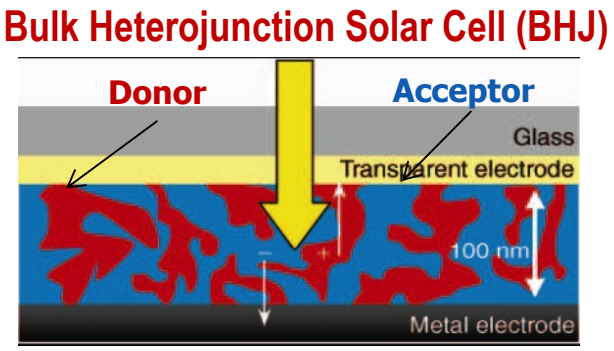

Figure 1-3 Device structure of a bulk-heterojunction polymer solar cell[12]

1.4 DEVELOPMENT OF INVERTED STRUCTURE SOLAR CELLS.

In most of the cases, PSCs based on the conventional device structure are fabricated by sandwiching an active layer between a low work-function metal cathode (e.g., Ca/Al) and a transparent indium tin oxide (ITO) anode with a conducting polymer, poly(3,4-ethylenedioxylenethiophene):poly(styrenesulfonic acid) (PEDOT:PSS) usually used as an anode buffer layer. Recently, the newly developed low band-gap polymers[6-12] and fullerene derivatives[13] have enabled the fabrication of very high power conversion efficiencies (PCEs) of > 7% in the conventional structure PSCs.

However, long-term stability of these devices in ambient is a major concern. The commonly used low work function cathode such as calcium and aluminum is easily oxidized in ambient, in addition, ITO could be etched easily by very acidic PEDOT:PSS to cause device degradation.[14] One way to circumvent these problems is to use an inverted structure PSC. By reversing the polarity of charge collection in the conventional structure, the inverted structure allows more air stable, higher work function metals (e.g., Ag, Cu)[15] to be used in combination with an appropriate interfacial layer (e.g., PEDOT: PSS, MoO_3, V_2O_5, graphene oxide (GO)) to collect holes,[16-20] while a transparent electrode in combination with a metal oxide (e.g., TiO_x, ZnO, Cs_2CO_3) could be used to collect electrons. [19],[21-24] In addition, high work function metals like Ag and Au can be potentially deposited through non-vacuum coating techniques which are important for developing low cost, large area, roll-to-roll printable solar cells. The structure of conventional and inverted device is shown in Figure 1-4.

My research is focus on the development of low cost, high efficiency of inverted structure PSCs, including electrode engineering of investigation alternative transparent electrode to replace ITO, studying inverted geometry's effect on device performance based on optical

modeling, interface engineering of hole transporting layer modification in inverted structure based a newly-developed high performance polymer, and processing engineering of bilayer processed device in inverted structure based on a low-band gap polymer.

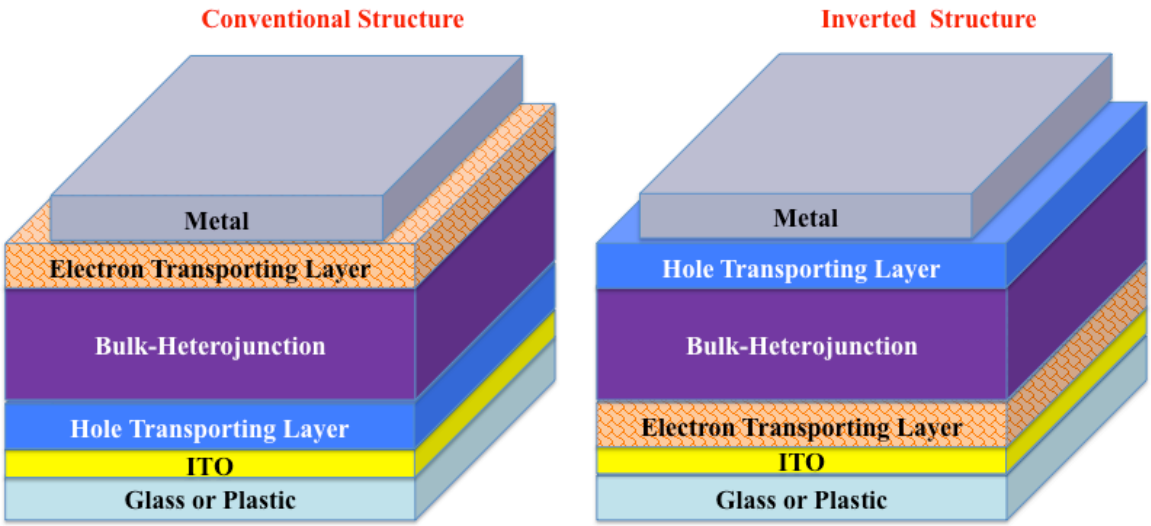

Figure 1-4 Devices structure of conventional and inverted structure.

Chapter 2. INTERGRATED DEVICE ENGINEERING OF POLYMER SOLAR CELLS

2.1 INTRODUCTION

The most common polymer solar cells have been based on the device architecture which consists of a photoactive layer sandwiched between a transparent conducting oxide electrode and a top metal electrode.

The photoactive layer of polymer solar cells are typically processed by spin coating solution that consists a blend of an electron-rich conjugated polymer donor and an electron-deficient fullerene acceptor to form a bulk-heterojunction layer (BHJ). As we described previously, the morphology of BHJ film is critical for device performance, which need to provide greater interface areas to facilitate the excitons dissociation, as well as form bi-continuously path for charge transportation. Much effort has been made in the field to understand how to develop simple reproducible processing conditions to achieve ideal nanoscale morphology to improve polymer solar cells.

In addition to developing processing techniques, there has been much effort on architecture design. One approach that has been taken to improve device performance is to develop alternative device architectures in which the incoming incident optical field distribution is manipulated to increase the chance for maximum light absorbance in the active layer. Also, to have a better charge collection and long term stability of devices, interface engineering has been applied between the BHJ film and electrodes in devices. Elimination of the use of indium tin oxide as the transparent conducting oxide in polymer solar cells is another major challenges, due to the limitation of indium tin oxide of flexibility and conductivity, also the increased cost. This section will review the current approaches on developing different polymer solar cell devices.

2.2 Effects of bulk-heterojunction processing conditions on performance of polymer soe lar cells

From spin coating, the morphology of BHJ films is determined by thermodynamic as well as kinetic effects. From the thermodynamic point of view, the intrinsic properties of the components of the solution (the donor and acceptor materials and the solvent) used to deposit the blended film, such as the Flory-Huggins parameter between the constituents involved, the ratio between the constituents, and the interaction or solubility of the donor and acceptor materials in the solvent, play key roles during the evolution of the film morphology. The thermodynamic parameters reflect the nature of fundamental properties of the solution composed the constituents and solvent applied for thin film deposition. During the film formation, kinetic factors, such as the solvent evaporation rate and post-treatment and crystallization behavior, have significant effects on the morphology of the active layer.[10][13] Both thermodynamic and kinetic parameters show comparable significance in determining the morphology of BHJ films obtained and thus the performance of PSCs eventually. Several approaches have been reported to effectively control this morphology and improve polymer solar cells, which will be discussed as below.

2.2.1 *Effects of composition ratio on polymer solar cells*

The overall concentration of components and the ratio between polymer and fullerene in the solution will affect both light absorption of BHJ films as well as the morphology. Generally, higher compound concentrations induce large-scale phase segregation upon film formation.[14] Depending on the absorption range of polymers, the solubility and crystallinity nature of the polymer:fullerene system, the optimum ratio is found to be different. A comprehensive study of MDMO-PPV/ $PC_{61}BM$ has been done over a wide range of ratio. For $PC_{61}BM$ contents less than 50%, homogeneous films morphology was observed. For concentrations around 67% or higher,

an abrupt improvement of device performance was observed, with the onset of phase separation shown. With the $PC_{61}BM$ concentration increased, both the hole and electron mobilities were improved until 80%. With higher $PC_{61}BM$ ratio, nano-clusters formed by $PC_{61}BM$ are also considered to contribute to the performance improvement.[15][16] The critical concentration of $PC_{61}BM$ is related to the intercalation of fullerene into polymer chains, and the percolation network formation of fullerene. Fullerene intercalation between polymer side chains can inhibit the coiling of the polymer chains and therefore increase the conjugation length, intermolecular interactions, and thus improve the hole mobility.[17][18] When a more crystalline polymer such as P3HT is employed as the donor, the necessary acceptor ratio is found to be significantly reduced. The optimized polymer:fullerene ratio of P3HT: $PC_{61}BM$ systems is reported in the range of 1:1 to 1:0.6. [19][20] Understanding the effect the polymer/fullerene ratio on morphology and device performance is important for the device optimization.

2.2.2 *Effects of solvent on polymer solar cells*

The choice of solvent used to dissolve and deposit the polymer and fullerene from have been shown to have a dramatic effect on device performance. The solubility of the materials in the solvent and the solvent evaporation rate will change the crystallinity as well as phase separation of polymer and fullerene, and affect the charge separation and transport properties.

By changing solvent from toluene to chlorobenzene, PSCs based on MDMO-PPV and $PC_{61}BM$ showed power conversion efficiency improvement from 0.9% to 2.5%, with the same preparation conditions.[21] Investigated by TEM images, MDMO-PPV/ $PC_{61}BM$ system gave a morphology in which PCBM-rich domains are dispersed in the MDMO-PPV-rich matrix, and the size of PCBM-rich domains in the blend films change tremendously with the choice of solvent. Processed from tollenrene, the average size of the PCBM-rich domains is around 600nm with a

broad size distribution (about 350-1300 nm). As a comparison, by using chlorobenze, $PC_{61}BM$ clusters with average size of 80nm were observed.[22][23] The maximum solubility of $PC_{61}BM$ in toluene is reported as 1 wt% while in chlorobenze is 4.2 wt%. The lower solubility of $PC_{61}BM$ has been claimed to be the reason of coarser phases due to the aggregation in solvents, and leads to reduced interfaces for charge separation.

A higher boiling point solvent utilized for BHJ deposition will result in a slower drying of films during spin coating. In P3HT: $PC_{61}BM$ system, it has been found the 1,2-orthodichlorobenze (*o*-DCB) will lead to a better ordering of P3HT polymer chains, and contribute to higher hole mobility as well as improved device performance. [20][24]

2.2.3 *Effects of thermal treatment on polymer solar cells*

Thermal treatment is a commonly used post-treatment method to influence the morphology of active layers in PSCs. During thermal annealing, reorganization of the film morphology is forced, especially when components of the BHJ have the ability to pack. The result device performance depends on the annealing temperature, annealing time, and could affect device performance in both positive and negative ways. For the system of MDMO-PPV/ $PC_{61}BM$, annealing always results in unflavored large-scale phase separation and large $PC_{61}BM$ single crystals, even for short times or low temperatures below the glass transition temperature of MDMO-PPV (~80°C), and leads to a significant decreasing of device performance.[22][25] In contrast, appropriate annealing of P3HT/ $PC_{61}BM$ system results in a significant improvement of its power conversion efficiency. In all studies, a remarkable increase of the performance is observed after annealing, and power conversion efficiencies as high as 5.2% have been reported.[26] During annealing, the crystalline order of both P3HT and PCBM has been improved,

and the interpenetration of the two components has been enhanced.[27] Both are considered contribute to the improved device performance.

2.2.4 *Effects of solvent vapor annealing on polymer solar cells*

Solvent vapor annealing allows a saturated solvent vapor environment around the bulk-heterojunction films after spin coating, which could partially re-dissolve and rearrange materials to produce better ordering or penetration. For widely studied P3HT/ $PC_{61}BM$ system, it has been observed that after spin coating from a chlorobenzene solution, 30 minutes of solvent vapor treatment in *o*-dichlorobenzene leads to improve the PCE from 0.80% to 1.35%. By further annealed at 150°C for 1 minutes, PCE has reached 3.7%. UV-Vis study and mobility testing indicate that solvent vapor annealing provided more intense P3HT ordering than thermal annealing, and improved hole mobility. However, a short thermal treatment is still necessary to improve the $PC_{61}BM$ ordering and balance the charge transport.[28] Other studies have suggested that the performance of device obtained by solvent vapor annealing can exceed that of thermally annealed devices. By sealed devices in a petri dish after spin coating from dichlorobenzene overnight without thermal annealing, 3.7% PCE has been achieved, comparing with 3.1% result from thermal annealing. [29] Although more consideration in the reproducibility of this type of processing is needed, using the solvent vapor annealing is more suitable for flexible plastic substrates since it requires a lower temperature processing.

2.2.5 *Effects of additives on polymer solar cells*

Adding high boiling point solvent to a typical solvent allows further control over the final device morphology and performance. Several high boiling point solvents have been used to for the enhancement of PSC devices performance, such as octanedithiol, [30] diiodooctane[31], chloronaphthalene[32]. It is believed that in certain polymer/fullerene system, during spin-coating

process, the dissimilar solvent mixture can facilitate fullerene cluster formation and subsequently lead to the "intelligent" phase separation of the active layer into an optimum morphology.[33] By incorporating a few volume percent of alkanedithiol into the chlorobenzene from which BHJ films comprising the low bandgap polymer [2,6-(4,4-bis(2-ethylhexyl)-4*H*-cyclopenta[2,1-b;3,4-b']-dithiophene)-*alt*-4,7-(2,1,3-benzothiadiazole)] (PCPDTBT) and C_{71}-PCBM are cast, the power conversion efficiency was increased from 2.8% to 5.5%.[31] It is concluded that alkanedithiol have selective solubility for fullerene, and result in larger domains with wider connective cross section of fullerene, which contribute to the improve hole mobility. [19] poly [(4,4-didodecyldithieno [3,2-b:2',3'-d] silole) - 2,6-diyl-alt- (2,1,3-benzoxadiazole) - 4,7-diyl] (P1) displays a strong tendency toward aggregation in solution. When combined with $PC_{71}BM$, the films obtained from chlorobenzene exhibit large surface roughness with a complex surface morphology. The addition of CN leads to smoother films, planarize the surface of the active layer and to reduce the heterogeneity of the donor and acceptor phases. [20]

2.3 OPTICAL MANAGEMENT IN POLYMER SOLAR CELLS

Photovoltaic device performance is affected by the rate of photo absorption in the active layer, exciton generation, charge separation, transport and collection. In order to get optimized photo current, the light harvesting in active layer need to be maximized. The incident light forms a standing wave inside the devices, and the optical field intensity diminishes to zero after propagation into reflecting electrode. The maximum intensity is located at a certain distance away from the reflective mirror, depending on the refractive indices and thickness of each layer in devices.

The fraction of incident light intensity absorbed by the active layer is influenced by all layers in the device due to the interference effect, therefore, independently measured the absorption of bulk-heterojuction (BHJ) films cannot be counted on to represent the absorption of films in devices. To determine the individual contribution of the active layer on optical absorption, proper optical modeling is needed. Transfer matrix formalism is commonly used to calculate the interference of reflected and transmitted light waves at each interface in the stack based on the wavelength-dependent complex index of refraction (n+ik) of each materials.[34][35]

With reversed device architecture and different interface materials, different electric field distribution will be generated in inverted structure, comparing with conventional structure. The change of electric field distribution will result in the change the light absorption in active layer, and also spatial distribution of exciton generation. By simultaneously optimized the thickness of active layer and interface, S. Albrecht, et.al, have demonstrated with inverted device stacks, the light absorption can be enhanced and generate 10% larger short circuit current than conventional devices.[36] Thus, for defined polymer system, with a careful design of device architecture and well control of morphology, inverted structure devices have the potential to give better performance, in addition to its intrinsic better stability.

Besides absorption, spatial distribution of exciton generation is another import issue for optical management in device architecture optimization. The interface layers between the active layer and electrode can manipulate electric filed spatial distribution, and the hole transporting layer in front of the metallic electrode shows more obviously optical spacer effect in redistribution of the exciton generation.[37][38][39] In order to get the largest current generation, the optical effect of interface thickness needs to be considered as well as the materials' intrinsic conductivity.

The optimized spatial distribution of exciton generation is related to the hole and electron mobility balance in active layer. In several newly developed polymer system, exciton generation peak shifting to anode can be observed. Therefore, most of the generated electrons need to travel longer distance in order to be collected by the cathode. This increases the probability of charge recombination during their transport. Thus, higher electron mobility is needed in order to maximize the generated current. Higher fullerene ratio in the BHJ film is an efficient way to maintain adequate electron mobility in inverted structure, and this also can explain the different optimized processing condition in conventional and inverted structure.

2.4 INTERFACE ENGINEERING OF POLYMER SOLAR CELLS

The contact at the interfaces between layers is one of the most critical parameters to determine the performance of polymer solar cells. It is necessary to establish ohmic contacts with minimum resistance and high charge selectivity at both electrodes for efficient charge extraction. Tremendous efforts have been devoted to engineer the interfaces by introducing proper interfacial materials.[8][40] Particularly, in solution-processed polymer active layers, the surface properties of the bottom interface have a substantial influence on the film morphology, which will also affect device performance.[41][42]

The interface layers inserted between electrodes and organic photo-active layers dramatically alter the interface properties and can determine the overall device performance. The main functions of the interfacial layers include: Minimization of the energy barrier for charge injection and extraction; determination of the relative polarity of the devices and improving charges selectivity; modification of the surface property to alter film morphology; suppression of diffusion and reaction between the electrode material and polymer; modulation of the optical filed by introducing optical spacer and plasmonic effects.[40]

Particularly, self-assembled monolayers(SAMs) can be employed to modify the surface of metal oxide interfacial layers. By using SAMs the can form favorable dipoles and covalent bonding between electrode and metal oxide, the contact between metal oxide buffer layer and metal electrode and be facilely engineered. Significant improvement in efficiency has been shown, and higher work function metals such as Ag or Au can be allowed to be used as cathode.[43][44] The modification of electron transporting layers of metal oxide films in inverted structure with functional SAMs can also efficiently alter the morphology of BHJ. By changing the surface compositions the two different SAMs with either polar $–NH_2$ or non-polar $–CH_3$ end group, a wide range of surface energies from 40mN/m to 70mN/m has been demonstrated, and the optimized surface energy leading to an improved PCE of devices. [45] Modifying the metal oxide underneath BHJ film with fullerene-based SAMs has been proved to be an efficient way to improve device performance of inverted structure PSCs. fullerene-based SAMs could enhance the interfacial exicton-dissociation efficiency, passivate inorganic surface trap states, and optimize the upper organic layer morphology.[46]

2.5 ELECTRODE ENGINEERING OF POLYMER SOLAR CELLS

Currently, Indium Tin Oxide (ITO) is the most commonly used commercial available transparent electrode, as it combines both high optical transparency in the visible range (~82%) and low resistivity (~10-20Ω/□ on glass). However, ITO is becoming one of the limiting factors for device performance as well as flexibility for the new generation optoelectronic devices, due to its limited conductivity on flexible substrates (~60Ω/□) and poor mechanical ductility. Plus, the price of ITO is increasing in recent years as a result of limited availability of indium.[47][48]

Alternative materials for transparent electrode is necessary and has been widely studied, including other transparent conducting oxide,[49][50] carbon nanotubes,[51] graphene,[52]

conducting polymers,[53][54] metal nanowires or meshes,[55] patterned metal grids,[56]–[59] and ultra thin metal films (UTMF).[60]–[63] Among them, metal grids and UTMF combine the characteristics of high electrical conductivity as well as good mechanical ductility, and will be discussed in details later.

Chapter 3. PROCESSING OPTIMIZATION OF NEWLY DEVELOPED MATERIALS FOR POLYMER SOLAR CELLS

3.1 INTRODUCTION

Research on polymer solar cells has been based on polymer materials that have a delocalized π-conjugated electron system that can absorb light, create photo generated charge carriers and transport the charge carriers to generate photocurrent. The properties of polymers could be tuned by controlled molecular design. The light harvesting as well as charge transport properties are both important considerations when developing new polymer systems for solar cells. Much of the development in this area has been tried to manipulate the absorbance, improve inter-chain packing and interaction to have good charge transport mobility, so that the maximum potential current can be generated and extracted.

With the rapid development of new polymers for light harvesting, it is critical to optimize the processing of these polymers in bulk-heterojunction films regarding to the previous discussion. By simultaneously tune film thickness, solvent choice, polymer/fullerene ratio together with post treatment, the optimized device performance could be achieved. It is also important to understand the polymer structure and properties relationship, and correlate the polymer structure with devices performance by characterizations including optical, electrical and morphological methods. Several polymers systems have been developed in our group to obtain high power conversion efficiency, and the photovoltaic device performance have been demonstrated, together with comprehensive characterizations to understand the effects of polymers structure changing.

3.2 Conjugated Polymers Based on C, Si and N-Bridged Dithiophene and Thienopyrroledione Units[64]

3.2.1 *Introduction*

Compared to conjugated homopolymers (such as P3HT), donor-acceptor (D-A) conjugated polymers, with electron-rich and electron-deficient units alternating on the polymer backbone, are proven to be an effective approach to make low band-gap polymers. The band-gap and energy level of these conjugated polymers can be easily tuned by using suitable donor and acceptor units, such as fluorene, silafluorene, carbazole, benzodithiophene, benzothiadiazole, qunioxaline, and thienopyrazine, etc., to achieve PCE of higher than 5%.[65]–[68]

Among these conjugating moieties, dithiophene unit bridged with a carbon (C) or a silicon (Si) atom has been incorporated into alternating copolymers with an electron-deficient benzothiadiazole unit to make efficient polymer BHJ cells. Originally, a low PCE of ca. 2.7% has been achieved for devices containing the C-bridged dithiophene-based polymer donor (PCPDTBT) and the $PC_{61}BM$ acceptor. By optimizing the morphology of PCPDTBT/$PC_{71}BM$ blend with a small amount of alkylenedithiol additive, the PCE went up to 5.5%.[69][70] However, other conjugated polymers with the same donor unit can only get low PCE of 1-2%.[71][72] This shows that morphology of these types of polymers is quite sensitive to the solvents or additives used for device processing. In addition to PCPDTBT, its Si-analog, PSBTBT, has also been reported by Hou *et al.*[73] and Brabec *et al.,*[74] as a promising polymer donor for PSCs. By changing the bridging atom from C to Si, the PCE of the devices can improve to 5.1% without adding any additives during the device fabrication.[73] This is possible due to longer C-Si bond (~0.3Å) on PSBTBT allows for better inter-chain polymer packing to improve hole mobility.

Compared to the C- and Si-bridged dithiophene, dithieno[3,2-b:2',3'-d]pyrrole (DTP), the N-bridged dithiophene, possesses stronger electron-donating ability and has been used as an electron-rich donor for D-A conjugated polymers. For example, DTP-based polymers such as PDTPDTBT and PDTPDTDPP containing either a bis(2-thienyl)-2,1,3-benzothiadiazole-5',5''-diyl or a 3,6- dithiophen-2-yl-2,5-dihydropyrrolo[3,4-c]pyrrole-1,4-dione (DPP) as electron-deficient unit have been reported by Zhou *et al.* that show broad absorption almost reach 1100 nm. However, bulk-heterojunction (BHJ) cells derived from these polymers only show relatively low PCE of 2.18 % and 2.71%.[75][76] This is due to low V_{oc} (0.37-0.62 V) of these devices (as a result of high HOMO energy level of these polymers) that limits their performance. Therefore, it is critical to develop polymers with optimal HOMO energy levels and charge-transporting properties to improve device performance.

In this paper, we present a series of new D-A alternating polymers based on C-, Si- and N-bridged dithiophene as the electron-rich donor and thienopyrrodione (TPD) as the electron-deficient acceptor (Figure 3-1). Recently, we and others have reported devices based on polymer containing thienopyrroldione (TPD) and benzodithiophene units that show high V_{oc} (as high as 0.89 V).[77][77]–[80] This inspires us to further explore the possibility of using TPD to copolymerize with electron-rich bridged dithiophenes to improve polymer properties.

3.2.2 *Experimental*

The synthesis of these Conjugated Polymers Based on C, Si and N-Bridged Dithiophene and Thienopyrroledione Units are fully described elsewhere.[64]

To fabricate conventional configuration solar cells, ITO-coated glass substrates (15 Ω/sq.) were first cleaned with detergent, de-ionized water, acetone, and isopropyl alcohol. A thin layer (ca. 40 nm) of PEDOT:PSS (Baytron® P VP AI 4083, filtered at 0.45 μm) was first spin-coated

on the pre-cleaned ITO-coated glass substrates at 5,000 rpm and baked at 140°C for 10 min under ambient conditions. The substrates were then transferred into an argon-filled glove-box. Subsequently, the polymer:$PC_{71}BM$ active layer (ca. 90 nm) was spin-coated onto the PEDOT:PSS layer at 900 rpm from a homogeneous blend solution. The solution was prepared by dissolving the polymer at a blend weight ratio of 1:2 in o-dichlorobenzene (or o-dichlorobenzene with 2 vol% of 1-chloro-naphthalene) and filtered with a 0.2 μm PTFE filter. At the final stage, the substrates were pumped under high vacuum ($< 2 \times 10^{-6}$ Torr), and calcium (0.8 nm) topped with aluminum (100 nm) was thermally evaporated onto the active layer through a shadow mask to define the active area of the devices. The device pattern was a 2 mm diameter circle, which had nominal device area of 3.14×10^{-2} cm^2.

The un-encapsulated solar cells were tested under ambient conditions using a Keithley 2400 SMU and an Oriel Xenon lamp (450 W) with an AM1.5 filter. The light intensity was calibrated to 100 mW/cm^2 using a calibrated silicon solar cell with a KG5 filter, which has been previously standardized as the National Renewable Energy Laboratory.

The current-voltage (I-V) characteristics of unencapsulated photovoltaic devices were measured under ambient conditions using a Keithley 2400 source-measurement unit. An Oriel xenon lamp (450 Watt) with an AM1.5 G filter was used as the solar simulator. The light intensity was set to 1 sun (100 mW cm^{-2}) using a calibrated Hamamatsu silicon diode with a KG5 color filter, which can be traced to the National Renewable Energy Laboratory (NREL). The EQE system uses a lock-in amplifier (Stanford Research Systems SR830) to record the short-circuit current under chopped monochromatic light.

3.2.3 *Results and Discussion*

The optical properties of these polymers were investigated in chloroform solutions and in thin films. Figure 3-2a shows the absorption spectra of all three polymers in chloroform solution. From the spectra it can be observed that, as the identity of the bridging atom is varied, the absorption maximum changes from 653 nm in PDTC with a high-energy shoulder at 604 nm, to 608 nm in PDTSi with a low-energy shoulder at 660 nm, and to 645 nm in PDTP with a high-energy shoulder at 598 nm. The absorption edge of PDTC and PDTSi are similar at ~723 nm, while PDTP has a lower-energy absorption edge of 747 nm. In thin film state (Figure 3-2b), the predominant peaks move to 671, 665 and 686 nm in PDTC, PDTSi and PDTP, respectively. The red-shift in film state compared to solution state likely implies a slightly increased extent of pi-pi stacking along the polymer backbone. On the other hand, the slight red-shift in λ_{max} of PDTP compared to PDTC and PDTSi is consistent with the stronger donor properties of N atom relative to C or Si.[76] The absorption edges in film state for PDTC, PDTSi and PDTP are 741, 734 and 778 nm, respectively. The corresponding optical band-gaps of these polymers calculated from the absorption edge in film state were estimated to be 1.67, 1.70 and 1.59 eV for PDTC, PDTSi and PDTP, respectively.

In general, the formation of a bi-continuous interpenetrating network between polymer donor and PCBM acceptor is the most promising architecture in BHJ cells. The morphology of an active layer (polymer: PCBM blend film) is very critical for the performance of BHJ cells. If there are large size domains and significant phase separation in active layer, it will reduce the interfaces for efficient charge separation and a smooth film with few domains will also increase the possibility for charge recombination. As it can be seen from Table 3-1, PDTSi and PDTP devices fabricated from o-DCB solution show much poorer performance compared to PDTC

device. The inferior device performance may be due to the non-optimal morphology in these polymer/$PC_{71}BM$ blend films.

To understand the morphological effect on the device performance, the films of polymer blends were investigated by tapping-mode atomic force microscopy (AFM) and these AFM topography images were shown in Figure 3-3 AFM topography images of polymer: $PC_{71}BM$ (1:2 wt) blend films from o-DCB (a, b, c) and o-DCB : 2 vol% 1-chloronaphthalene (d, e, f).. As shown from Figure 3-3 a, the PDTC/$PC_{71}BM$ film shows a smoother surface and smaller phase separation, which facilitates charge separation and results in higher device performance. However, in the PDTSi/$PC_{71}BM$ and PDTP/$PC_{71}BM$ blend films (Figure 3-3 b, c), significant phase separation and large domains were observed. This leads to poorer charge separation and increased charge carrier recombination. The strong phase separation may be due to polymer self-aggregation and/or incompatibility between polymer and $PC_{71}BM$. Therefore, this results in poorer performance in PDTSi and PTDP devices.

There are several ways to alter the interpenetrating nanoscale morphology of a BHJ cell. Bazan *et al*. have demonstrated that the addition of a small amount of solvent additives with high boiling point into conjugated polymer/PCBM solution during processing can give substantial increase of device performance due to significantly improved morphology. The solvent additives play a role of slowing down the aggregation of conjugated polymer and PCBM so as to be able to avoid forming the over-shape polymer or PCBM aggregates, which inhibit charge carrier transport in BHJ film.[81][82] Recently, 1-chloronaphthalene (CN) has been proved to be an alternative solvent additive in improving the performance of the bridged dithiophene-based polymers.[32][83] To take advantage of this effect, CN was also used as the solvent additive to improve the morphology of the polymer blends, especially for the PDTSi/$PC_{71}BM$ and

PDTC/$PC_{71}BM$ systems. The morphology of the polymer/$PC_{71}BM$ films cast from their o-DCB solution with 2 vol% of CN was studied by AFM. Figure 3-3 showed the AFM topographical images. As shown from Figure 3-3 d, the addition of 2 vol% CN had minor effect on the morphology of PDTC/$PC_{71}BM$ thin film. However, the previously observed large size domains from the PDTSi/$PC_{71}BM$ and PDTP/$PC_{71}BM$ thin films cast from their o-DCB solution (Figure 3-3 b, c) can no longer be detected. The nanoscale morphologies of PDTSi/$PC_{71}BM$ and PDTP/$PC_{71}BM$ films were substantially improved. This indicates that CN solvent additive can promote the self-aggregation of PDTSi and PDTP in a relatively fluid medium and also improves the compatibility between polymer and $PC_{71}BM$.[32][82] As a result, the relatively smooth BHJ films of polymer/$PC_{71}BM$ were formed. To verify this point, BHJ cells with the same device configuration described above were fabricated by spin-coating films from their o-DCB:2 vol% CN solutions. The optimized volume of CN is 2 vol%. The J-V curves of these devices were shown in Figure 3-4 b and summarized inTable 3-1. As shown in Figure 3-4 b, there are significant improvements in the device performance, especially for the PDTSi and PDTP devices. The PCE of the PDTC device remained to be 3.45% while the PCE of PDTSi device increased from 1.18% to 2.13% with almost 3 times increase of its J_{sc}. However, V_{oc} of the device showed a slight decrease to 0.85 V. The similar decrease has also been observed earlier[69] which may be due to morphological changes and interfacial interactions between the active layer and cathode. For the PDTP device, the PCE improved from 0.91% to 1.69% after the addition of CN. The external quantum efficiency (EQE) of these devices was measured to evaluate the photoresponse of the BHJ cells. Figure 3-5 showed the EQE curves of the PDTC device fabricated from o-DCB and the PDTSi and PTDP devices fabricated from o-DCB:2 vol% CN solution. All devices exhibited efficient photoresponse between 350 and 750 nm. The EQE of the

PDTC device is more than 45% with the highest value reached 53.5% at 570 nm. However, the PDTSi and PDTP devices showed much lower EQE values compared to PDTC device with their maximum reached 38.3% and 25.2% at 560 nm, respectively. The low EQE values affect the low J_{sc} observed for PDTSi and PDTP devices (Table 2). In addition, the low EQE in PDTSi and PDTP devices was mainly ascribed to the lower hole mobility observed in these two polymers because non-ideal interpenetrating nanoscale phase separation between the polymers and $PC_{71}BM$. Since there are many factors affecting the phase separation, such as the Flory–Huggins interaction, the tendency of the components to aggregate, and the kinetic constraints,[10][69][84] further work will focus on understanding the relationship between morphology and performance and will be reported elsewhere.

3.2.4 *Conclusions*

Three new polymers, PDTC, PDTSi and PDTP have been designed and synthesized between C-, Si-, N-bridged dithiophene stannyl compound and 1,3-dibromo-5-octylthieno[3,4-c]pyrrole-4,6-dione.The photovoltaic properties of these polymers were investigated using the device configuration of ITO/PEDOT:PSS/polymer:$PC_{71}BM$ (1:2)/Ca/Al. The highest achievable PCE for PTDC, PDTSi, and PDTP is 3.74%, 2.13%, and 1.69%, respectively. It worthy to note that the V_{oc} of these devices increased significantly (~0.2-0.4 V) due to lower HOMO energy level of these polymers compared to other C-, Si-, N-bridged dithiophene-based polymers.

Table 3-1 Performance of PDTC, PDTSi and PDTP Photovoltaic Devices under the AM 1.5 Simulated Illumination (100 mW/cm^2).

polymer:	V_{oc}	J_{sc}	FF	PCE
$PC_{71}BM$ (1:2)	(V)	(mA/cm^2)		(%)
PDTC[a]	0.80	10.04	0.47	3.74
PDTC[b]	0.80	9.40	0.45	3.45
PDTSi[a]	0.91	2.32	0.56	1.18
PDTSi[b]	0.85	6.58	0.37	2.13
PDTP[a]	0.71	2.53	0.50	0.91
PDTP[b]	0.76	4.69	0.53	1.69

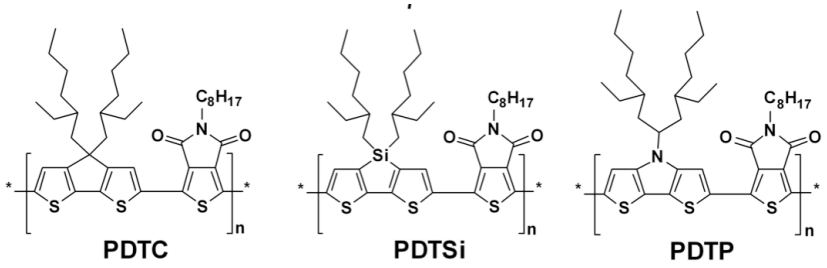

Figure 3-1 Chemical structure of PDTC, PDTSi and PDTP

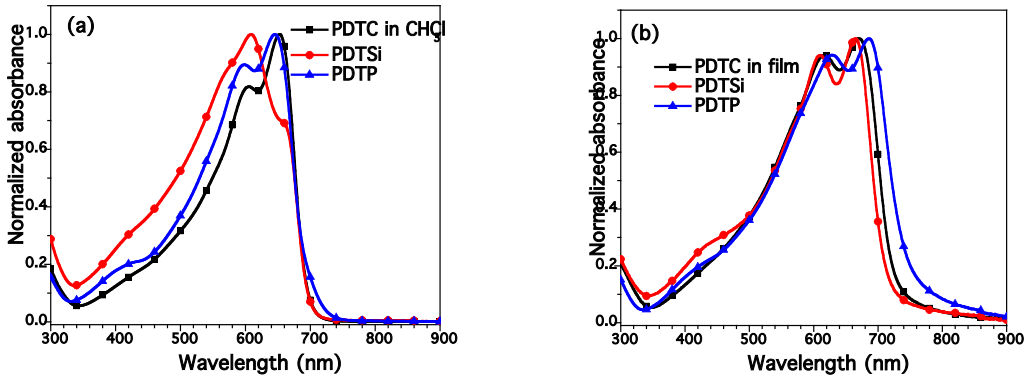

Figure 3-2 UV-Vis spectra of polymers PDTC, PDTSi and PDTP in (a) chloroform solution and in (b) film states.

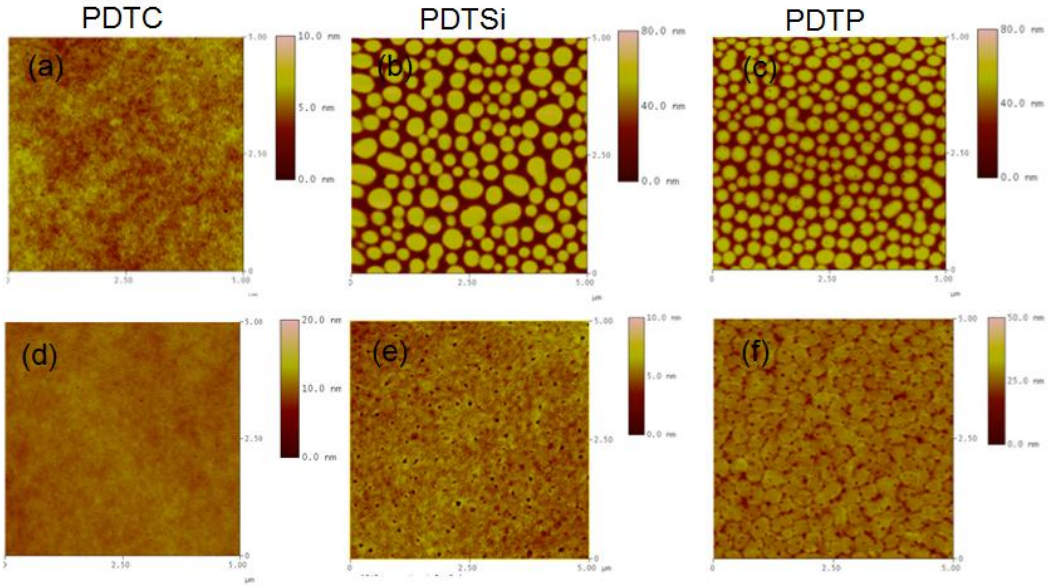

Figure 3-3 AFM topography images of polymer: $PC_{71}BM$ (1:2 wt) blend films from o-DCB (a, b, c) and o-DCB : 2 vol% 1-chloronaphthalene (d, e, f).

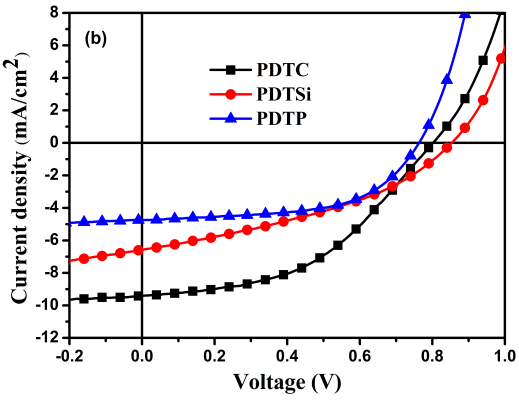

Figure 3-4 J-V curves of PDTC, PDTSi and PDTP devices (a) film prepared from pristine o-DCB solution and (b) film prepared from o-DCB: 2 vol%1-chloronaphthalene under illumination of AM 1.5, 100 mW/cm^2.

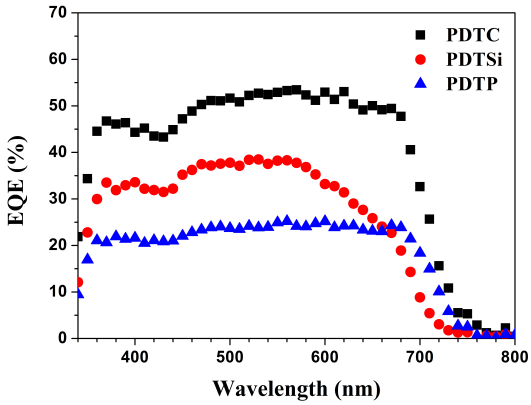

Figure 3-5 External quantum efficiency spectrum of optimized PDTC, PDTSi and PDTC devices.

3.3 Indacenodithiophene and Quinoxaline-Based Conjugated Polymers[85]

3.3.1 *Introduction*

Recently, conjugated polymers based on the indacenodithiophene (IDT) unit have exhibited more research interest with promising performance in PSCs,[86]–[89] because the IDT unit can enhance the co-planarity of polymer backbone with the reduced energetic disorder of the polymer. For example, Ting and co-workers have reported a PCE of 6.1% from the alternating polymer of IDT and benzothiadiazole (BT) units.[88] More importantly, the IDT-based polymers show high and stable field-effect hole mobilities. A hole mobility of as high as ~1 cm^2 V^{-1} s^{-1} from the analogous polymer of IDT and BT units has been reported by Zhang et al.[86]

Quinoxaline has been widely implemented as an electron-deficient co-monomer of low-band gap polymers in PSCs. The impressive performance of quinoxaline-based polymers has shown its obvious potential for achieving high performance in PSCs. [90]–[95] 2,3-Diphenylquinoxaline, which possesses two separated phenyl rings, is one of the commonly investigated quinoxaline derivatives due to its facile synthesis and versatility. Research efforts focusing on tuning the solubility, band-gap, and energy levels of 2,3-diphenylquinoxaline-based polymers have resulted in PCEs of ≤ 6%.[90]–[95] However, most of these polymers possess large band-gaps (> 1.9 eV) and low charge carrier mobilities (~10^{-5} cm^2 V^{-1} s^{-1}). Moreover, two separated phenyl rings on the 2,3-diphenylquinoxaline could induce some steric hindrance to interrupt intermolecular stacking between polymer chains.

If two phenyl rings could be connected by a single bond between the *ortho* positions, it will significantly increase the planarity of quinoxaline and facilitate both intermolecular packing and charge transport. Moreover, the extended π-conjugation of the fused qunioxaline (named as

phenanthrenequnioxaline) will function as a stronger electron-acceptor, leading to lower bandgap in the corresponding polymer. In this communication, we combined IDT and two quinoxaline derivatives to form new polymers (PIDT-diphQ and PIDT-phanQ, Figure 3-6). Due to the enhanced planarity of phenanthrenequnioxaline, PIDT-phanQ/$PC_{71}BM$-based BHJ device exhibits an improved PCE of 6.24% compared to the PCE of 5.69% in PIDT-diphQ/$PC_{71}BM$-based device.

3.3.2 *Experimental*

The synthesis of these Conjugated Polymers are fully described elsewhere.[85]

Polymer solar cells were fabricated using the same device structure for both polymers (ITO/PEDOT:PSS/PIDT-diphQ or PIDT-phanQ:$PC_{71}BM$ (1:3, w/w)/Ca/Al). To fabricate the conventional solar cells, ITO-coated glass substrates (15 Ω/sq.) were cleaned with detergent, de-ionized water, acetone, and isopropyl alcohol. A thin layer (ca. 40 nm) of PEDOT:PSS (Baytron® P VP AI 4083, filtered at 0.45 μm) was first spin-coated on the pre-cleaned ITO-coated glass substrates at 5,000 rpm and baked at 140°C for 10 minutes under ambient conditions. The substrates were then transferred into an argon-filled glove-box. Subsequently, the polymer : $PC_{71}BM$ active layer (ca. 90 nm) was spin-coated on the PEDOT:PSS layer at 900 rpm from a homogeneously blended solution. The solution was prepared by dissolving the polymer at different blend weight ratio from 1:3 in o-dichlorobenzene and filtered with a 0.2 μm PTFE filter. The substrates were annealed at 110 °C for 10 minutes prior to electrode deposition. At the final stage, the substrates were pumped down to high vacuum ($< 2 \times 10^{-6}$ Torr), and calcium (30 nm) topped with aluminum (100 nm) was thermally evaporated onto the active layer through shadow masks to define the active area (10.08×10^{-2} cm^2) of the devices.

The un-encapsulated solar cells were tested under ambient conditions using a Keithley 2400 SMU and an Oriel Xenon lamp (450 W) with an AM1.5 filter. The light intensity was calibrated to 100 mW/cm^2 using a calibrated silicon solar cell with a KG5 filter, which has been previously standardized as the National Renewable Energy Laboratory.

The current-voltage (I-V) characteristics of unencapsulated photovoltaic devices were measured under ambient conditions using a Keithley 2400 source-measurement unit. An Oriel xenon lamp (450 Watt) with an AM1.5 G filter was used as the solar simulator. The light intensity was set to 1 sun (100 mW cm^{-2}) using a calibrated Hamamatsu silicon diode with a KG5 color filter, which can be traced to the National Renewable Energy Laboratory (NREL). The EQE system uses a lock-in amplifier (Stanford Research Systems SR830) to record the short-circuit current under chopped monochromatic light.

Space charge limited currents have been tested in hole-only devices with a configuration of ITO/PEDOT:PSS/polymer:$PC_{71}BM$/PEDOT:PSS/Ag. The devices were prepared following the same procedure described above for photovoltaic devices, except that the metal electrode was replaced by PEDOT:PSS(15nm)/Ag(100nm). The mobilities were determined by fitting the dark current to the model of a single carrier space charge limited current with field dependent mobility, which is described as

$$J = \frac{9}{8}\varepsilon_0\varepsilon_r\mu_0 \exp\left(0.891\gamma\sqrt{\frac{V}{L}}\right)\frac{V^2}{L^3}$$

where J is the current, μ_0 is the zero-field mobility, γ is the field activation factor, ε_0 is the permittivity of free space, ε_r is the relative permittivity of the material, L is the thickness of the active layer, and V is the effective voltage. The effective voltage can be obtained by subtracting the voltage drop (V_{RS}) from the substrate's series resistance from the applied voltage (V_{APPL}),

$V=V_{APPL}$ -V_{RS}. The built-in voltage was assumed to be zero since PEDOT:PSS was used in both electrodes. In all the simulations, ε_r was assumed to be 3, which is a typical value for organic materials. L equaled to 135nm and 137nm for device with active materials PIDT-diphQ and PIDT-phanQ, which was measured using atomic force microscopy. The series resistance to our substrates was determined from a reference device without the active layer, i.e. a device configuration of ITO/PEDOT:PSS/Ag, and was found to be ca. 21.9 Ω. μ_0 and γ were extracted at the region where J and V follow the near quadratic space charge limited formula mentioned above.

3.3.3 *Results and Discussion*

The UV-Vis spectra of the polymers in chloroform and in the film state are shown in Figure 3-7a. In chloroform solution, PIDT-diphQ shows an absorption maximum at 617 nm with a weaker peak at 420 nm. The λ_{max} of the solid film of PIDT-diphQ, however, exhibits a blue-shift of 36 nm to 581 nm (Figure 3-7a). A similar phenomenon has been reported and is attributed to the decreased conjugation length in solid film due to steric hindrance between the pendent phenyl rings on the IDT and quinoxaline units. This will weaken the inter-chain packing of polymer in solid state. Interestingly, the absorption of PIDT-phanQ in chloroform gives two peaks at the maximum of 644 nm and 442 nm, respectively, which shows ~30 nm red-shift compared with PIDT-diphQ due to the extended conjugation length of the phenanthrenequinoxaline unit on PIDT-phanQ. However, the absorption of PIDT-phanQ thin film is almost identical with that observed in solution (Figure 3-7a), which showed a 63 nm red-shift compared to PIDT-diphQ. This indicates that the more planar phenanthrenequinoxaline unit not only effectively reduces steric hindrance in the solid state but also promotes stronger chain stacking even in solution. It is well known that thermal treatment can change the conjugated

polymer chains stacking. To further explore the chain stacking of both polymers, the UV-Vis spectra of PIDT-diphQ and PIDT-phanQ films with thermal treatment at 110 ^{o}C for 10 min were measured. As shown in Figure 3-8, the UV-Vis spectrum of PIDT-phanQ film with thermal treatment shows no change compared with that as-spun film. This means that PIDT-phanQ already has tightly stacking in the as-spin film. However, for PIDT-diphQ polymer, it can be found a significant change on both absorption peak and absorption onset. This result shows the as-spun film of PIDT-diphQ is stacking incompactly. Therefore, it clear shows that the PIDT-phanQ polymer has stronger chain stacking than the PIDT-diphQ. The absorption onsets of PIDT-diphQ and PIDT-phanQ in as-spun film are ~684 and ~744 nm, respectively, corresponding to an optical band-gap of 1.81 and 1.67 eV. The ~0.14 eV reduction of polymer band-gap is found due to the enhanced planarity of using phenanthrenequinoxaline as the co-monomer.

In the PIDT-diphQ device, it showed a V_{oc} of 0.87 V, a short-circuit current density (J_{sc}) of 10.9 mA cm^{-2}, and a fill factor (FF) of 0.60, resulting a relatively high PCE of 5.69%. Under the same conditions, the PIDT-phanQ device showed an increased PCE of 6.24% with a V_{oc} of 0.87 V, a J_{sc} of 11.2 mA cm^{-2} and a FF of 0.64. It is very encouraging that the device performance of both polymers, especially for the one based on PIDT-phanQ has already shown comparable result with those the state-of-the-art PSCs. [96][97]

There are several factors that may contribute to the result of getting high PCE in PIDT-phanQ based device. First of all, the PIDT-phanQ polymer has a relatively low band-gap of 1.67 eV and preferred energy levels that are well matched with $PC_{71}BM$.[98] The hole mobilities of polymers/$PC_{71}BM$ blend films measured by using the space-charge-limit-current (SCLC) method also showed high values (1.14×10^{-3} and 2.06×10^{-3} cm^2 V^{-1} s^{-1} for PIDT-diphQ and PIDT-

phanQ, respectively). Furthermore, the morphology of the polymer/$PC_{71}BM$ blend films measured by AFM showed very smooth films, indicating homogeneous mixing of polymers and $PC_{71}BM$ (Figure 3-10). The combined smooth morphology and high mobility of the blends, therefore, resulted in a high FF (64%). The high V_{oc} value (0.87 V) is related to the deeper HOMO levels of the polymers.

The external quantum efficiency (EQE) is commonly used to evaluate the photo response of the devices. As shown in Figure 3-9b, both devices exhibited high photo conversion efficiency covering from 350 nm to 700 nm with an EQE value of more than 50% in the region between 350 and 650 nm and also agree well with the UV-Vis absorption of polymer/$PC_{71}BM$ blend films. The J_{sc} calculated from the EQE curves are 10.3 and 11.1 mA cm^{-2} for PIDT-diphQ and PIDT-phanQ, respectively, showing a mismatched factor less than 2% compared with those values measured under AM 1.5G illumination.

3.3.4 *Conclusions*

In conclusion, two small band-gap conjugated polymers based on the polymerization of IDT and quinoxaline units have been synthesized. Both polymers show good solubility in common organic solvents because of the peripheral tetrahexylbenzyl side chains of IDT units. Due to the enhanced planarity of phenanthrenequninoxaline unit, the PIDT-phanQ polymer showed higher hole-mobility than PIDT-diphQ. The polymer solar cells fabricated from the blend of polymer and $PC_{71}BM$ exhibit high PCEs of 5.69% and 6.24% for PIDT-diphQ and PIDT-phanQ, respectively. The results indicate that these polymers are promising candidates for the application of polymer solar cells.

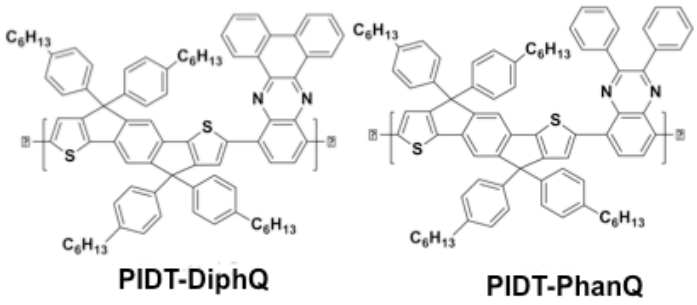

Figure 3-6 Chemical structure of PIDT-diphQ and PIDT-phanQ.

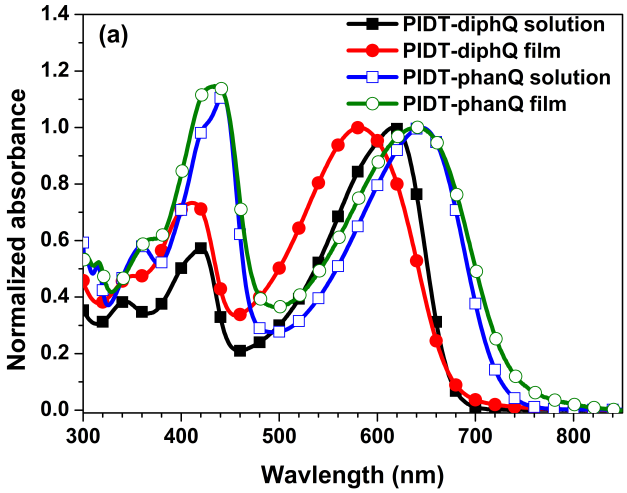

Figure 3-7 UV-Vis spectra of PIDT-diphQ and PIDT-phanQ in chloroform solution and film states.

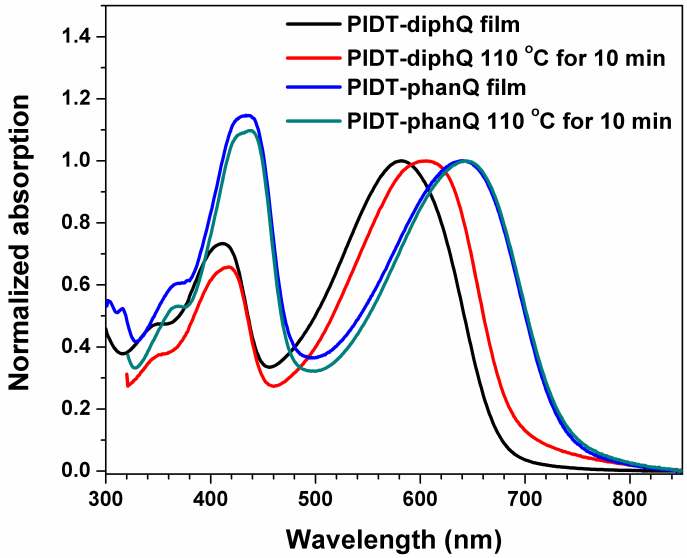

Figure 3-8 The UV-Vis spectra of PIDT-diphQ and PIDT-phanQ films with and without thermal treatment.

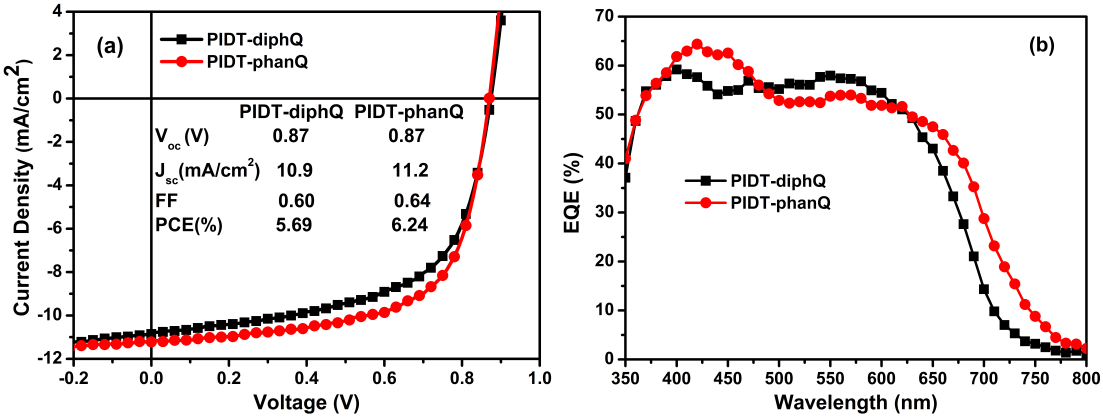

Figure 3-9 (a) The J-V curves of PIDT-diphQ:$PC_{71}BM$ and PIDT-phanQ:$PC_{71}BM$ devices under illumination of AM 1.5G, 100 mW/cm^2. (b) EQE spectra of PIDT-diphQ:$PC_{71}BM$ and PIDT-phanQ:$PC_{71}BM$ devices.

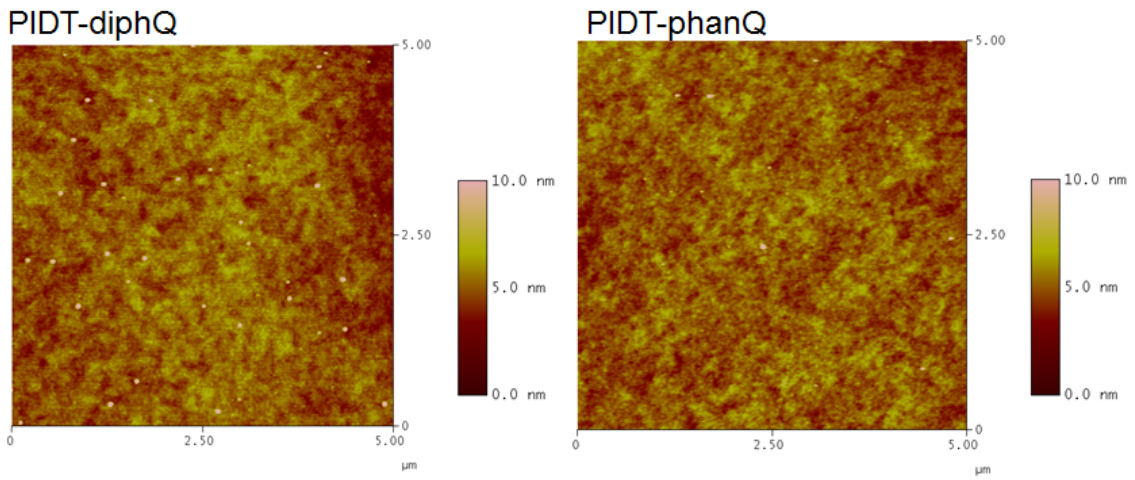

Figure 3-10 AFM figures of PIDT-diphQ/$PC_{71}BM$ and PIDT-phan/$PC_{71}BM$ films

3.4 Dithienobenzoquinoxaline- and Dithienobenzopyridopyrazine - Based Conjugated Polymers[99]

3.4.1 *Introduction*

Alternating donor-acceptor (D-A) conjugated polymers have recently received more and more attention as a viable method to develop low band-gap polymers because of their easily tunable band-gap, energy levels and charge mobility.[100] Among the acceptors, the electron-deficient quinoxaline unit is a quite promising one.[90]–[95] Figure 3-11 shows some reported quinoxaline-based polymers. It can be seen that most of them have a thiophene spacer between donor (such as fluorene, carbazole) and quinoxaline units with the aim of lowering the band-gap in resulting polymers. However, most of these polymers still possess relatively large band-gaps of more than 1.90 eV, which partially limits the further development of quinoxaline-based polymers.[92] As seen from the chemical structure of quinoxaline unit, one can find that there are two ways to further modify the quinoxaline unit which can lead to changes in band-gap and

energy levels of such polymers. One is from the top pyrazine unit, in which different substitutes (such as hydrogen, methyl and phenyl) could be introduced to affect the band-gaps of resulting polymers.[91][92][94][95] Another method is to change the benzene unit in the bottom of quinoxaline unit to more electron deficient moiety (such as pyridine), which could significantly change the band-gap and energy levels of resulting polymers.

Herein, we present two alternating D-A polymers (P1 and P2) based on dithienobenzoquinoxaline (M1) and dithienobenzopyridopyrazine (M2) as the electron-deficient acceptor and an indenodithiophene (IDT) as the electron-rich donor (Figure 3-12). M1 and M2 possess a large fused benzodithiophene ring on top of pyrazine unit, which is different from most quinoxaline units found in the literature. The large fused ring presents some advantages over other quinoxaline units. First of all, the fused dithiophene ring could decrease the steric hindrance compared to the freely rotating dithiophene unit and also form a planar structure to improve the intermolecular stacking of polymers as we have demonstrated in our previous report.[101] Further, the extended π-conjugation in the fused qunioxaline unit will act as a strong electron deficient acceptor, thus resulting a lower band-gap in P1 and P2. [101] In addition, M2 contains a more electron deficient pyridine unit in the bottom that could lead to a smaller band-gap of P2 compared to P1. To this end, polymers P1 and P2 were synthesized *via* Stille polycondensation and their optical, electro-chemical, field-effect transistor and photovoltaic properties were investigated.

3.4.2 *Experimental*

The synthesis of these Conjugated Polymers are fully described elsewhere.[99]

The polymer solar cells were fabrication as following: ITO-coated glass substrates (15 Ω/sq.) were cleaned with detergent, de-ionized water, acetone, and isopropyl alcohol. A thin

layer (ca. 40 nm) of PEDOT:PSS (Baytron® P VP AI 4083, filtered at 0.45 μm) was first spin-coated on the pre-cleaned ITO-coated glass substrates at 5,000 rpm and baked at 140°C for 10 min under ambient conditions. The substrates were then transferred into an argon-filled glove-box. Subsequently, the polymer:$PC_{71}BM$ active layer (ca. 90 nm) was spin-coated on the PEDOT:PSS layer from a homogeneously blended solution. The solution was prepared by dissolving the polymer at a blend weight ratio of 1:3 in o-dichlorobenzene and filtered with a 0.2 μm PTFE filter. At the final stage, the substrates were pumped down to high vacuum ($< 2 \times 10^{-6}$ Torr), and calcium (30 nm) topped with aluminum (100 nm) was thermally evaporated onto the active layer through shadow masks to define the active area of the devices.

The un-encapsulated solar cells were tested under ambient conditions using a Keithley 2400 SMU and an Oriel Xenon lamp (450 W) with an AM1.5 filter. The light intensity was calibrated to 100 mW/cm^2 using a calibrated silicon solar cell with a KG5 filter, which has been previously standardized as the National Renewable Energy Laboratory.

The current-voltage (I-V) characteristics of unencapsulated photovoltaic devices were measured under ambient conditions using a Keithley 2400 source-measurement unit. An Oriel xenon lamp (450 Watt) with an AM1.5 G filter was used as the solar simulator. The light intensity was set to 1 sun (100 mW cm^{-2}) using a calibrated Hamamatsu silicon diode with a KG5 color filter, which can be traced to the National Renewable Energy Laboratory (NREL). The EQE system uses a lock-in amplifier (Stanford Research Systems SR830) to record the short-circuit current under chopped monochromatic light.

3.4.3 *Results and Discussion*

The optical properties of P1 and P2 were investigated in their chloroform solutions and thin films. Figure 3-13 shows the absorption spectra of P1 and P2 in chloroform and thin films. In

chloroform solution, it can be seen that P1 shows two main peaks, the high-energy peak with an absorption maximum at 445 nm comes from the donor part and the low-energy peak with a maximum of 663 nm is due to the charge transfer from donor to acceptor. However, the polymer P2 in chloroform solution shows a significant red-shift on the charge transfer peak with an absorption maximum at 721 nm, while the high-energy peak keeps almost same with that of P1 because the same donor is used in both polymers. It shows that changing to the more electron-deficient pyridine unit in P2 has a large effect on the optical property in comparison with that of P1. The optical band-gap in solution for P1 was determined to be 1.63 eV (760 nm). The optical band-gap of P2 in solution is decreased to 1.51 eV (820 nm) due to the more electron-deficient pyridine in polymer backbone. It is interesting that the UV-Vis spectra of P1 and P2 in thin films (Figure 3-13) exhibit similar features with that in solution. The charge transfer peak for P1 and P2 in thin film is at 651 and 720 nm, respectively. These results suggest that the polymers in solution likely already show a certain degree of packing, which is similar to what is observed in thin film. Further, the fused ring unit also promotes stronger chain stacking in solution and thin film compared with those polymers with free-rotated aromatic rings in quinoxaline unit, in which a significant blue-shift in thin film absorption is observed compared with that in solution.[7] The absorption onsets of P1 and P2 are ~770 and ~835 nm, respectively, corresponding to an optical band-gap of 1.61 and 1.48 eV, respectively. This value is around 0.3-0.6 eV smaller than other quinoxaline-based polymers (Figure 3-11).

The photovoltaic properties of the polymers were first investigated with a conventional device configuration of ITO/PEDOT:PSS/polymer:$PC_{71}BM$ (1:3)/Ca/Al. Device performance was measured under 100 mW/cm^2 AM 1.5 illumination. The active layers were spin-coated from *o*-DCB solutions of polymer and $PC_{71}BM$. The optimized weight ratio between the polymer and

$PC_{71}BM$ is 1:3. $PC_{71}BM$ was used as the electron acceptor due to the complementary absorption to the polymer in the visible region.[102] Figure 3-14(a) shows the J-V curves of the best P1 and P2 devices. The P1 device, shows a V_{oc} of 0.83 V, a short-circuit current density (J_{sc}) of 11.6 mA cm^{-2}, and a fill factor (FF) of 0.63, resulting a high PCE of 6.06%. It is noted that such a high PCE is achieved without any pre- and/or post-treatments, such as thermal annealing, solvent/vapor annealing, or the addition of solvent additives. This is one of the highest PCE reported so far in BHJ PSCs without any thermal or solvent treatments.

Under the same conditions, the P2 device only showed a PCE to 3.21% with a V_{oc} of 0.74 V, a J_{sc} of 10.1 mA cm^{-2} and a FF of 0.43. The low performance in the P2 device is well below what is expected because P2 possesses a lower HOMO energy level potential leading to a higher V_{oc} and lower band-gap which favors a high J_{sc}. Although it is well known that the V_{oc} is dependent on the difference between HOMO energy level of the donor and LUMO energy level of the acceptor,[98][103] there are still some more factors affecting the V_{oc}, such as the cathode, interface resistance and excition non-radiative recombination.[104]–[108] In this case, it is most likely that excition non-radiative recombination at the interface is one of the reasons for the lower V_{oc} and J_{sc} since the pyridine unit may play a role as an electron trap compared with benzene unit in P1.[109] In addition, the lower LUMO level of P2 will also potential have a negative effect on charge separation, thereby resulting in a lower J_{sc} and reducing PCE even further. Having said that, it is interesting that P2 devices are still able to show a J_{sc} of as high as 10 mA cm^{-2}.

To evaluate the accuracy of measurement, the external quantum efficiencies (EQEs) of both devices were measured. The EQE curves of P1 and P2 devices were shown in Figure 3-14(b). The P1 device shows an efficient photoresponse from 350 to 750 nm, and the photoresponse of P2 device extended to around 800 nm as a result of red-shift absorption compared with P1. The

EQE value of P1 device shows more than 40% between 350 and 700 nm with the highest value of 65% at ~400 nm. It is noted that the EQE shows a flat decrease from over 60% at short wavelengths to ~40% at 680 nm, indicating the balanced contribution from the shorter and longer wavelength absorption of P1 and $PC_{71}BM$. However, in P2 device, there is a significant decrease on EQE value from ~65% to 15% between 350 and 800 nm, and the main contribution to the EQE is from $PC_{71}BM$ and the short wavelength absorption of P2. The result is consistent with the lower J_{sc} in P2 device than that in P1 device. The calculated J_{sc} values in P1 and P2 devices are 11.8 and 9.47 mA cm^{-2}, respectively, which are in line with those values measured under AM 1.5G illumination.

The morphology of the polymer and $PC_{71}BM$ blend films were investigated by tapping-mode atomic force microscopy (AFM). Figure 3-15 shows the AFM figures of P1:$PC_{71}BM$ (1:3, w/w) and P2:$PC_{71}BM$ (1:3, w/w) films. Both films show a very smooth surface and small degree of phase separation, which should facilitate charge separation and potentially lead to high performance. The root-mean-square roughness is 0.964 nm and 0.845 nm for P1 and P2 blend films, respectively. It is known that an interpenetrating bi-continuous network between polymer and PCBM with an ideal domain size of 10-20 nm is important for high performance PSCs. Both larger and smaller domain sizes of the blend films are not favorable for efficient charge transfer and separation. In addition, better miscibility and smaller domain sizes between polymer and PCBM should increase the possibility for charge recombination. The smaller roughness and better miscibility of P2 and $PC_{71}BM$ compared to the P1 blend film, could lead to charge recombination, and thus it may be a cause of the low J_{sc} in P2-based device relative to P1-based device. Further detailed studies on the charge transfer and excition separation and recombination are in progress and will report elsewhere.

3.4.4 *Conclusions*

The photovoltaic properties were investigated with the device structure of ITO/PEDOT:PSS/polymer: $PC_{71}BM$ (1:3, w/w)/Ca/Al. A PCE of 6.06% with a V_{oc} of 0.83 V, a J_{sc} of 11.6 mA cm^{-2} and a FF of 0.63 for a P1-based device was achieved without any thermal or solvent treatments. We believe that P1 will be one of the very promising candidates for offering roll-to-roll manufacturing of PSCs.

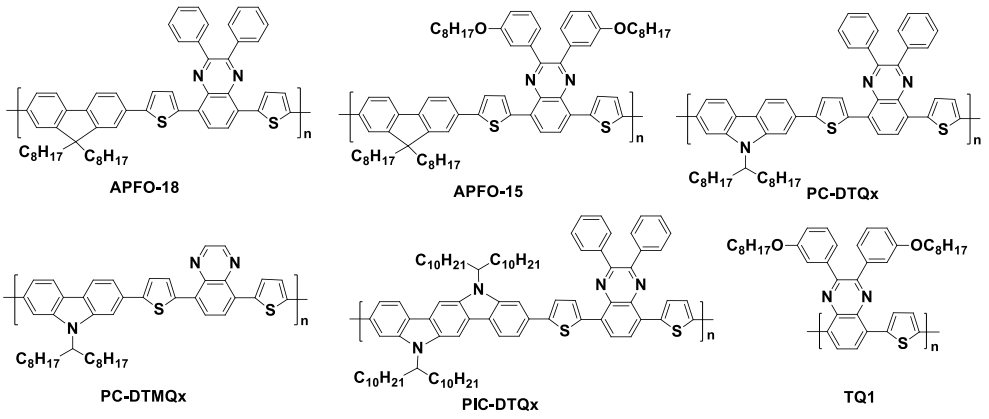

Figure 3-11 The chemical structures of several reported quinoxaline-based polymers.

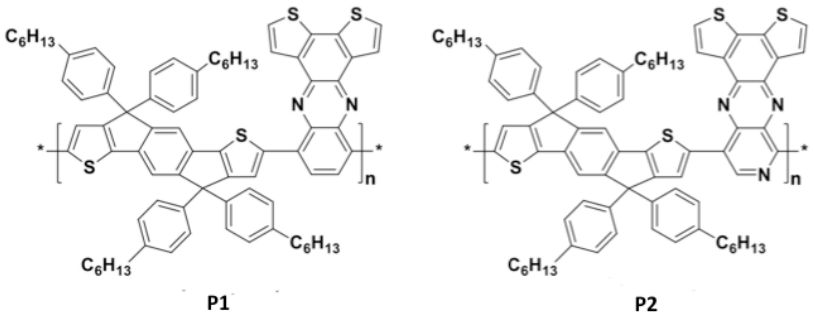

Figure 3-12 The chemical structures of P1 and P2.

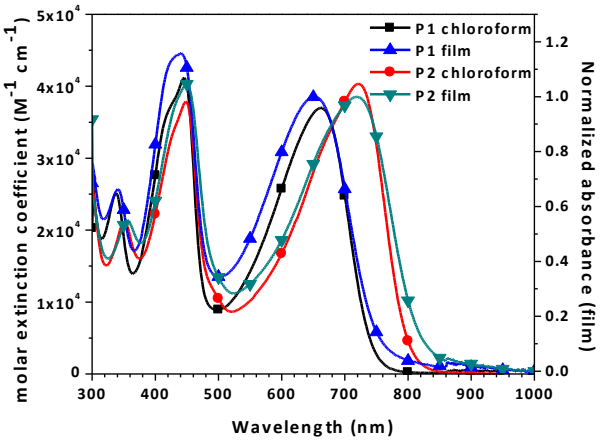

Figure 3-13 UV-Vis absorption spectra of P1 and P2 in chloroform and thin films.

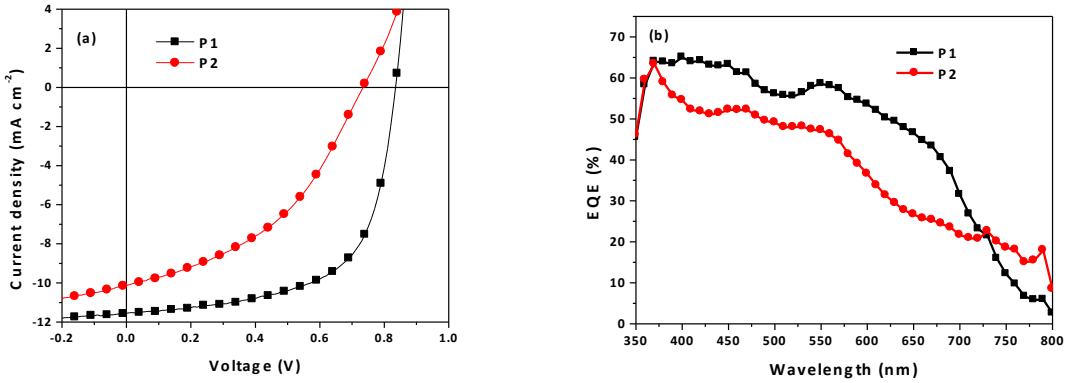

Figure 3-14 J-V curves (a) of P1/$PC_{71}BM$ and P2/$PC_{71}BM$ (1:3 wt) and EQE curves (b) of the conventional devices.

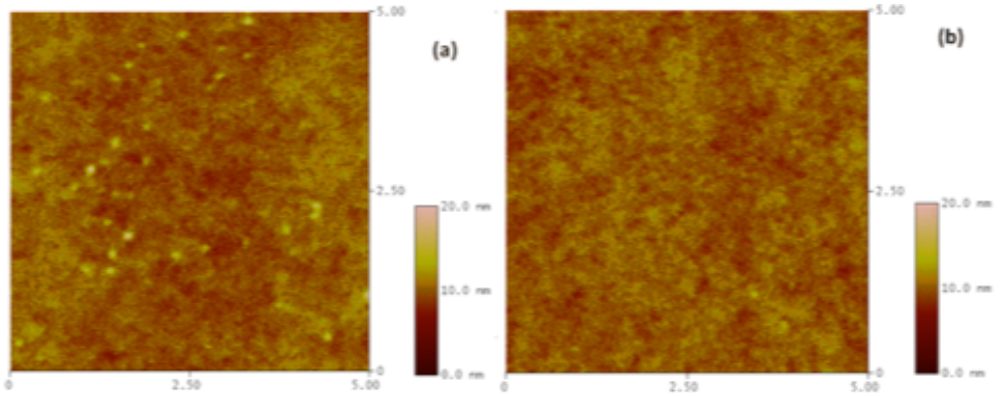

Figure 3-15 AFM figures of P1:$PC_{71}BM$ (1:3, w/w) (a) and P2:$PC_{71}BM$ (1:3, w/w) (b) blend films.

3.5 Partially Fluorinated Cyclopentadithoiphene / Benzothiadiazole Conjugated Polymer[110]

3.5.1 *Introduction*

One of the most important developments for conjugated polymers is the rational design of narrow band-gap polymers to better match the solar spectrum.[65] In general, these polymers are copolymers based on an electron-rich donor (D) and an electron-deficient acceptor (A) on the polymer backbone to facilitate the intramolecular charge transfer between D and A. The molecular units such as carbazole, benzodithiophene, and cyclopentadithiophene, etc. have been used as the donor, and benzothiadiazole, thienothiophene and thienopyrroledione, etc. have been commonly used as the acceptor.[64][70][77][79][80][96][109][111]–[116]

As we known, the morphological control of the BHJ active layer in PSC plays a key role in charge generation, separation and transport within the device. Bazan and Heeger *et al*. have

shown that the morphology of the active blend can be effectively controlled by adding a small amount of high boiling point solvent such as 1,8-dithioloctane (DTO) or 1,8-diiodooctane (DIO) into the polymer solution. For example, the devices made from poly[2,6-(4,4-bis-(2-ethylhexyl)-4*H*-cyclopenta[2,1-b;3,4-*b*']dithiophene)-*alt*-4,7-(2,1,3-benzothiadiazole)] (PCPDTBT) could reach much higher PCE by adding a small amount of DTO or DIO into the PCPDTBT/$PC_{71}BM$ solution in chlorobenzene.[69][81] The optimized PCPDTBT/$PC_{71}BM$ devices showed a J_{sc} of ~15-16 mA cm^{-2}, a V_{oc} of 0.37-0.6 V, a fill factor (FF) of 40-55%, and a PCE of between 3.5 to 5.4%.[69][81][83] However, without solvent additive, the PCPDTBT/PCBM-based devices only gave a PCE of 2.6-3.2% and a low J_{sc} of 8-11 mA cm^{-2} because of the formation of unfavorable morphology.[69][117] Another well-studied polymer, poly [(4,4'- bis (2-ethylhexyl) dithieno [3,2-b:2',3'-d] silole) - 2,6-diyl-alt- ((5-octylthieno [3,4-c] pyrrole-4,6-dione) - 1,3-diyl)] (PDTSTPD), also showed significant morphological changes upon the addition of processing additive. Without DIO in processing solvent, the device performance of PDTSTPD only showed a PCE of less than 1%. After adding 2% DIO, the PCE of PDTSTPD device dramatically increased to ~ 7% due to the improved morphology.[113] These results showed that proper control of the morphology is very critical to improve the overall performance of device. However, these small amounts (0.2-3%) of high boiling point solvent additives are difficult to control and remove afterwards. In addition, the tedious processing conditions are also unfavorable for large-area ink-jet or roll-to-roll printing due to possible residual solvent in the device.[99][118] Therefore, it would be ideal if a conjugated polymer/PCBM blend can be processed from single solvent system to afford optimal morphology for fabricating high-performance PSC. [99][118]

Recently, the introduction of fluorine (F) atom onto conjugated polymer backbone has been proven to be an effective way to enhance the overall performance of PSCs.[119][120] The F atom

plays two important roles: 1) the electron-withdrawing property of F atom can lower the highest occupied molecular orbital (HOMO) energy level, therefore, results in an increased V_{oc} in the corresponding device; 2) F atom can form F-H, F-F bonding through inter- or intra-molecular interactions, which may affect π-π stacking of polymer to fine-tune its morphology with fullerene.

Herein, we report a fluorinated polymer, PCPDTFBT (Scheme 1), synthesized *via* Stille polymerization of monofluoro-substituted benzothiadiazole and distannylcyclopentadithiophene. Better π-π stacking in PCPDTFBT enables the PCPDTFBT/$PC_{71}BM$ blend based PSC to have a promising PCE of 5.51% with higher V_{oc} (~0.75V) compared to its PCPDTBT/$PC_{71}BM$ analog (< 0.6V). Most importantly, this performance was achieved without using any solvent additive. We have also demonstrated that PCPDTFBT can be processed from a non-chlorinated solvent, o-xylene to achieve a high PCE of 5.32%, which is the best performance reported so far for devices processed from non-chlorinated solvents. Furthermore, an even higher PCE of 5.84% could also be achieved after inserting a thin layer of fullerene-containing surfactant between the active layer and Ag cathode to facilitate the extraction of electrons.

3.5.2 *Experimental*

The synthesis of these Conjugated Polymers are fully described elsewhere.[110]

PSCs were fabricated using ITO-coated glass substrates (15 Ω/sq), which were cleaned with detergent, de-ionized water, acetone, and isopropyl alcohol. A thin layer (ca. 30 nm) of PEDOT:PSS (Baytron® P VP AI 4083, filtered at 0.45 μm) was first spin-coated on the pre-cleaned ITO-coated glass substrates at 5,000 rpm and baked at 140°C for 10 min under ambient conditions. The substrates were then transferred into a nitrogen-filled glovebox. Subsequently, the polymer:$PC_{71}BM$ active layer was spin-coated onto the PEDOT:PSS layer. For devices, the

solution was prepared by dissolving the polymer and fullerene at a 1:2 weight ratio in chlorobenzene or in o-xylene overnight and filtered through a 0.2 μm PTFE filter, and the substrates were annealed at 110 °C for 10 min prior to electrode deposition. For the device with surfactant, the Bis-C_{60} surfactant in methanol was spin-coated onto the active layer. At the final stage, the substrates were pumped under high vacuum (< 2×10^{-6} Torr), and calcium (20 nm) topped with aluminum (100 nm) or silver (100 nm) was thermally evaporated onto the active layer. Shadow masks were used to define the active area (10.08×10^{-2} cm^2) of the devices.

The un-encapsulated solar cells were tested under ambient conditions using a Keithley 2400 SMU and an Oriel Xenon lamp (450 W) with an AM1.5 filter. The light intensity was calibrated to 100 mW/cm^2 using a calibrated silicon solar cell with a KG5 filter, which has been previously standardized as the National Renewable Energy Laboratory.

The current-voltage (I-V) characteristics of unencapsulated photovoltaic devices were measured under ambient conditions using a Keithley 2400 source-measurement unit. An Oriel xenon lamp (450 Watt) with an AM1.5 G filter was used as the solar simulator. The light intensity was set to 1 sun (100 mW cm^{-2}) using a calibrated Hamamatsu silicon diode with a KG5 color filter, which can be traced to the National Renewable Energy Laboratory (NREL). The EQE system uses a lock-in amplifier (Stanford Research Systems SR830) to record the short-circuit current under chopped monochromatic light.

3.5.3 *Results and Discussion*

3.5.3.1 Performance of devices processed from chlorobenzene solutions

The photovoltaic devices of PCPDTFBT were investigated in the configuration of ITO/PEDOT:PSS/polymer:$PC_{71}BM$/Ca/Al. PCPDTBT-based devices were also made under the

same condition for direct comparison. Detailed fabrication and characterization are shown in the experimental section. The J-V curves of PCPDTFBT/$PC_{71}BM$ and PCPDTBT/$PC_{71}BM$ devices were shown in Figure 3-17a. The optimized polymer to $PC_{71}BM$ ratio is 1:2. The active layers were processed from their pure CB solutions without any additive. The device performances were shown in Table 1. The PCPDTFBT/$PC_{71}BM$ device showed a promising PCE of 5.51% with a V_{oc} of 0.75 V, a J_{sc} of 15.0 mA cm^{-2}, and a FF of 49%. However, the PCPDTBT/$PC_{71}BM$ device only gave lower values with a V_{oc} of 0.65 V, a J_{sc} of 10.1 mA cm^{-2}, and a FF of 42% which results in a PCE of 2.75%. The theoretical V_{oc} is calculated to be 0.75 V and 0.62 V under the theoretical equation of $V_{oc} = \frac{1}{e}\left(\left|E_{HOMO}^{donor}\right| - \left|E_{LUMO}^{PCMB}\right|\right) - 0.3V$ considering the LUMO level of PCBM to be -4.10 eV.[16, 40]

The external quantum efficiency (EQE) curves of devices were shown in Figure 3-17b. It can be seen that the devices showed broad response over the range of 350 to 900 nm. The EQE value between 400 nm to 800 nm for PCPDTFBT devices is more than 50% compared to ~35% for PCPDTBT devices, which is consistent with the result of measured J_{sc}. The integrated J_{sc} from EQE is 10.4 and 14.8 mA cm^{-2}, respectively for PCPDTBT and PCPDTFBT devices, showing the accuracy of measurements. The significantly improved performance in PCPDTFBT/$PC_{71}BM$ device is mainly attributed to higher V_{oc} and J_{sc}.

It is known that the V_{oc} of PSC is proportional to the difference between the HOMO level of polymer and the LUMO level of $PC_{71}BM$, regardless of the cathode modifications. Therefore, the lower lying HOMO level (-5.15 eV) of PCPDTFBT compared to PCPDTBT (-5.02 eV) contributes to the increased V_{oc}. In general, the J_{sc} of a PSC is relevant to the charge mobility and morphology of a BHJ blend. Higher hole mobility measured in PCPDTFBT should also contribute to the higher J_{sc} and FF observed in PCPDTFBT/$PC_{71}BM$ device. It is well known that

proper control of nanoscale morphology of the active layer is also very crucial to the performance of PSCs. Too large or too small phase separation (domains) is not favorable for efficient charge separation, which may lead to severe charge recombination. Figure 3-18 and Figure 3-19 showed the TEM and AFM images of the thin film blends of PCPDTBT and PCPDTFBT with $PC_{71}BM$, which were prepared from their CB solutions. As shown in Figure 3-18, amorphous film was found in PCPDTBT blend film, which is similar to that observed previously.[30][81] The smaller size of phase separation in PCPDTBT blend film increased the possibility for charge recombination, therefore, resulted in lower J_{sc} and FF.[64] Under the same condition, the larger size of phase separation was observed in PCPDTFBT blend film, which is similar to the excition diffusion lengths, leading to more efficient charge separation and transport. The AFM images in Figure 3-19 further provide the evidence for larger phase separation in PCPDTFBT/$PC_{71}BM$ compared to that of PCPDTBT/$PC_{71}BM$. In the PCPDTBT/$PC_{71}BM$ case, it showed a smaller RMS of 0.504 nm compared to 1.205 nm for PCPDTFBT/$PC_{71}BM$, which may increase the possibility for charge recombination.

As a result, higher J_{sc} and FF values were obtained in the PCPDTFBT-based device. By combining higher V_{oc}, J_{sc}, and FF, a higher PCE (5.51%) could be reached in PCPDTFBT-based device compared to 2.75% for the PCPDTBT-based device. It is worthy to note that these values were obtained from the pure CB solution of PCPDTFBT/$PC_{71}BM$, without adding any additive. The attempt to add 2-3% of DIO didn't further increase the performance of the device. However, the PCPDTBT device with 2% DIO showed an increased PCE (3.69%) with similar J_{sc} but lower V_{oc} (0.59 V).

3.5.3.2 Performance of device processed from o-xylene solution

As discussed above, processing solvent is a critical parameter in determining the performance of polymer solar cells.[121]–[123] In literature, most of the efficient BHJ solar cells were processed using chlorinated solvents, such as DCB and CB, to afford better morphology due to better solubility and viscosity compared to other solvents.[20][69][96][114][124] However, chlorinated solvents are not suitable for large scale production due to their high cost, toxicity, and environmental issues. Therefore, it is highly desirable to find an alternative solvent that can be used to afford appropriate morphology during thin film processing to lead to high efficiency PSCs. O-xylene is a good choice because of the similar boiling point and viscosity compared to CB. The most studied polymer using o-xylene as solvent is P3HT because of its good solubility.[125]–[127]

There is very little information about D/A polymer based device that can be processed from o-xylene solution to show good efficiency. Since PCPDTFBT has good solubility in o-xylene, the active layer of its photovoltaic device can also be processed from o-xylene solution. Figure 3-20a shows the J-V curve of PCPDTFBT/$PC_{71}BM$ device processed from o-xylene solution. The device showed a V_{oc} of 0.77 V, a J_{sc} of 14.4 mA cm^{-2}, and a FF of 48%, which results in an overall PCE of 5.32% (*Table 3-2*). This is comparable to device processed from CB solution. To our knowledge, it is one of the highest values reported in literature for device processed from non-chlorinated solvents. This performance is attributed to the appropriate morphology achieved for the blend (Figure 3-20b). The PCPDTFBT/$PC_{71}BM$ film processed from o-xylene solution showed the similar phase separation as the film processed from CB solution (Figure 3-19).

2.5.3. Device performance with hybrid electron-collecting layer/Ag cathode

Cathode modification for organic electronics has received much attention because the interface between active layer and electrode is critical for achieving optimal device

performance.[107][128][129] Water-/alcohol-soluble polymers or polyelectrolytes have been employed as effective interfacial modification materials for improving the performance of PSCs.[128][130] Recently, we have reported a new alcohol-soluble, bis-adduct fullerene surfactant and its function as an efficient electron selective material when inserted as a thin layer between the active material and high work function cathode, such as Al or Ag.[131] We have adapted this approach here to improve the performance of PCPDTFBT-based devices. The device were fabricated with the configuration of ITO/PEDOT:PSS/PCPDTFBT:$PC_{71}BM$/C_{60}-Bis/Ag. The C_{60}-Bis was spin-coated from its methanol solution. Ag was selected as cathode because it is air stability and good reflectivity. Figure 3-21 shows the J-V curve of PCPDTFBT/$PC_{71}BM$ device with Bis-C_{60} surfactant as the electron-collecting layer. The PCE was further improved to be 5.81% (with a V_{oc} of 0.76 V, a J_{sc} of 15.0 mA cm^{-2}, and a FF of 51%, *Table 3-2*), which is even higher than the device with Ca/Al as cathode. This enhancement may be attributed to the efficient charge collection and as an optical buffer between active layer and cathode. [131]

3.5.4 *Conclusions*

We have designed and synthesized a partially fluorinated low bandgap polymer, PCPDTFBT. By introducing F atom onto the BT unit, PCPDTFBT exhibited better π-π stacking in solution than PCPDTBT. The PSC processed from the solution of PCPDTFBT/$PC_{71}BM$ in CB showed a high PCE of 5.51% compared to 2.75% for PCPDTBT/$PC_{71}BM$ based device that was fabricated under the same condition. The increased V_{oc} is believed to be the result of lower lying HOMO in PCPDTFBT. The larger phase separation on the order of excition diffusion length and the balanced ambipolar charge mobility contributed to the enhanced J_{sc}. These results showed that the introduction of F atom provides an effective way to simultaneously improve V_{oc} and

morphology. Most importantly, there is no need to add any solvent additive to control the morphology of active layer.

Furthermore, PCPDTFBT could also be processed from o-xylene and its PSC showed a PCE of 5.32%, which is among the best performance for donor-acceptor type polymers processed from non-chlorinated solvents. In addition, the PCE of PCPDTFBT device could also be increased to reach 5.81% by inserting a thin layer of fullerene-containing surfactant between the active layer and Ag cathode. These encouraging results showed that PCPDTFBT has the potential to be used as a low bandgap polymer to provide complementary absorption in tandem solar cells.

Table 3-2 The device performance of PCPDTFBT and PCPDTBT devices.

active layer (solvent)	**cathode**	**V_{oc} (V)**	**J_{sc} (mA cm^{-2})**	**FF (%)**	**PCE (%)**
PCPDTBT/$PC_{71}BM$ (o-DCB)[a]	Ca/Al	0.65	10.1	42	2.75
PCPDTFBT/$PC_{71}BM$ (o-DCB)[b]	Ca/Al	0.75	15.0	49	5.51
PCPDTFBT/$PC_{71}BM$ (o-xylene)[c]	Ca/Al	0.77	14.4	48	5.32
PCPDTFBT/$PC_{71}BM$ (o-DCB)[b]	Bis-C60/Ag	0.76	15.0	51	5.81

[a]: ~95 nm; [b]: ~120 nm; [c]: ~110 nm

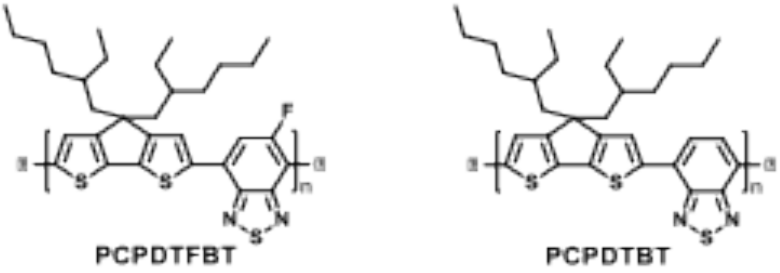

Figure 3-16 The chemical structures of PCPDTBT and PCPDTFBT.

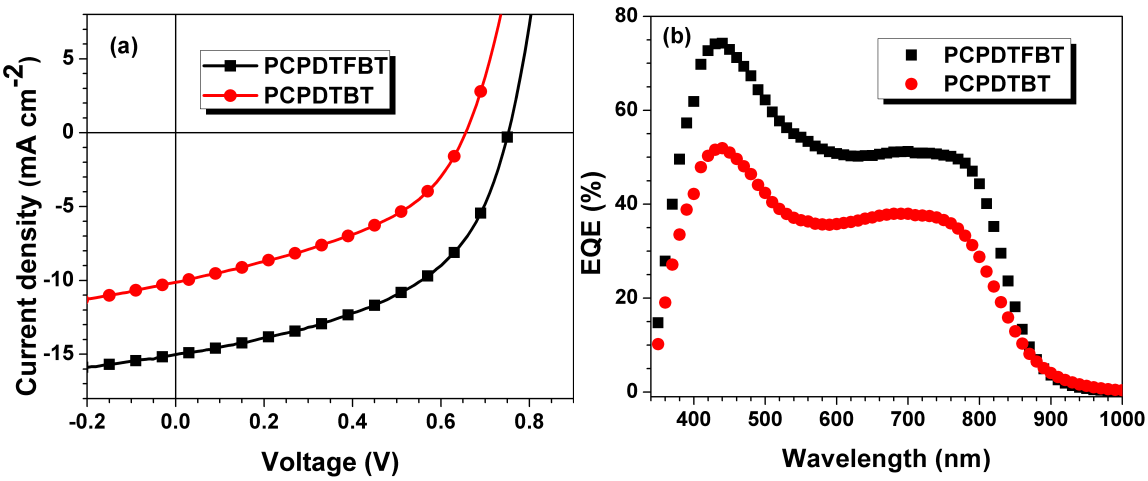

Figure 3-17 The J-V (a) and EQE (b) curves of PCPDTFBT and PCPDTBT devices processed from chlorobenzene solutions.

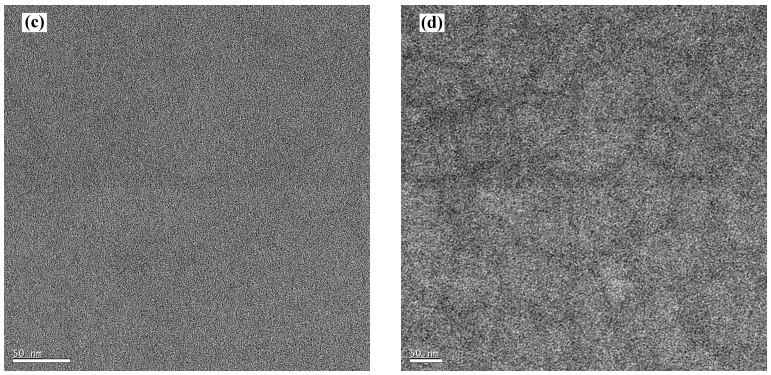

Figure 3-18 The TEM images of PCPDTBT/$PC_{71}BM$ and PCPDTFBT/$PC_{71}BM$ films processed from chlorobenzene solutions. The scale bar is 50 nm.

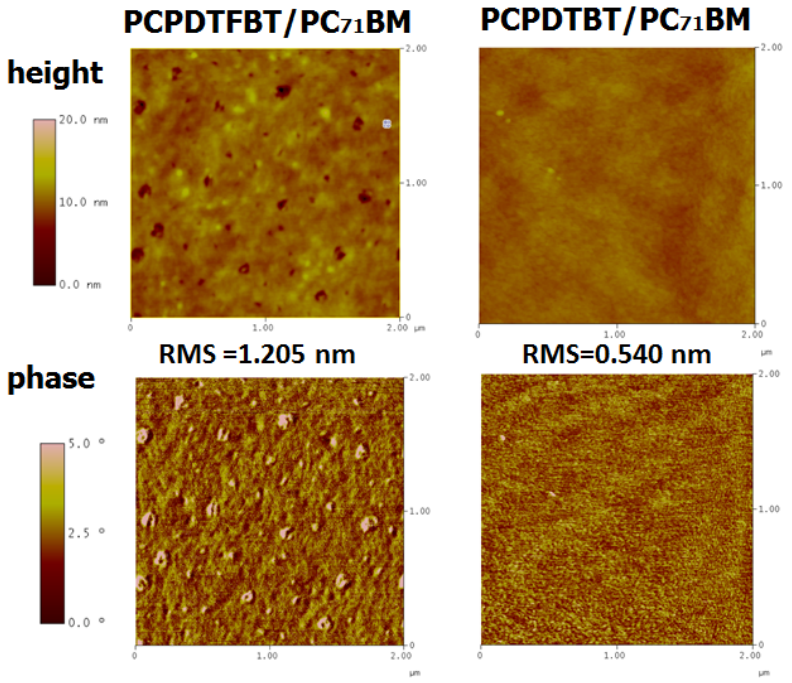

Figure 3-19 The tapping mode AFM images of PCPDTFBT/$PC_{71}BM$ and PCPDTBT/$PC_{71}BM$ films processed from chlorobenzene solutions.

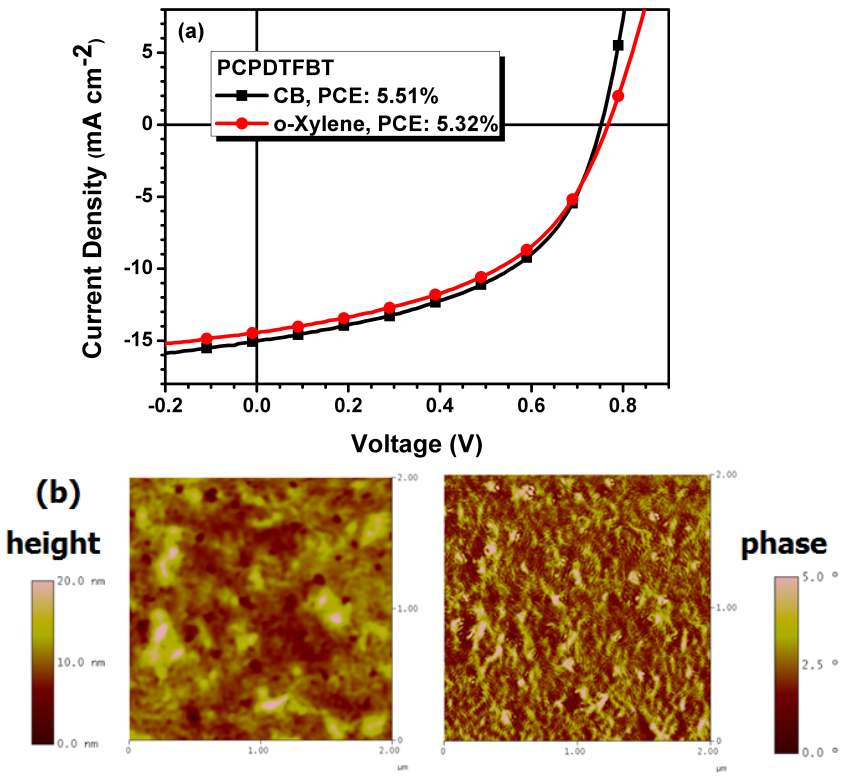

Figure 3-20 (a) The J-V curves of PCPDTFBT/$PC_{71}BM$ devices processed from CB and o-xylene solutions. (b) The AFM images of PCPDTFBT/$PC_{71}BM$ films processed from o-xylene solution.

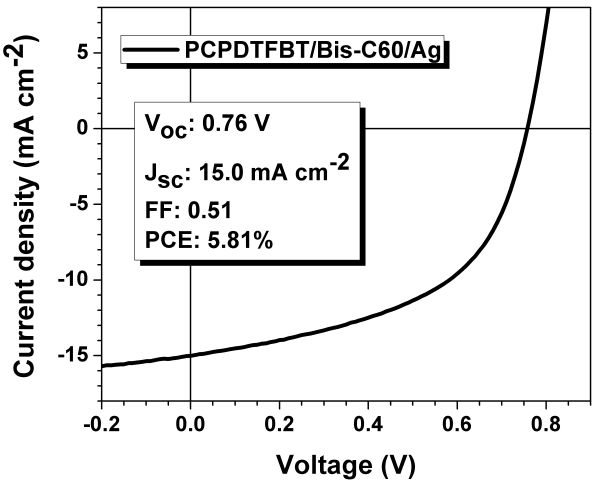

Figure 3-21 The J-V curve of PCPDTFBT-based device with Bis-C_{60} surfactant as an electron-collecting layer and Ag as cathode.

3.6 Tailoring Side-Chains for Cyclopentadithiophene/Fluoro-benzothiadiazole Based Low Bandgap Polymers[132]

3.6.1 *Introduction*

The power conversion efficiency (PCE) of single junction PSCs has reached more than 9% in recent reported devices.[133] However, there are still challenges to further improve the PCE of these devices. The main limitations lie on that polymers cannot absorb light efficiently to generate enough charge carriers and their intrinsically low mobilities. By stacking both wide and small band gap polymers into tandem solar cells, light absorption can be enhanced while minimizing photon energy loss, to provide PCEs higher those of single junction cells.[134] One of the problems that impede the progress of tandem solar cells is the lacking of high-performance low band gap polymers (Eg < 1.5 eV).[135][136] Therefore, it is an important task to develop suitable small band gap polymers that can be used to fabricate PSCs with reduced energy loss and increased photocurrent density.

Recently, a low band gap polymer poly[2,6-(4,4-bis(2-ethylhexyl)-4H-cyclopenta[2,1-b;3,4-b']dithiophene)-alt-4,7 (monofluro-2,1,3-benzothiadiazole)] PCPDTFBT has been reported by Jen[110] and Neher[36] which possesses a small band gap (E_g) of 1.44 eV. A relatively high PCE of 5.51% could be achieved without using any solvent additives for device fabrications. The resulting devices could reach an open-circuit voltage (V_{oc}) of 0.75 V and a short-circuit current density (J_{sc}) of 15.0 mA cm^{-2}. However, these devices only showed a relatively low fill factor (FF) of 0.49. Although this polymer can be considered for use in tandem solar cells, its high lying highest occupied molecular orbital (HOMO) energy level limits the V_{oc} of the resultant cell.

Owning to electron-withdrawing character of fluorine (F) atom, conjugated polymers with F groups functionalized on their backbones usually exhibit lower HOMO energy levels, thus it can increase the V_{oc} of the corresponding device.[117][118][135] We have previously introduced difluorobenzothiadiazole to further deepen the HOMO level of the PCPDTFBT polymer. As expected, the new polymer poly[2,6-(4,4-bis(2-ethylhexyl)-4Hcyclopenta[2,1-b;3,4-b'] dithiophene)-alt-4,7-(difluro-2,1,3 -benzothiadiazole)] (PCPDTDFBT) showed an increased V_{oc} of 0.84 eV, which is about ~ 0.1 eV higher than that of PCPDTFBT. This V_{oc} is one of the highest among currently available low band gap polymers. Nevertheless, the solubility of PCPDTDFB is quite poor due to enhanced F–H, F–F interactions and strong stacking of polymer. It strongly limits its processibility, which can only be processed through hot o-DCB. This not only hampers the formation of good quality film, but also creates significant problem for device fabrication.

In order to have high V_{oc}, while maintaining good solution processibility of the polymer, we have devoted significant effort in engineering its alkyl side-chains. It has been proven to be an effective way to tune the solubility of polymers. Müllen *et al*.[135] have demonstrated the use of

long linear alkyl chains C_{16} instead of shorter branched $C_{2,8}$ to enhance stacking of polymers and achieve ultrahigh mobility (3.3 $cm^2 V^{-1}s^{-1}$). Pei *et al*.[136] have reported that significantly enhanced mobility of isoindigo-based polymers could be achieved through subtle modifications of their alkyl chains. Very recently, You *et al*.[137] have also investigated a series of naphtho[2,1-b:3,4-b'] dithiophene (NDT) and 4,7-di(thiophen-2-yl) benzothiadiazole (DTBT) containing conjugated polymers with different side-chains and F-substituents to show significantly improved PCE (form 1.9% to 5.6%).

Herein, we report the systematic study of a series of cyclopentadithiophene-based conjugated polymers with varied side-chain patterns and F-substituents for developing high efficiency, low band gap polymers for tandem solar cells. To our surprise, the replacement of shorter and bulkier 2-ethyl-hexyl (EH) side-chain with longer 3,7-dimethyl-octyl (DMO) side-chain resulted in significant changes to the optical, electrochemical, and morphological properties of the polymers, as well as the subsequent performance of devices made from these materials. To investigate the underlying mechanism behind this, we have conducted a thorough device, spectroscopic and theoretical analysis to correlate the polymer structure–performance. It was found that the variation of type and length of the alkyl side-chain is critical to the molecular packing behavior. As a result, it caused significant deviation in the photovoltaic properties of polymer devices. This finding may provide insight for making more efficient low band-gap polymers.

3.6.2 *Experimental*

The synthesis of these Conjugated Polymers are fully described elsewhere.[130]

UV-Vis spectra were obtained using a Perkin-Elmer Lambda-9 spectrophotometer. X-Ray diffraction measurements were performed on a Bruker D8 X-ray diffractometer using a Cu-Ka source.

ITO-coated glass substrates (15 Ω/sq.) were cleaned with detergent, de-ionized water, acetone, and isopropyl alcohol. A thin layer (ca. 35 nm) of PEDOT:PSS (Baytron® P VP AI 4083, filtered at 0.45 μm) was first spin-coated on the pre-cleaned ITO-coated glass substrates at 5,000 rpm and baked at 140°C for 10 minutes under ambient conditions. The substrates were then transferred into an argon-filled glove-box. Subsequently, the polymer : $PC_{71}BM$ active layer (ca. 90 nm) was spin-coated on the PEDOT:PSS layer at 600 rpm from a homogeneously blended solution. The solution was prepared by dissolving the polymer and fullerene at weight ratios of 1:2 in chlorobenzene to a total concentration of 12mg/mL at 110°C overnight and filtered through a PTFE filter (0.45 μm). All of the substrates were placed on the hot plate at 110°C for 10min. After annealing, substrates were briefly transferred out of the glove box (total ambient exposure <10 min) and a 10 nm thick film of C_{60}-bis surfactant (1 mg/mL in methanol) was spin-coated at 5k rpm. The substrates were then transferred back into the glove box and annealed at 110 °C for 5 min to drive off any remaining solvent prior to metal deposition. At the final stage, the substrates were pumped down to high vacuum ($< 2 \times 10^{-6}$ Torr), and silver (100 nm) was thermally evaporated onto the active layer. Shadow masks were used to define the active area (10.08×10^{-2} cm^2) of the devices.

The un-encapsulated solar cells were tested under ambient conditions using a Keithley 2400 SMU and an Oriel Xenon lamp (450 W) with an AM1.5 filter. The light intensity was calibrated to 100 mW/cm^2 using a calibrated silicon solar cell with a KG5 filter, which has been previously standardized as the National Renewable Energy Laboratory.

The current-voltage (I-V) characteristics of unencapsulated photovoltaic devices were measured under ambient conditions using a Keithley 2400 source-measurement unit. An Oriel xenon lamp (450 Watt) with an AM1.5 G filter was used as the solar simulator. The light intensity was set to 1 sun (100 mW cm^{-2}) using a calibrated Hamamatsu silicon diode with a KG5 color filter, which can be traced to the National Renewable Energy Laboratory (NREL). The EQE system uses a lock-in amplifier (Stanford Research Systems SR830) to record the short-circuit current under chopped monochromatic light.

3.6.3 *Results and discussion*

The chemical structures of four polymers EH-FBT, EH-DFBT, DMO-FBT, DMO-DFBT are shown in Figure 3-22**.** The UV-Vis absorption spectra of cyclopentadithiophene (CPDT) based polymers were investigated in CB/DCB solutions and in thin film (Figure 3-23). Due to the poor solubility of EH-DFBT, it can only be dissolved in hot o-DCB. The rest of the polymers can all be dissolved in CB. All these polymers show the same two characteristic peaks resulting from similar polymer main chains (Figure 3-22a). The longer wavelength band is due to the intramolecular charge transfer (ICT) between CPDT and BT units. The double peak at the low energy absorption band of EH-FBT (776 nm) is attributed to the strong aggregation of polymer backbone The absorption spectra of all polymer thin films showed a marked red-shift compared to those measured in solution, which can correlate with their solid-state packing. The new peaks at 757 and 759 nm for EH-DFBT and DMO-DFBT in films indicate a more ordered structure in the solid state due to stronger inter-chain packing. The edge of the absorption bands of EH-FBT, EH-DFBT, DMO-FBT, DMO-DFBT in films are 863, 904, 832, and 848 nm, respectively. The corresponding optical bandgaps of these polymers were estimated to be 1.44, 1.37, 1.49 and 1.46 eV by extrapolating from the absorption edge of these films. However, the absorption of EH-

DFBT and DMO-DFBT blue-shifted in both solution and solid-state compared with those of EH-FBT and DMO-FBT. This may be due to the fluorine atoms affect more on the HOMO than on the LUMO. As a result, the bandgap becomes larger when difluoro-benzothiadiazole was introduced onto the polymer.

To gain deeper insight of the nature of the molecular stacking of the polymers, X-ray diffraction analysis on films of the polymer was performed (Figure 3-24). The reflections at 4.5 and 8.0 were related to the polymer lamellar spacing, and the stacking distances between coplanar conjugated polymers were represented at 21.5-25.4. Shorter lamellar spacing by ~8 Å for the EH-based polymers can be found. This inference can be attributed to the longer side chain length of DMO, thus slightly increasing the spacing. Interestingly, except in the case of DMO-FBT, all polymers showed two diffraction peaks, which indicate less structural organization in the DMO-FBT film. It was most likely due to the long and branched DMO side-chains weakening the intermolecular interactions between polymer chains. This explanation is also supported by the UV spectra, in which EH-FBT, EH-DFBT and DMO-DFBT all showed a shoulder peak at long wavelengths (resulting from stacking). However, when FBT was replaced with DFBT in DMO-DFBT, a significant change in polymer packing is observed. The polymer showed clear π–π stacking signal, which can be attributed to the increased inter- or intra-molecular interactions from F–H, F–F interactions. The π–π stacking distance of DMO-DFBT was 3.5 Å, while EH-FBT and EH-DFBT were 3.8 Å and 4.1 Å. All of them were very small for semiconducting polymers, which explains the reason why high mobility could be obtained for OFETs made from these polymers.

It is quite interesting to see that significant changes in the optical, electrochemical, and morphological properties could be observed in these polymers by only changing very slightly of

their structures. Furthermore, significant differences in PCE (as much as four fold from 1.29% to 5.48%) could be noted in their BHJ devices. In order to fairly compare these data and accurately interpret the structure-property relationships, the photovoltaic devices were all made under the same condition. All devices were investigated in the configuration of ITO/PEDOT:PSS/polymer:$PC_{71}BM$/Ca/Al. The optimized polymer to $PC_{71}BM$ ratio is 1:3. The active layers were processed from their pure CB solutions without using any additive, except EH-DFBT, which was processed from o-DCB solution, because of its poor solubility in CB. The current-voltage characteristics of the solar cells are shown in Figure 3-25(a) with representative performance parameters listed in Table 3-3.

As shown in Table 3-3, large differences in V_{oc} could be observed due to differences in these polymers' electronic properties. It is well known that the V_{oc} of a PSC is proportional to the difference between the HOMO level of polymer and the LUMO level of $PC_{71}BM$. By lowering the HOMO level results in a higher V_{oc}. When DFBT is used instead of FBT, an increase of ~0.08-0.09 V is seen in the V_{oc}. Surprisingly, the replacement of the shorter and bulkier side-chains with longer side-chains resulted in a significantly increased HOMO level. As a result, the V_{oc} decreased for almost 0.1 V. It is believed that the electronic properties of a conjugated polymer are mainly determined by its conjugated backbone, whereas the attached alkyl side-chains were thought to be irrelevant. Recently, Gadisa et al.[138] found that longer side-chains tend to lower the HOMO level of the polymer. Li et al.[139] also reported that the substitution of longer/branched alkyl chains on CPDT lowered the HOMO energy level and increased Voc. Very recently, similar phenomena was also observed by Thompson et al. in P3HT-based polymers.[140] However, this is contradictory to our study that the HOMO levels actually increased with the increase of the side-chain length. This may be explained by the

enhanced intermolecular interactions due to stronger p-p stacking of the DMO side-chain substituted polymer.

Meanwhile, the large change of J_{sc} and FF could also be observed by replacing the shorter and bulkier side-chains of EH-FBT with the longer side-chains of DMO-FBT to result in a dramatically decreased J_{sc} from 14.5 mA/cm^2 to 4.76 mA/cm^2. Nevertheless, the introduction of DFBT brought J_{sc} back to 11.6 mA/cm^2. Since J_{sc} of a PSC is closely related to the charge mobility and optical absorption, in order to verify the reason for the decreased Jsc, the external quantum efficiency (EQE) of polymer/$PC_{71}BM$ devices were measured and shown in Figure 3-25 (b). It can be seen that the J_{sc} values calculated from the EQE curves under the standard AM 1.5G conditions match well with those obtained from the J−V measurements. The devices showed broad response over the range 350−900 nm. The EH-FBT showed the highest EQE value (50%) between 400 to 800 nm compared to 30% for EH-DFBT, 10% for DMO-FBT and 40% for DMO-DFBT, which is consistent with the result of measured J_{sc}. It has been proved by UV-Vis and XRD, DMO said-chains may weaken the intermolecular interaction between polymers and decrease the crystallinity, also, the long and branched side-chain can hinder the intercalation of PCBM into polymers. All of these can contribute to higher exciton recombination rate and inefficient charge transport, result in lower EQE and J_{sc}. With a stronger F−H, F−F interactions from DMO-DFBT, a better packing of polymer chains results in a significant improve EQE and J_{sc}.

3.6.4 *Conclusions*

In conclusion, we have thoroughly investigated how alkyl side- chain and fluorine substitution affect the photovoltaic properties of cyclopentadithiophene-based conjugated polymers. To our surprise, when the shorter and bulkier EH side-chains were substituted with the

longer 3,7-dimethyl-octyl (DMO) side-chains, significant changes in their electronic properties and morphology could be observed. The increased HOMO level is believed to be the result of the stronger intermolecular polymer interactions with the longer chain of DMO. Correspondingly, a significant decrease was noted in the Voc. Meanwhile, the π–π stacking distances also change, affecting mobility in OFET devices, where the smaller π–π stacking distances in the polymer film resulted in higher mobility and FF in their corresponding solar cells. Overall, our results indicate that F-substitution and side-chain tuning help optimize π–π stacking, polymer crystallinty, and solubility, which provide significant insight for the development of new generation low band-gap materials design.

Table 3-3 Summarized performances of devices containing EH-FBT, EH-DFBT,DMO-FBT and DMO-DFBT

Polymer	V_{oc}/ V	J_{sc}/ mA cm^{-2}	FF/ (%)	PCE/ (%)
EH-FBT	0.76	14.50	0.50	5.48
EH-DFBT	0.84	9.59	0.42	3.37
DMO-FBT	0.65	4.76	0.41	1.29
DMO-DFBT	0.76	11.80	0.41	3.67

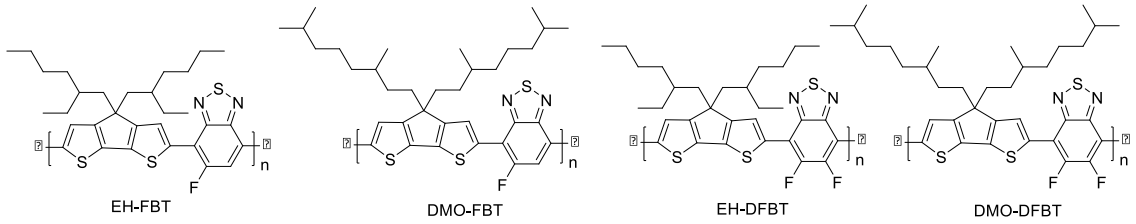

Figure 3-22 Chemical structure of polymers EH-FBT, EH-DFBT, DMO-FBT, DMO-DFBT

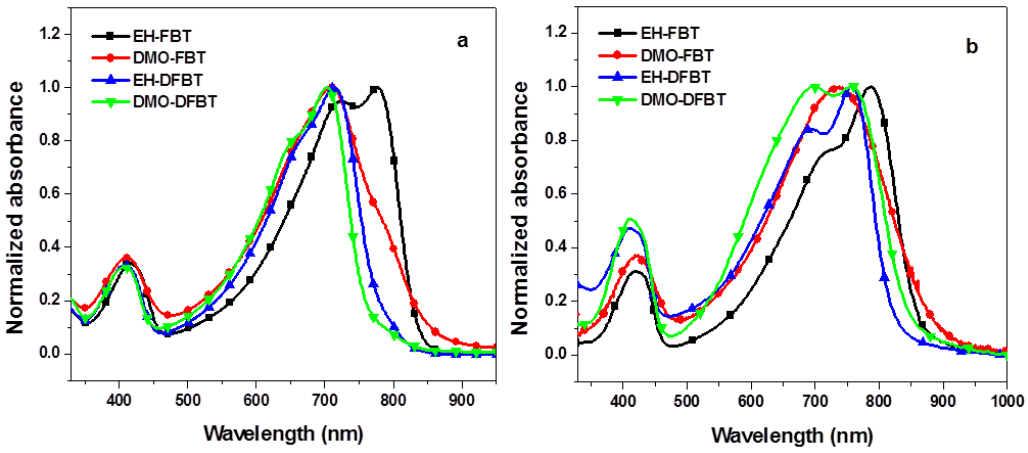

*Figure 3-23 The UV-Vis spectra of EH-FBT, EH-DFBT, DMO-FBT, DMO-DFBT in solution (a) and **in** thin film (b).*

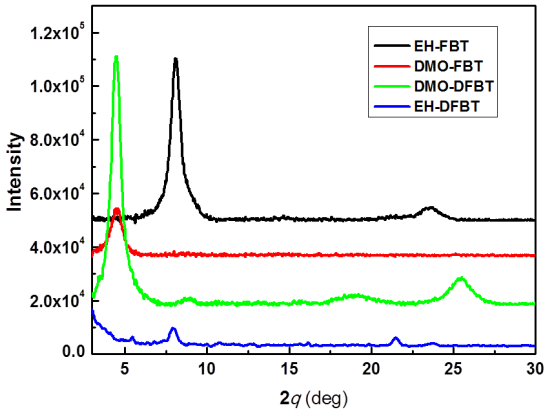

Figure 3-24 X-ray diffraction analysis of EH-FBT, EH-DFBT, DMO-FBT and DMO-DFBT after annealing them at 150 °C for 20 min.

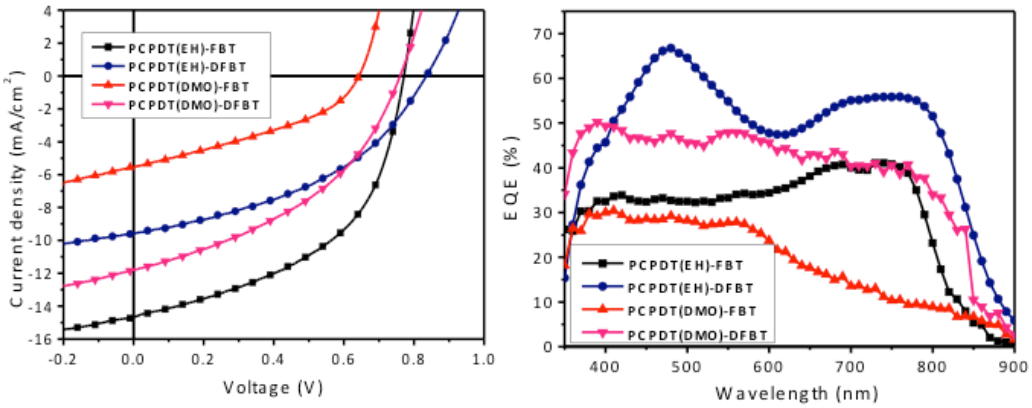

Figure 3-25 J−V (a) and EQE (b) curves of EH-FBT, EH-DFBT, DMO-FBT and DMO-DFBT devices

Chapter 4. INTEGRATE HIGH-PERFORMANCE POLYMER INTO INVERTED POLYMER SOLAR CELLS: DEVICE CHARACTERIZATION, OPTICAL MODELING, AND HOLE-TRANSPORTING MODIFICATIONS [141]

4.1 INTRODUCTION

Previously, we have demonstrated that high efficiency inverted devices with good ambient stability could be achieved in the BHJ layer made of poly (3-hexylthiophene) (P3HT) and [6,6]-phenyl-C_{61}-butyric acid methyl ester ($PC_{61}BM$).[142] Since then, numerous studies have been conducted on the same active material system trying to develop deeper understanding of interface,[142]–[144]optical field distribution,[22]–[24] and vertical phase separation in BHJ active layer on affecting device performance.[39] Because of the intrinsic limitation of light harvesting in the P3HT/$PC_{61}BM$ system, the PCE of most of the inverted structure PSCs studied so far are in the range of 3-4%, which are lower than those obtained from conventional PSCs. [25][26]

Recently, there are several reports showed inverted devices with >6% PCE could be achieved by incorporating newly developed donors.[148][149] With the rapid development of new polymer donors, there is a substantial room for further improvement of inverted devices. In this paper, we report the comprehensive study of a series of conventional and inverted structure devices using poly (indacenodithiophene-*co*-phananthrenequinoxaline) (PIDT-PhanQ) and [6,6]-phenyl-C_{71}-butyric acid methyl ester ($PC_{71}BM$) as the active material with different polymer:fullerene blending ratios.

The chemical structure and energy diagram of PIDT-PhanQ and $PC_{71}BM$ are shown in Figure 4-1 (a) and (b). Previously, we have shown that the PCE of conventional structure PSCs based on the blend of PIDT-PhanQ and $PC_{71}BM$ can reach over 6% at an optimized 1:3

polymer:fullerene blending ratio.[99] However, a higher fullerene content of 1:4 is needed in the BHJ films of inverted cells in order to achieve higher device efficiency. To better understand the effect of the blend compositions on photovoltaic performance of these device architectures, we have correlated their current-voltage (J-V) characteristics and external quantum efficiency (EQE) results in conjunction with optical modeling.

The active layers showed similar UV-Vis absorption spectra when they were deposited on top of either PEDOT:PSS as in the conventional structure or ZnO as in the inverted structure. However, the results from optical modeling reveal that significant differences in optical distribution and exciton generation profiles between these two device architectures after the complete devices were fabricated by putting on the top electrodes. For the best device in the conventional structure, the peak of the exciton generation profile within the BHJ is located in the middle of the vertical direction of the film. While in the inverted structure, the peak of the exciton generation profile is located closer to the top anode. As a result, the majority of electrons in the inverted cell need to travel longer distance to reach the bottom cathode. Therefore, improvement of electron mobility in the BHJ is required to achieve optimized performance for inverted cells. This can be achieved by increasing the fullerene to polymer blend ratio from 3:1 to 4:1, which resulted in a factor of 3 increase in electron mobility measured by electron only devices.

To further improve the efficiency of the inverted cells, we have modified the interface between the PEDOT:PSS hole-transporting layer and the Ag anode with a thin layer of graphene oxide (GO). The use of a GO modifier improves the electron-blocking property of the anode, which is supported by the decreased dark current under reverse bias. A high PCE of 6.38% was achieved, which is even higher than that of the optimal conventional device.

(a)

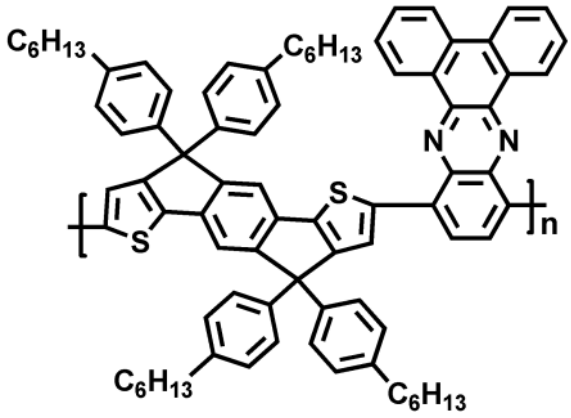

PIDT-PhanQ

(b)

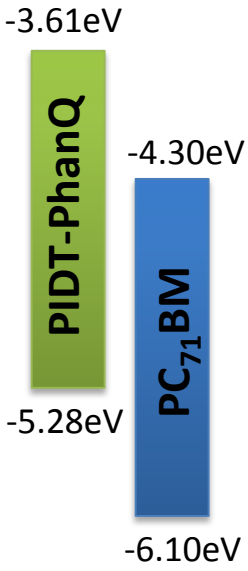

Figure 4-1 (a) The molecular structure of PIDT-PhanQ. (b) Energy level diagram of PIDT-PhanQ and PC71BM.

4.2 EXPERIMENTAL

4.2.1 *Device fabrication*

PSCs were fabricated using ITO-coated glass substrates (15 Ω sq^{-1}.), which were cleaned with detergent, de-ionized water, acetone, and isopropyl alcohol. In the conventional structure devices, a thin layer (ca. 35 nm) of PEDOT:PSS (Baytron® P VP AI 4083, filtered at 0.45 μm) was first spin-coated on the pre-cleaned ITO-coated glass substrates at 5,000 rpm and baked at 140°C for 10 min under ambient conditions. The substrates were then transferred into a nitrogen-filled glovebox. Subsequently, the polymer:$PC_{71}BM$ active layer (ca. 90 nm) was spin-coated on the PEDOT:PSS layer from a homogeneous solution. The solution was prepared by dissolving the polymer and fullerene at different weight ratios in o-dichlorobenzene overnight and filtered

through a PTFE filter (0.2 μm). The substrates were annealed at 110 °C for 10 min prior to electrode deposition. At the final stage, the substrates were pumped down to high vacuum (< 2 × 10^{-6} Torr), and calcium (30 nm) topped with aluminum (100 nm) was thermally evaporated onto the active layer. For inverted device fabrication, a thin layer of ZnO nanoparticles (ca. 30nm) synthesized using the method described by Beek *et al*.[150] was spin-coated onto the pre-cleaned ITO-coated glass substrates. The same process used for active layer in the conventional structure devices was also used for the inverted devices. After annealing, PEDOT:PSS (10nm)was spin-coated on top of BHJ film and annealed at 100 °C for 10 min. An Ag electrode (100nm) was then deposited to complete the inverted devices structure. Shadow masks were used to define the active area (10.08×10^{-2} cm^2) of the devices.

4.2.2 *Device characterization*

The current-voltage (I-V) characteristics of unencapsulated photovoltaic devices were measured under ambient conditions using a Keithley 2400 source-measurement unit. An Oriel xenon lamp (450 Watt) with an AM1.5 G filter was used as the solar simulator. The light intensity was set to 1 sun (100 mW cm^{-2}) using a calibrated Hamamatsu silicon diode with a KG5 color filter, which can be traced to the National Renewable Energy Laboratory (NREL). The EQE system uses a lock-in amplifier (Stanford Research Systems SR830) to record the short-circuit current under chopped monochromatic light.

Optical modeling by transfer matrix formalism

We assume the multilayer is embedded between two semi-infinite layers (j=0, j=m+1), which is glass and air in our case. The devices is composed of m individual layer, j (j=1,2, ……,

m) with thickness, d_j, and wavelength–dependent complex indices of refraction, $\bar{n}_j = n_j + i \cdot k_j$. We assume that the multilayer is illuminated from the direction x along the surface normal.

At an interface between layer j and k, the propagation of the optical field is described by the interface matrix I_{jk} .

$$\begin{bmatrix} E_j^+ \\ \bar{E}_j^- \end{bmatrix} = I_{jk} \begin{bmatrix} E_k^+ \\ \bar{E}_k^- \end{bmatrix} = \begin{bmatrix} \frac{1}{t_{jk}} & \frac{r_{jk}}{t_{jk}} \\ \frac{r_{jk}}{t_{jk}} & \frac{1}{t_{jk}} \end{bmatrix} \begin{bmatrix} E_k^+ \\ \bar{E}_k^- \end{bmatrix}$$

Where $\bar{E}_j^{\pm}$ and $\bar{E}_k^{\pm}$ are the components of the optical electric field propagation in the positive (+) and negative (-) direction in the adjacent layers j and k, respectively. For a plane wave propagation along the surface normal, the Fresnel complex reflection and transmission coefficients are $r_{jk} = (\bar{n}_j - \bar{n}_k)/\ (\bar{n}_j + \bar{n}_k)$ and $t_{jk} = 2\bar{n}_j/\ (\bar{n}_j + \bar{n}_k)$, respectively. The propagation through a layer j causes absorption and a phase shift, as described by the layer matrix L_j

$$L_j = \begin{bmatrix} e^{-i\xi_j d_j} & 0 \\ 0 & e^{i\xi_j d_j} \end{bmatrix},$$

where $\xi_j = \left(\frac{2\pi}{\lambda}\right)\bar{n}_j$. The electric field in the two outermost layers j=0 and j=m+1 are related via the transfer matrix S

$$\begin{bmatrix} \bar{E}_0^+ \\ \bar{E}_0^- \end{bmatrix} = S \begin{bmatrix} \bar{E}_{m+1}^+ \\ \bar{E}_{m+1}^- \end{bmatrix},$$

where

$$S = \begin{bmatrix} S_{11} & S_{12} \\ S_{21} & S_{22} \end{bmatrix} = \left(\prod_{n=1}^{m} I_{(n-1)n} L_n\right) \cdot I_{m(m+1)} .$$

The reflection and transmission coeffients are then $r = \frac{\bar{E}_0^-}{\bar{E}_0^+} = \frac{S_{22}}{S_{11}}$ and $t = \frac{\bar{E}_{m+1}^+}{\bar{E}_0^+} = S_{11}^{-1}$, respectively. The absorption efficiency of a multilayers stack is then $\eta_A = 1 - T - R$, with

$T = \frac{|t|^2 \bar{n}_{m+1}}{\bar{n}_0}$ and R= $|r|^2$, then transmissivity and reflectivity, respectively, of the multilayer structure. The device is typically supported by a substrate with a thickness of 0.1-1mm >>λ. Hence, the effect of the substrate is included by correcting T and R for reflections at the air/substrate and substrate/multilayer interfaces rather than by including it directly in the transfer matrix calculation, viz.

$R' = \frac{R^* + R}{1 + R^* R}$,

$T' = \frac{T^* T}{1 + R^* R}$,

with

$R^* = \left|\frac{1 - \bar{n}_0}{1 + \bar{n}_0}\right|^2$,

$R^* = \left|\frac{2}{1 + \bar{n}_0}\right|^2$,

where $\bar{n}_0$ is the refraction index of the substrate. The absorption efficiency is then $\eta_A = 1 - T' - R'$. To obtain the electric field within layer j, we note that the total multilayer transfer matrix is

$S = S_j^- L_j S_j^+$,

with

$S_j^- = (\prod_{n=1}^{j-1} I_{(n-1)n} L_n) \cdot I_{j(j-1)j}$,

$S_j^+ = (\prod_{n=j+1}^{m} I_{(n-1)n} L_n) \cdot I_{m(m+1)}$.

The electric field propagating in the positive direction in the layer j at the left interface is related to the incident plane wave by

$\frac{\bar{E}_j^+}{\bar{E}_0^+} = t_j^+ = \frac{\frac{1}{S_{j11}^-}}{1 + \frac{S_{j12}^- S_{j21}^+}{S_{j11}^- S_{j11}^+} e^{i2\xi_j d_j}}$.

The total electric field at an arbitrary position inside layer j is given in terms of the electric field of the incident wave by

$$E_j(x) = E_j^+(x) + E_j^-(x) = (t_j^+ e^{i\xi_j x} + t_j^- e^{-i\xi_j x})E_0^+$$

The time averaged absorbed power as a function of position is then

$$Q_j(x) = \frac{4\pi c\varepsilon_0 k_j n_j}{2\lambda} \left|\vec{E}_j(x)\right|^2 ,$$

where c is the speed of light and ε_0 is the permittivity of free space.

Thus, the exciton generation rate can be calculated by $G_j(x) = \left(\frac{\lambda}{hc}\right) Q_j(x)$.

This $G_j(x)$ is wavelength dependent, and by integrate $G_j(x)$ on all the spectrum where the materials have absorption, the spatial distribution of exciton generation as a function of position in the active layer can be plot out.[32][33]

4.2.3 *Mobility measurements*

Space charge limited currents have been tested in electron-only devices with a configuration of ITO/Al/polymer:PCBM/Ca/Al and hole-only devices with a configuration of ITO/PEDOT:PSS/polymer:PCBM/Pd. The devices were prepared following the same procedure described in experimental section for photovoltaic devices, except that the metal electrode was replaced by palladium (50 nm). The dark current of the SCLC devices was measured under ambient by using an Agilent 4155B semiconductor parameter analyzer. The mobilities were determined by fitting the dark current to the model of a single carrier SCL current with field dependent mobility, which is described as

$$J = \frac{9}{8}\varepsilon_0\varepsilon_r\mu_0 \exp\left(0.891\gamma\sqrt{\frac{V}{L}}\right)\frac{V^2}{L^3}$$

where J is the current, μ0 is the zero-field mobility, γ is the field activation factor, ε0 is the permittivity of free space, εr is the relative permittivity of the material, V is the effective voltage, and L is the thickness of the active layer,. In simulation, εr was assumed to be 3 for hole-only devices and 4.5 for electron-only devices, which is a typical value for organic materials and fullerene. The effective voltage can be obtained by subtracting the built-in voltage (VBI) and the voltage drop (VRS) from the substrate's series resistance from the applied voltage (VAPPL), V=VAPPL-VBI-VRS. VBI values of 0 V and 0.5 V were used for electron-only and hole-only devices, respectively, which provided best fits to the log(J) – log(V) curves. The series resistance to our substrates was determined from the reference device without the active layer, i.e. a device configuration of ITO/Al/Ca/Al and ITO/PEDOT:PSS/Pd , and was found to be ca. 3.84 Ω for electron-only devices and 20.38 Ω for hole-only devices. BHJ films with variable thickness have been applied and the thickness of the film (L) was measured by using atomic force microscopy. The film thickness is controlled by spin speed, however, due to different blending ratio and substrate surface energy, the thickness are slightly different for each configuration.

4.3 Results and Discussion

Figure 4-2 The devices structure of conventional and inverted structure PSC. depicts the schematics of both the conventional and inverted structure devices. The conventional structure devices use the PEDOT:PSS coated ITO to collect holes and calcium/aluminum cathode to collect electrons, while the inverted devices use ZnO nanoparticles (ZnO NP) film as the electron-transporting/-selecting layer and PEDOT:PSS as the hole-transporting layer. The distribution of optical density in the active layer showed marked differences between these two

device architectures. This causes exciton dissociation profile to shift and strongly affects the device performance.

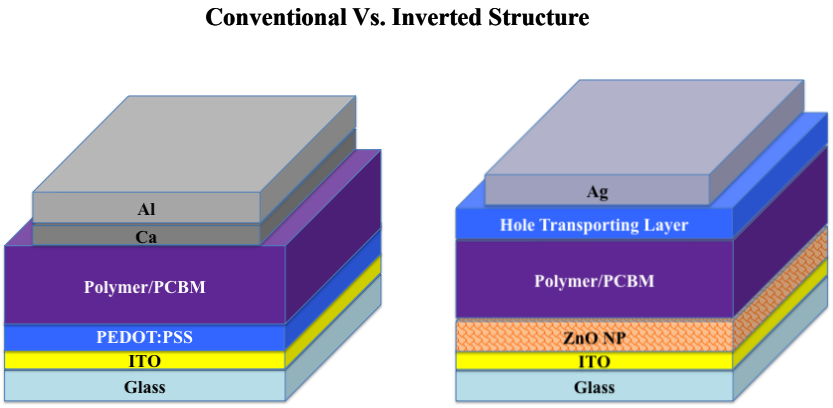

Figure 4-2 The devices structure of conventional and inverted structure PSC.

4.3.1 *Devices Characteristics*

Composition change of the polymer/$PC_{71}BM$ blend affects the efficiency of light harvesting as well as the balance of charge transfer in the devices. To achieve optimal performance of

PIDT-PhanQ/$PC_{71}BM$ based PSCs, a series of conventional and inverted structure devices with different blending ratios were fabricated. Thickness of the active layer was optimized based on the result of the best performance devices derived from previous round of study. The J-V characteristics of these devices are shown in Figure 4-3 (a) and (b) and their performance are listed in Table 4-1 and Table 4-2. The detailed fabrication procedures are described in the experimental section.

All photoactive layers in the fabricated devices are ~ 90-100 nm in thickness. Similar V_{oc}s were observed for all the conventional structure devices, even when the polymer/fullerene ratio was varied from 1:2 to 1:5 in the BHJ layer. However, both J_{sc} and FF of the devices increase when the blending ratio was changed from 1:2 to 1:3. When it was further increased to 1:5, the J_{sc} and FF of the devices started to decrease. The devices with the 1:3 blending ratio exhibit the best performance, with J_{sc} of 11.2 mA cm^{-2} and fill factor (FF) of 64%.[99] When similar processing condition and blending ratio of the BHJ films were used in the inverted structure devices, a relatively large decrease of PCE from 6.24% to 4.91% was observed. Both J_{sc} and FF in the inverted devices are lower, especially the FF dropped from 64% to 55%. To achieve better PCE, a systematic tuning of the blending ratio in the BHJ film was performed. The best device performance was obtained when the fullerene content was increased to 80%, which resulted in devices with J_{sc} of 11.0 mA cm^{-2}, FF of 64%, and PCE of up to 5.97%. Further increase of the fullerene ratio gave negative effect on both J_{sc} and FF, which led toward a decreased PCE.

To compare the device characteristics of PSCs prepared under the same processing condition of the BHJ films in different structures, external quantum efficiencies (EQE) of

devices with 1:3 and 1:4 polymer/fullerene blending ratios in both conventional and inverted structures were measured (Figure 4-4). The data showed that for inverted device with a 1:3 blending ratio, its EQE was lower than that of the conventional cell over most of the absorption spectrum, which resulted in lower J_{sc} values. While for the one with the 1:4 blending ratio, its EQE was similar to, or slightly higher than that of the conventional cells.

Compared to the EQE spectra of the BHJ films with 1:3 and 1:4 polymer/fullerene blending ratios, the films with 1:3 ratio showed higher EQE in the range between 600 and 700 nm, while the films with a 1:4 ratio gained higher EQE in the ranges of 500-600nm and 350-400nm. Figure 4-5 (a) shows the absorption spectra of PIDT-PhanQ:$PC_{71}BM$ BHJ films with different blend compositions on top of the PEDOT or ZnO-coated glass substrates and Figure 4b shows the extinction coefficient (*k*) of both pure PIDT-PhanQ and $PC_{71}BM$ films obtained from spectroscopic ellipsometry. According to Figure 4-5, it can be easily explained that films with higher polymer content exhibit higher EQE in the range between 600 and 700 nm due to enhanced contribution from the polymer absorption, while higher $PC_{71}BM$ content in the 1:4 ratio film provides stronger absorption in the ranges between 500-600 nm and 350-400 nm.

Table 4-1Performance of convention structure devices with different PIDT-PhanQ/$PC_{71}BM$ blending ratios

Conventional Structure	Ratio	V_{oc} [V]	J_{sc} [mA cm^{-2}]	FF	PCE [%]	J_{max} [mA cm^{-2}]	J_{sc} / J_{max}
	1:2	0.87	9.81	0.58	4.98		
	1:2.5	0.87	10.2	0.62	5.50		
	1:3	0.87	11.2	0.64	6.24	13.0	86%
	1:4	0.84	10.4	0.61	5.41	12.6	83%
	1:5	0.84	9.01	0.59	4.46		

Table 4-2Performance of inverted structure devices with different PIDT-PhanQ/PC71BM blending ratios

Inverted Structure	Ratio	V_{oc} [V]	J_{sc} [mA cm^{-2}]	FF	PCE (%)	J_{max} [mA cm^{-2}]	J_{sc} / J_{max}
	1:3	0.87	10.4	0.55	4.91	16.5	63%
	1:4	0.86	11.0	0.63	5.97	15.6	71%
	1:5	0.86	10.9	0.58	5.44		

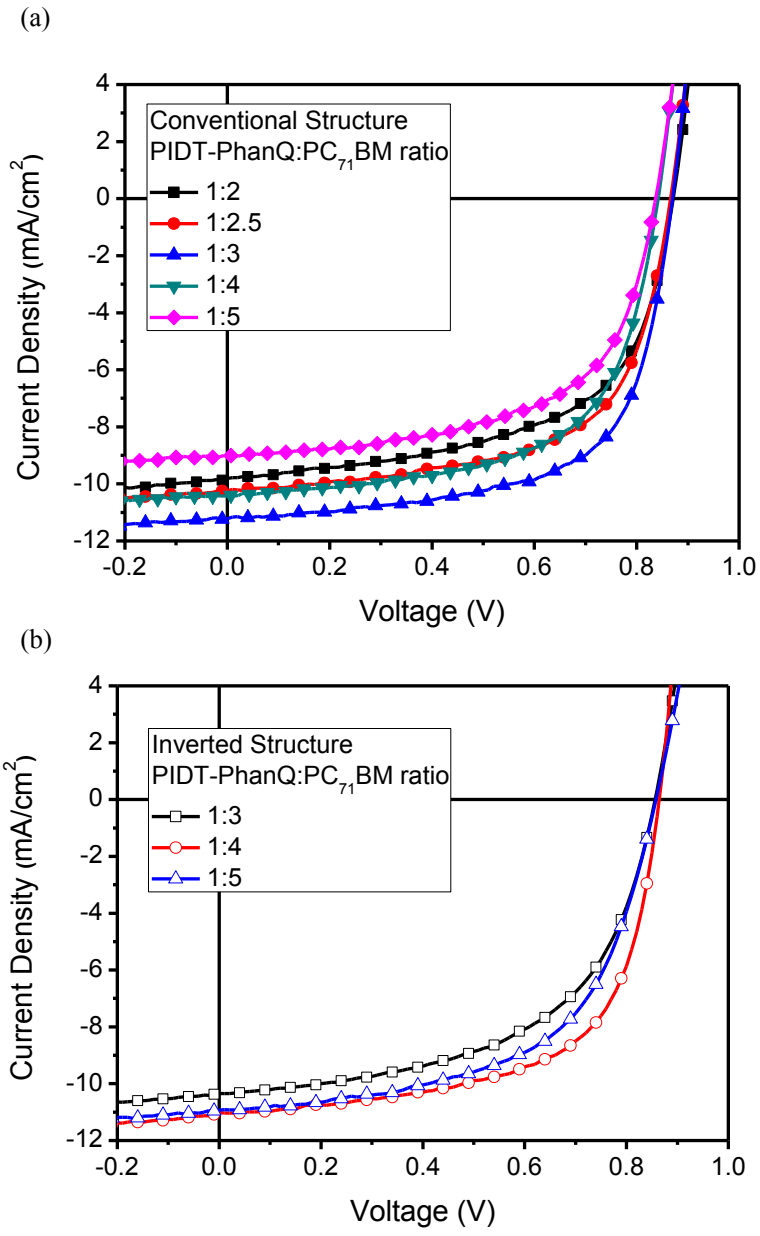

Figure 4-3 J-V characteristics of (a) conventional structure and (b) inverted structure of PSCs based on PIDT-PhanQ:PC_{71}BM with different blending ratio.

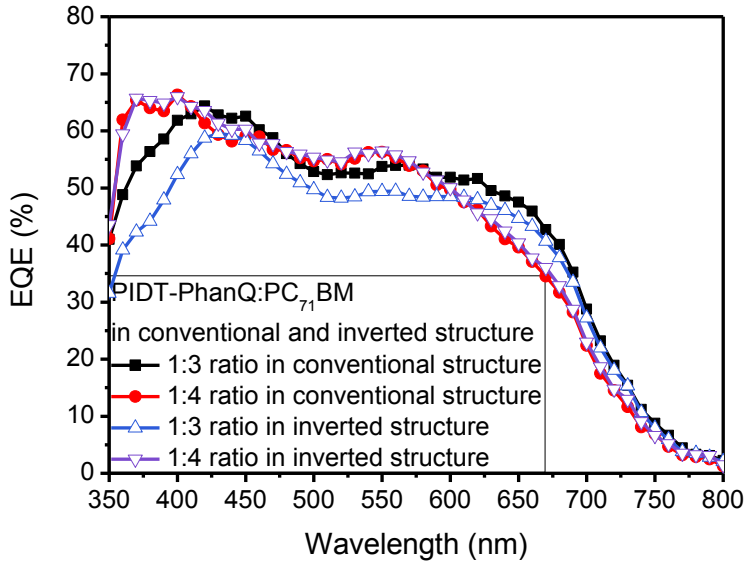

Figure 4-4 External quantum efficiency of devices based on conventional and inverted structure with PIDT-PhanQ: $PC_{71}BM$ blending ratio 1:3 and 1:4.

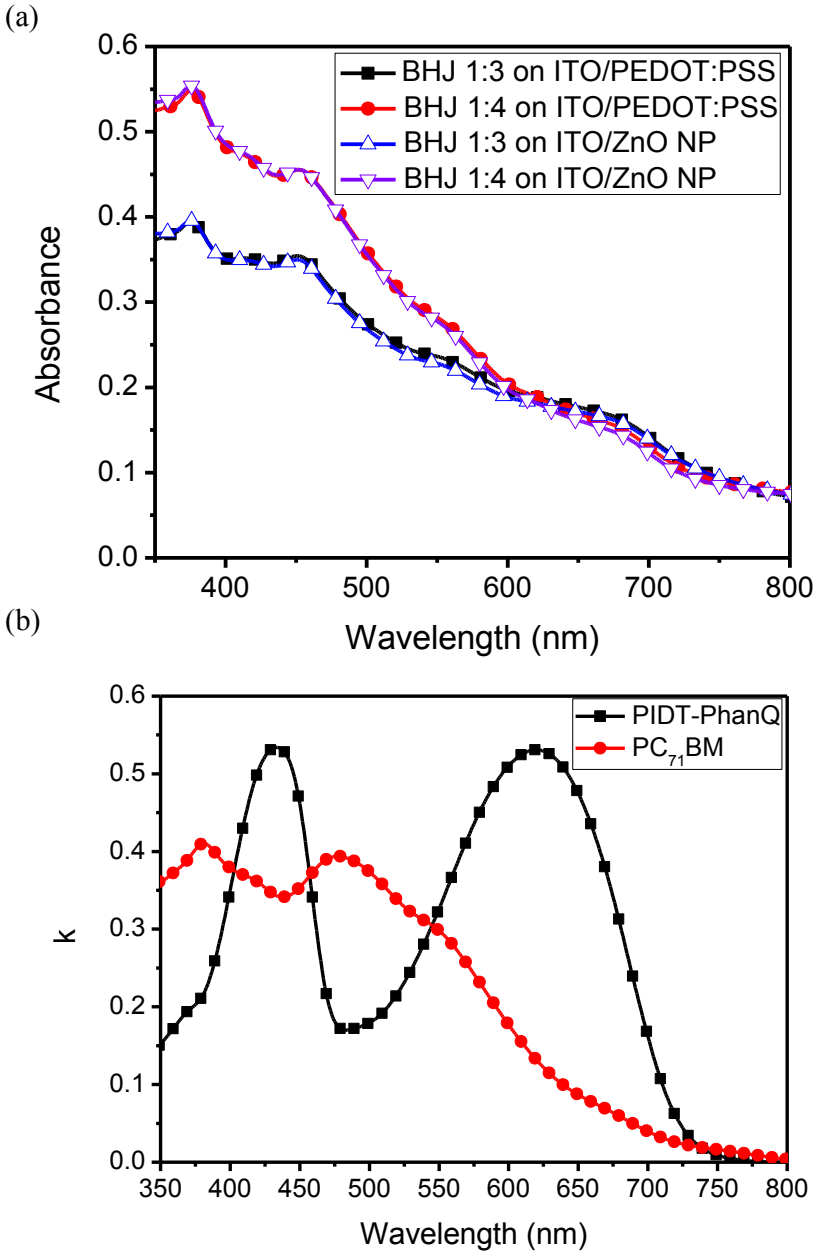

Figure 4-5 (a) direct absorption spectrum of PIDT-PhanQ:$PC_{71}BM$ BHJ films with different content and substrates (reference on PEDOT/ITO and ZnO/ITO respectively (b)Extinction coefficient k for PIDT-PhanQ and PC71BM.

4.3.2 *Optical modeling characteristics*

Since EQE could be affected by several factors, such as rate of photon absorption in the active layer, exciton generation, and charge separation, transport, and collection, to understand the difference of EQE in various device structures with the same composition, one must compare photon absorption in the device active layers. Similar UV-Vis absorption spectra were found when the same composition of the BHJ films were deposited on PEDOT:PSS for the conventional structure and on ZnO for the inverted structure Figure 4-5.

However, the fraction of incident light intensity absorbed by the films is influenced by all layers in the device due to the interference effect, therefore, the independently measured absorption of BHJ films can not be counted on to represent the absorption of films in devices. To determine the individual contribution of the active layer on optical absorption, proper optical modeling is needed.[151] In this work, transfer matrix formalism is used to calculate the interference of reflected and transmitted light waves at each interface in the stack based on the wavelength-dependent complex index of refraction (n+ik) of each material.[32], [39-40] The imaginary part of the complex index of refraction (k) could be measured directly by UV-Vis spectrometry and the real part (n) could be measured by variable angle spectroscopic ellipsometry for each layer (Figure 4-6a).

Based on the n and k values for each layer, the fraction of light absorbed by the BHJ films in both conventional and inverted device structures are calculated and summarized in Figure 4-6(b). Due to the difference of layer sequence and the optical properties of ZnO NP, PEDOT: PSS, and metals, the BHJ films showed dramatically different intensities of absorption fraction within the conventional and inverted device structures despite having the same content and similar extinction coefficients. In general, the fractions of absorbed light in BHJ films of the inverted devices are greater when the active layer was kept with the same thickness. Although

the optical constant is spatially dependent, the BHJ layer is treated as a homogenous film and its diffuse scattering is ignored in this optical modeling.

To facilitate the calculation of the maximum attainable photocurrents (J_{max}), 100% internal quantum efficiency (IQE) was assumed for all wavelengths. However, due to potential loss in charge recombination, transport, and collection, it is almost impossible to achieve 100% IQE, therefore, the experimental value of J_{sc} is always lower than that of the J_{max}. The calculated J_{max} values and ratio between J_{sc} and J_{max} are summarized in Table 1. For the conventional structure device with the 1:3 blending ratio, the calculated J_{max} value is 13.0 mA cm^{-2}, while the experimental J_{sc} value is 11.0 mA cm^{-2}, which indicates that ~ 86% of the generated excitons have been converted into charges and harvested by the electrodes.

However, in the same BHJ film of the inverted devices, only 63% of the generated excitons contributed to the photocurrents. By increasing the fullerene content to 80% in the conventional structure, the J_{sc}/J_{max} ratio decreased slightly from 86% to 83%, while it increased from 63% to 71% in the inverted structure. Generally, the same thickness films with a 1:4 ratio generated fewer excitons than the 1:3 ratio films. The increased J_{sc}/J_{max} ratio in the inverted structure demonstrates that higher fullerene content is favored for better charge separation, transport, and collection.

To understand the necessity for higher fullerene content in the inverted structure devices, the spatial distribution of exciton generation in BHJ films was also calculated. As it shown in Figure 4-7, the generated excitons is broadly distributed within the BHJ film of the conventional device with its peak approximately in the center, while the excitons is concentrated mainly in the region which is 40-80 nm away from the electron-transporting layer in the inverted device with its peak located near the top of the BHJ film.

In the latter case, most of the generated excitons are closer to the anode. Therefore, most of the generated electrons need to travel longer distance in order to be collected by the cathode. This increases the probability of charge recombination during their transport. The result of this modeling is consistent with the lower FF observed for inverted devices with 1:3 blending ratio. It also provides the explanation for higher fullerene ratio required in the inverted devices because it may provide a better-connected electron-transporting path in the device to decrease possible bimolecular recombination.

To prove that higher fullerene ratio can aid in electron transport and collection, both hole-only devices with the configuration of ITO/PEDOT:PSS/BHJ/Pd and electron-only devices with the configuration of ITO/Al/BHJ/Ca/Al were fabricated. Figure 4-8 shows the log scale *J-V* characteristics in the dark for devices with the blending ratios of 1:3 and 1:4. Higher electron mobility has been observed for the devices with 1:4 blending ratio, while hole mobility for the devices with 1:3 blending ratio is higher. The *J-V* curves were fitted with the space-charge-limited-current (SCLC) model to calculate both mobilities. The electron and hole mobility in the 1:3 ratio BHJ film is 3.68×10^{-5} $cm^2V^{-1}s^{-1}$ and 2.17×10^{-3} $cm^2V^{-1}s^{-1}$, respectively. The electron mobility in the 1:4 ratio BHJ films is 1.06×10^{-4} $cm^2V^{-1}s^{-1}$, which is about 3 times that of the 1:3 ratio BHJ film; while the hole mobility decreases to 1.00×10^{-3} $cm^2 V^{-1}s^{-1}$. Increasing the fullerene ratio significantly improves the electron mobility. Although it also slightly decreased the hole mobility, it is still much higher than the electron mobility. Due to the exciton generation peak shifting to anode in inverted structure, the electron mobility is more critical to prevent recombination loss. The mobility data shows that electron transportation is more efficient in films with higher fullerene content. Mobility measurements based on the SCLC calculations are described in the supporting information.

Furthermore, the mobilities of hole and electron also have been investigated by fabrication the BHJ films with different blending ration into field-effect transistors, using a bottom-gate, top contact configuration. The BHJ film is spin coated on Divinylsiloxane-bis-benzocyclobutene-treated SiO_2, and Au is used as the top metal electrode. The transfer characteristics are shown in Figure 4-9 and the electron and hole mobilities are extracted in the saturation regime from the linear fit of $(I_{ds})^{1/2}$ vs V_{gs}. Electron mobility in 1:3 ratio BHJ is 4.4×10^{-4} $cm^2V^{-1}s^{-1}$, and in 1:4 ratio BHJ is 1.5×10^{-3} $cm^2V^{-1}s^{-1}$, while hole mobility in 1:3 ratio BHJ is 3.2×10^{-3} $cm^2V^{-1}s^{-1}$, and in 1:4 ratio BHJ is 1.8×10^{-3} $cm^2V^{-1}s^{-1}$. The data also shows the electron mobility in 1:4 blending ratio BHJ is 3.4 times that of the 1:3 ratio BHJ film, while the hole mobility in 1:3 blending ratio BHJ is about 1.8 times that of the 1:4 ratio BHJ film. Also, even with decreased hole mobility in 1:4 ratio BHJ film, the hole mobility is still higher than electron mobility.

These data support the hypothesis that electrons are more efficiently transported in films with higher fullerene contents.

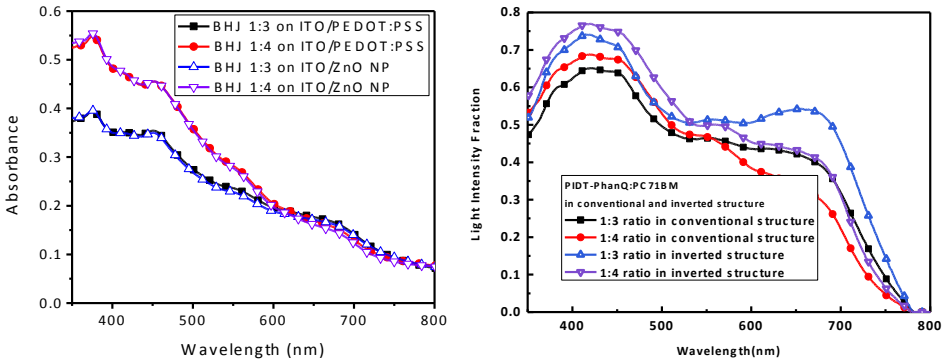

Figure 4-6 (a) complex index of refraction's real part n and imaginary part k, and (b) calculated light intensity absorption fraction by the transfer matrix optical model of PIDT-PhanQ:PC71BM films with 1:3 and 1:4 blending ratio in conventional and inverted structure.

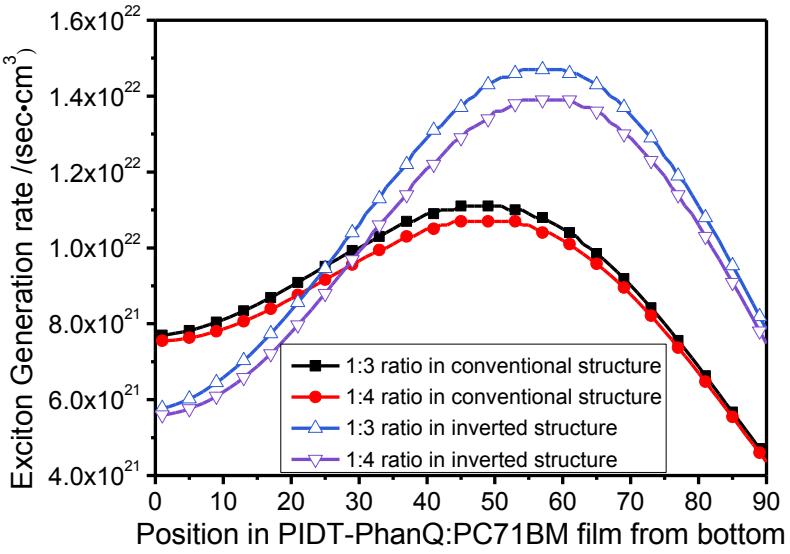

Figure 4-7 Calculated distribution profile of exciton generation rate in PIDT-PhanQ:PC71BM film in PSCs with 1:3 and 1:4 blending ratio in conventional and inverted structure.

(a)

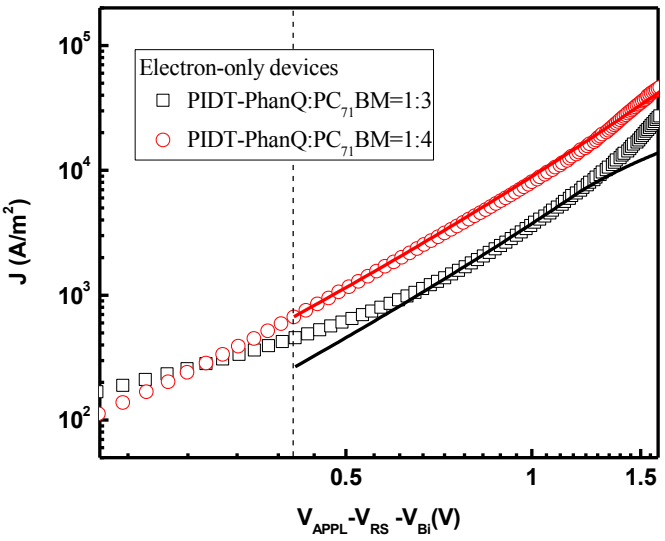

(b)

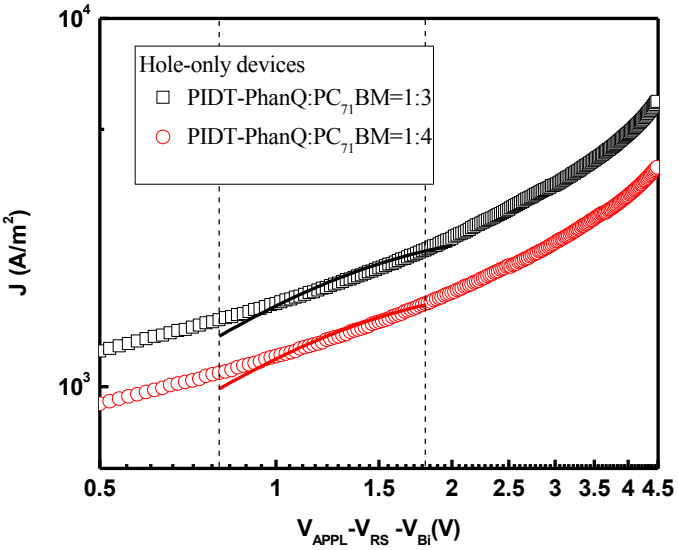

Figure 4-8 Measured J-V characteristics under dark for (a) electron-only and (b) hole-only devices consisting of PIDT-PhanQ/$PC_{71}BM$ BHJ films. The bias is corrected for built-in Voltage $V_{Bi,}$ arising from difference in the work function of the contacts

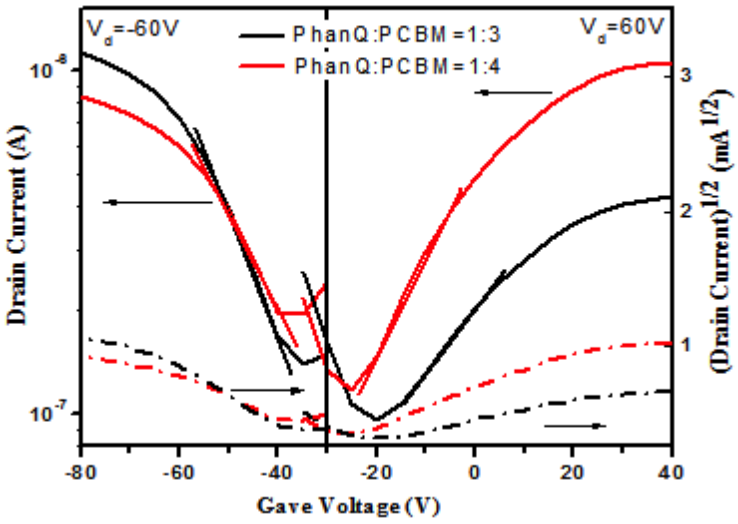

Figure 4-9 Transfer characteristics of the FET devices for BHJ with 1:3 and 1:4 blending ratio

4.3.3 *Modification of the Hole-Transporting Layer*

When PEDOT:PSS was used as hole-transporting layer in the 1:4 blending ratio inverted devices, PCE as high as 5.97% could be achieved. Recently, we have found that GO can function as a good anode interfacial layer to improve the performance of inverted cells.[152][153] To evaluate whether GO can be used to further improve the performance of inverted devices, hole-transporting layer based on individual PEDOT:PSS, GO, or their bilayer combination has been investigated. The *J-V* characteristics of inverted cells comprise of different interfacial layers under illumination and in the dark, and their EQE data, are shown in Figure 4-10. The devices performance are summaries in Table 4-3The devices utilizing a combined PEDOT:PSS (ca. 10nm)/GO (ca. 2-3nm) as hole-transporting layer show the best performance with J_{sc} of 11.6 mA cm^{-2} and PCE of up to 6.38%, which are comparable to those of the best conventional structure devices. The devices with GO as the interfacial layer show higher series resistance in both under illumination and in the dark. However, they also give a lower leakage current in the dark under the reverse bias compared to PEDOT:PSS.

It is well known that PEDOT:PSS can not efficiently block electrons and it sometimes can even function as cathode in PSCs to collect electrons.[154] By inserting a layer of GO, the electron-blocking property of the anode buffer layer can be enhanced. After combining PEDOT:PSS and GO, a better electron-blocking effect was achieved for device under reverse bias without sacrificing its low series resistance.

Table 4-3 Device performance of inverted structure PSCs with different hole-transporting layers.

Hole Transporting Layer	V_{oc} [V]	J_{sc} [mA cm^{-2}]	FF	R_s [Ω•cm^2]	R_p [Ω•cm^2]	PCE [%]
PEDOT:PSS	0.86	11.0	0.63	2.09	672	5.97
GO	0.86	10.9	0.62	2.87	672	5.88
PEDOT:PSS/GO	0.86	11.6	0.64	2.03	672	6.38

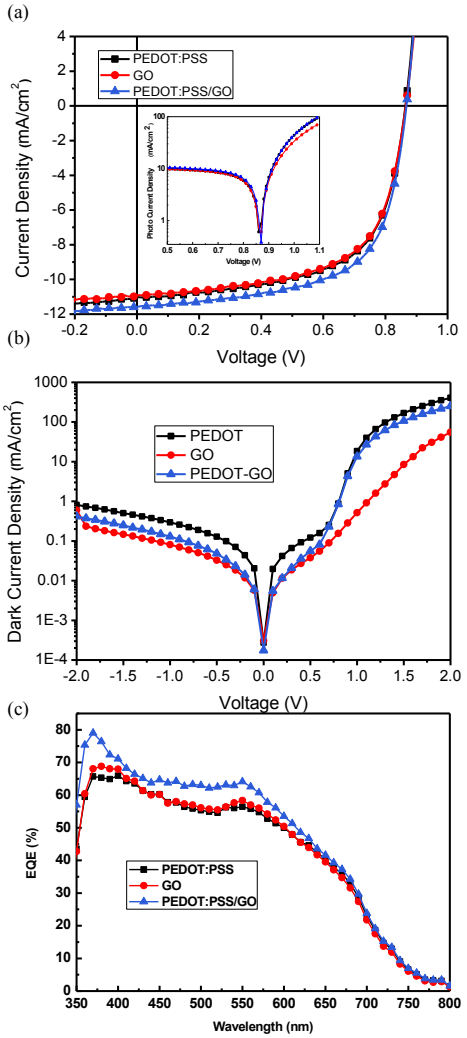

Figure 4-10 J-V characteristic of devices (a) under illumination and (b) in the dark. (c) external quantum efficiency of devices with different hole transporting top layer.

4.4 CONCLUSIONS

In summary, high-performance inverted device based on PIDT-PhanQ/$PC_{71}BM$ have been demonstrated. The effects of device geometry on exciton harvesting and overall performance were investigated by using BHJ films processed under the same condition. Higher fullerene blending ratios are needed in the inverted devices to achieve optimal PCEs. Optical modeling using transfer matrix formalism has been utilized to explain the variations of performance in different device architectures. Different processing sequence and optical properties of buffer layers are shown to be responsible for the significant difference observed in optical field distribution and exciton generation profile throughout the devices. The shifted exciton generation peak position in inverted devices necessitates the higher ratio of fullerene in the BHJ film to maintain adequate electron mobility. By utilizing a hole-transporting layer comprised of PEDOT:PSS and GO, inverted structure PSCs with very high PCE of 6.38% has been demonstrated.

Chapter 5. HIGH EFFICIENCY BILAYER PROCESSED DEVICE IN INVERTED STRUCTURE BASED ON A LOW-BAND GAP POLYMER

5.1 INTRODUCTION

As a promising technology for renewable energy, polymer solar cells (PSCs) have attracted substantial interests due to the potential to be a low cost alternative to conventional photovoltaic technologies.[1][5][64][155]–[158] Over the past few years, enormous progress has been made on the performance of PSCs with power conversion efficiency (PCE) of 9-10% being demonstrated owning to the development of new light harvesting and interface materials, also the optimization of these materials in new device architectures. [131][132]

The most efficient PSCs are typically composed of a layer of polymer donor and fullerene acceptor bulk-heterojunction (BHJ) film. An interpenetrating network with nanoscale phase separation between the donor and the acceptor phases should be formed in order to increase the number of interfaces for efficient exciton dissociation and to provide an effective pathway for charge transport and collection.[159][160] However, achieving the favorable nano-scale phase separation morphology of the BHJ is not trivial and typically requires tremendous efforts on optimizing the blend composition and processing conditions. Other parameters such as the difference in surface energies between the polymer and fullerene,[161] the solubility limits of the materials,[162] the tendency of crystallization of fullerenes[163] and the different wetting properties on different substrates[164]will also affect the BHJ morphology, making it one of most challenging problem to solve in OPV research.[9][22][30][113][165]–[168]

In contrast, bilayer planar heterojunction, formed by sequentially depositing donor and acceptor layers, is conceptually more straightforward. The first bilayer heterojunction solar cell

was reported by Tang in 1986 with 1% PCE,[10] but it was considered not as promising as BHJ on the basis of the argument that the smaller interfacial area between donor and acceptor limits exciton dissociation, due to the short exciton diffusion length in organic materials. However, one advantage of a bilayer structure is the improved charge transport by having better continuity of charge transporting phases in vertical direction. Once charge separation occurs at the bilayer interface, the charges will have an unobstructed path to their respective electrodes.

Recently, Ayzner et.al. have reignited interest by showing that an all-solution processed bilayer structure PSC based on poly(3-hexylthiophene) (P3HT) : [6,6]-phenyl-C_{61} butyric acid methyl ester (PCBM) could perform comparably to a BHJ device,[169] and several groups have since reported efficient bilayer heterojunction systems.[168][170]–[174] With appropriate choice of processing solvent system and post thermal treatment, mixing can occur between polymer and fullerene in the bilayer structure, resulting in a layer-evolved BHJ that can generate a sufficient interface for exciton dissociation. Without the concern on the spontaneously formed phase-separation of the donor/acceptor blend during the spin coating process, bilayer structure also simplifies the processing by eliminating the need for complex solvent systems such as the use of additives, or using complicated post-treatments such as solvent vapor annealing. Additionally, the polymer and fullerene layers can be controlled and optimized independently, to better fulfill balanced optical and electrical properties.

With the rapid development of new polymer donors, especially low-band gap polymers with extended absorption, there is substantial room for further improvement of bilayer devices. However, other than P3HT, poly[N-9″-heptadecanyl-2,7-carbazole-*alt*-5,5-(4′,7′-di-2-thienyl-2′,1′,3′-benzothiadiazole) (PCDTBT) is the only polymer system that has been applied to solution-processed bilayer devices, and proved that it can perform on par with BHJ-based

devices.[171]

The challenge to apply a bilayer structure to newly developed polymer systems with solution processing comes from sequentially solution deposition of polymer and fullerene layers. To spin-coat fullerene on top of a polymer layer, an appropriate orthogonal solvent combination is critical, which needs to provide good film formation for each material, and ensure the upper fullerene layer deposition will not destroy the bottom polymer film. After deposition, inter-diffusion can be driven by thermal annealing. Another potential limitation of the bilayer device is its applicability to the more stable inverted device architecture, which requires the reversion of the bilayer sequence with polymer layer on top of the fullerene layer to ensure adequate charge collections.

In this paper, a newly developed polymer PCPDT-FBT, with enhanced absorption at longer wavelengths, increased V_{oc} and enhanced π-π stacking from fluorine substitution,[108] has been successfully processed with bilayer deposition. With the optimization of the deposition conditions and post-thermal treatment, the bilayer devices show comparable PCE to their corresponding BHJ devices. Furthermore, highly efficient inverted devices are also first demonstrated despite starting with a bilayer with intuitively unfavorable sequence. The bilayer inverted device even shows a higher performance compares to its BHJ counterpart with an increase in J_{sc} of 16.4 mA/cm^2 and a PCE of 5.84%. External quantum efficiencies (EQE) of bilayer and BHJ films in both conventional and inverted structures have been compared. To further understand the differences between bilayer and BHJ structures, absorbed fraction of incident light intensity for each active layer has been calculated by optical modeling, and IQE is obtained. An improved IQE has been observed for an inverted bilayer structure. In order to understand the factors that may contribute to the improved IQE, efficient photoluminescence

(PL) quenching has been shown as an evident of good mixture of polymer and fullerene in bilayer films. Furthermore, the XPS in combination with ellipsometry analysis were utilized to determine the relative distribution of PCPDT-FBT and $PC_{71}BM$ throughout the active layer and revealed that PCPDT-FBT and $PC_{71}BM$ are homogenously distributed in the vertical direction within the bilayer structure, similar to that of BHJ films. The surfaces of all the blended films are found to be enriched with a thin layer (3-5nm) of PCPDT-FBT, which is favorable for hole collection in inverted structure. Electron and hole mobilities of pristine PCPDT-FBT film, bilayer film and BHJ film have been calculated from SCLC measurement. The improved electron transport in the vertical direction after depositing $PC_{71}BM$ on top of PCPDT-FBT proves the good penetration of fullerene into the polymer film. At the same time, the bilayer film shows greater electron mobility than that of the BHJ film, and has a more balanced charge transport. Also, improved polymer chain stacking of PCPDT-FBT in bilayer films has been observed from UV-Vis absorption compared to BHJ films. The better electron mobility and polymer chain stacking can contribute to the high efficiency of inverted bilayer device.

5.2 EXPERIMENTAL

5.2.1 *Bilayer film process*

Figure 5-1 shows the molecular structures of PCPDT-FBT, and Schematic diagrams of the device structures utilized in this study are shown in

Figure 5-1(b). The details of devices fabrication are described in the experimental section. The most critical step for bilayer processing is to find an appropriate orthogonal solvent combination. PCPDT-FBT can be dissolved in *o*-dichlorobenzene (DCB), chlorobenzene (CB)

and *o*-xylene, with solubility from high to low, and the absorption spectra normalized at 722 nm for both solution and thin film are shown in **Figure 2(a)**. All of the absorption spectra show a peak at 722nm, which is attributed to the intramolecular charge transfer (ICT) band between the cyclopenta-dithiophene (CPDT) and benzothiadiazole (BT) units.[68][115] In DCB solution, a shoulder peak appears at ~770 nm. By changing the solvent from DCB to CB, and *o*-xylene, the intensity of the shoulder peak increased with maximum absorption at 776nm. This peak is believed to be the result of π-π stacking, and the increasing absorption indicates stronger packing and decreased solubility in CB and *o*-xylene. By processing the solution into films, the π-π stacking peak becomes even stronger with an absorption onset shift up to 860nm. This π-π stacking peak was also observed in *o*-xylene solution at room temperature, however, when the solution was heated up to 90°C, the peak at 776 nm decreased dramatically, indicating the lost of packing and increase in solubility in hot solution (**Figure 2(b)**).

Utilizing the solubility difference in different solvents and temperatures, the bilayer active layer film is fabricated in the following procedure: PCPDT-FBT is first dissolved in *o*-xylene at 90°C and spin coated from the hot solution; $PC_{71}BM$ is dissolved in a co-solvent of o-xylene:DCB with 4:1 ratio by volume, and then spin-coated directly on top of PCPDT-FBT bottom layer at room temperature. The schematic processing steps are shown in **Figure 3**. The PCPDT-FBT film processed from *o*-xylene has a rough surface (with surface roughness of RMS=13.37nm) with a large surface area (as shown in **Figure 3(b)**), which can provide a large interface between polymer and fullerene. With $PC_{71}BM$ processed from a combination of *o*-xylene（at room temperature) as a poor solvent and DCB as a good solvent for PCPDT-FBT, a good penetration of $PC_{71}BM$ into the PCPDT-FBT film can be achieved via solvent-induced polymer swelling followed by diffusion of fullerene into the polymer matrix. [171][175]–[177]

Thermal annealing will further improve the inter-mixture of fullerene and polymer.[170][174][178] The AFM topography after $PC_{71}BM$ deposition has also been shown in **Figure 3(c)** with a reduced surface roughness RMS of 2.09 nm.

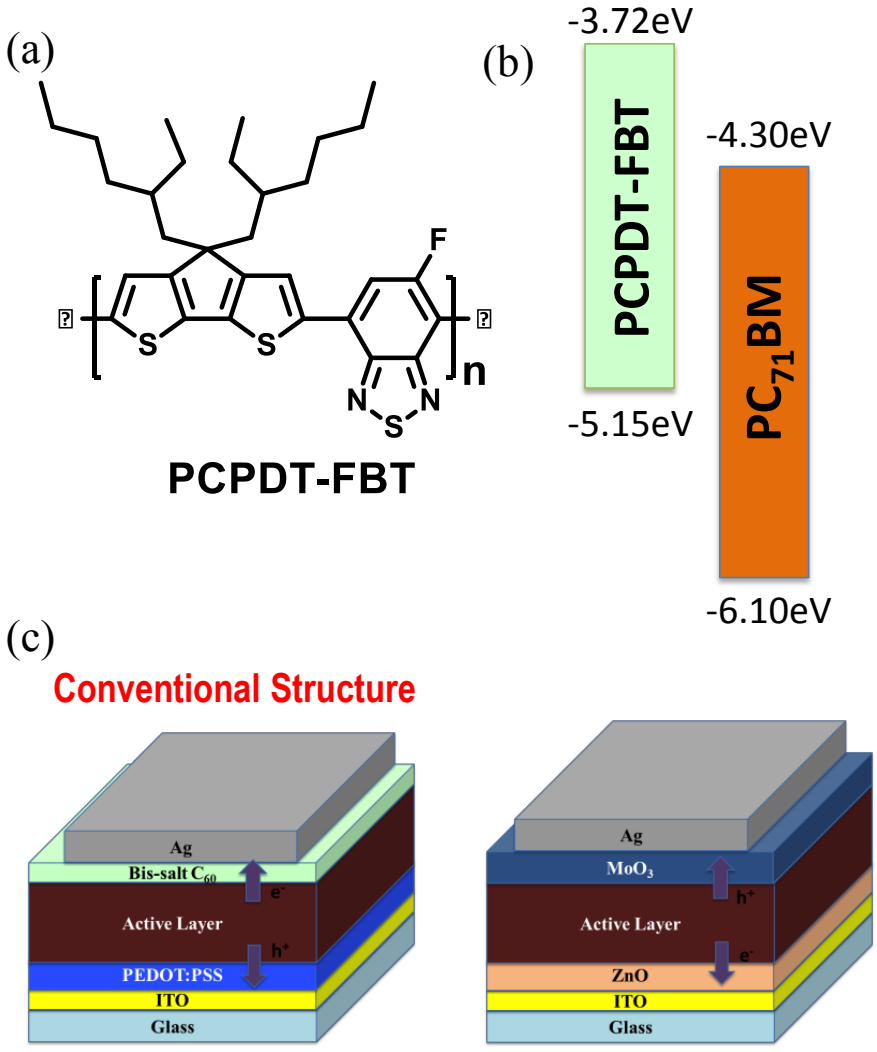

Figure 5-1(a) The molecular structure of PCPDT-FBT. (b) Energy level diagram of PCPDT-FBT and $PC_{71}BM$. (c) The devices structure of conventional and inverted structure PSC.

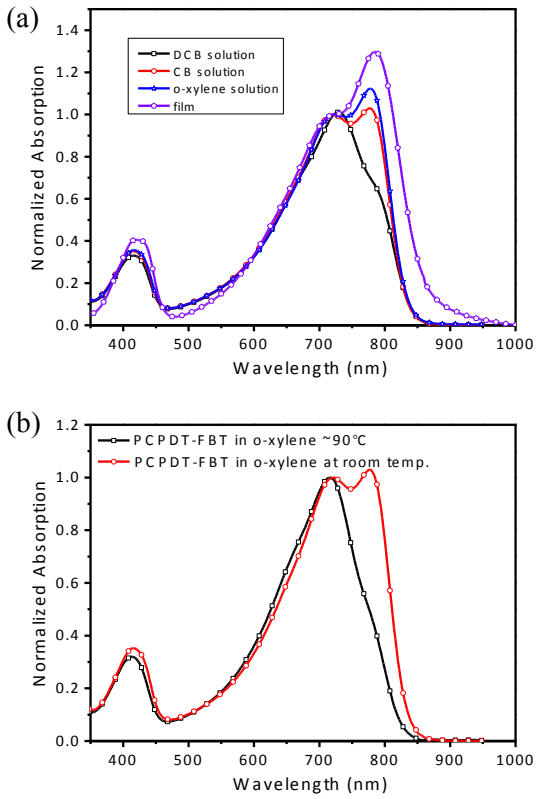

Figure 5-2 The normalized UV-Vis spectra of PCPDTFBT (a) in solution and thin film, (b)in o-xylene with different temperature.

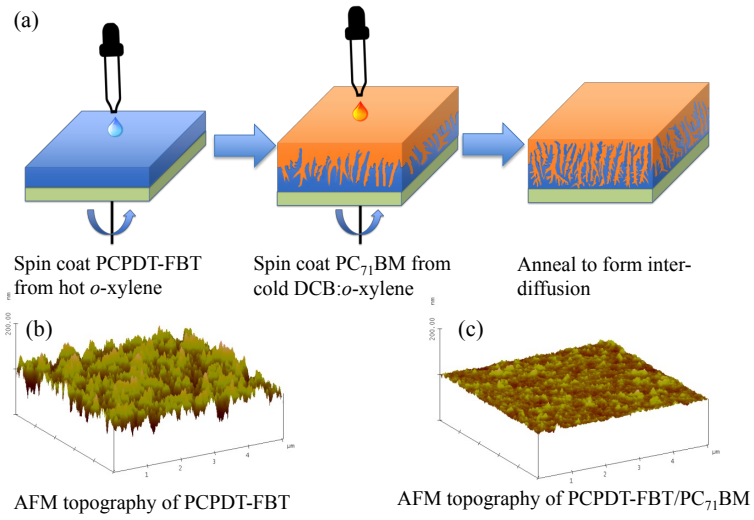

Figure 5-3 (a) The schematic of bilayer processing steps and (b)corresponding 3D AFM topography of PCPDT-FBT and PCPDT-FBT/PC71BM.

5.2.2 *Fabrication of photovoltaic devices*

PSCs were fabricated using ITO-coated glass substrates (15 Ω sq^{-1}.), which were cleaned with detergent, de-ionized water, acetone, and isopropyl alcohol. After drying, the substrates were air-plasma treated for 20 seconds to remove any residual organic materials. The solution for the BHJ was prepared by dissolving the polymer and fullerene at weight ratios of 1:3 in chlorobenzene to a total concentration of 12mg mL^{-1} at 110°C overnight and filtered through a PTFE filter (0.45 μm). For bilayer devices, a PCPDT-FBT solution was prepared by dissolving the polymer in o-xylene to a concentration of 6mg/mL and stirring overnight at 110°C; a $PC_{71}BM$ solution was made by dissolving $PC_{71}BM$ powder in a co-solvent of o-dichlorobenzene and o-xylene with volume ratio of 1:4 to a concentration of 16mg/mL at room temperature. In the conventional structure devices, a thin layer (ca.35 nm) of PEDOT:PSS (Baytron® P VP AI 4083, filtered at 0.45 μm) was first spin-coated on the pre-cleaned ITO-coated glass substrates at 5,000 rpm and baked at 140°C for 10 min under ambient conditions. The substrates were then transferred into a nitrogen-filled glovebox. Subsequently, the active layer was then deposited on the PEDOT:PSS. The BHJ active layer was spin coated from the PCPDT-FBT:$PC_{71}BM$ mixture at 900 rpm. For the bilayer devices, PCPDT-FBT was cast from a solution kept at 90°C, and a solution of $PC_{71}BM$ at room temperature was spin coated onto the polymer films. All of the substrates were then placed on the hot plate at 110°C for 30min. After annealing, substrates were briefly transferred out of the glovebox (total ambient exposure <10 min) and a 10 nm thick film of C_{60}-bis surfactant (1 mg/mL in methanol) was spin-coated at 5k rpm. The substrates were then transferred back into the glovebox and annealed at 110 °C for 5 min to drive off any remaining solvent prior to metal deposition. At the final stage, the substrates were pumped down to high vacuum (< 2×10^{-6} Torr), and silver (100 nm) was thermally evaporated onto the active layer.

For inverted device fabrication, ZnO precursor prepared using the method described by Sun *et al*. [149] was spin-coated onto the pre-cleaned ITO-coated glass substrates, and films were annealed at 200°C for 1 hour in air. Before BHJ film processing, a fullerene self-assembled monolayer (C_{60}-SAM) in in tetrahydofuran (THF) chlorobenzene (CB) (1:1 *v/v)* was spin coated on the ZnO film for surface modification.[44] The same process used for the active layer in the conventional structure devices was also used for the inverted devices. After annealing, MoO_x (5 nm) topped with silver (100 nm) was thermally evaporated onto the active layer to complete the inverted devices structure. Shadow masks were used to define the active area (10.08×10^{-2} cm^2) of the devices.

SCLC devices were prepared following the same procedure described for photovoltaic devices, except that the metal electrode was replaced by palladium (50 nm). The dark current of the SCLC devices was measured under ambient by using an Agilent 4155B semiconductor parameter analyzer.

5.2.3 *Other Samples preparation*

XPS samples were prepared the same way as photovoltaic devices up to active layer deposition. Photoluminescence and UV-Vis absorption samples were prepared on glass substrates, and the active layers were deposited the same way as in device fabrication.

5.2.4 *Device characterization*

The current-voltage (I-V) characteristics of unencapsulated photovoltaic devices were measured under ambient conditions using a Keithley 2400 source-measurement unit. An Oriel xenon lamp (450 Watt) with an AM1.5 G filter was used as the solar simulator. The light intensity was set to 1 sun (100 mW cm^{-2}) using a calibrated Hamamatsu silicon diode with a KG5 color filter, which can be traced to the National Renewable Energy Laboratory (NREL).

The EQE system uses a lock-in amplifier (Stanford Research Systems SR830) to record the short-circuit current under chopped monochromatic light.

XPS depth profiling analysis was performed on a PHI 5000 Versa Probe (Ulvac-Phi. Inc) using a monochromated Al K-α X-ray source and a hemispherical analyzer. An Ar ion gun was used for sputtering experiments at an ionization energy of 1 kV. The beam was defocused to cover over 10mm^2 sample area. Atomic compositions were determined from surface spectra, and were calculated by determining the integral peak intensities using a Shirley type background, removing the inelastically scattered electron contribution.

Variable angle spectroscopic ellipsometry measurements were carried out using a Woollam Co. M-2000 Variable Angle Spectroscopic Ellipsometer, with a spectral range 210-1700nm. All measurements were done for angles between 45 and 75 degrees with 5 degree steps. Software of CompleteEASE provided by J.A. Woollam Co., Inc was used for fitting and data analysis.

Space charge limited currents have been tested in electron-only devices with a configuration of ITO/Al/polymer:PCBM/Ca/Al and hole-only devices with a configuration of ITO/PEDOT:PSS/polymer:PCBM/Pd. The devices were prepared following the same procedure described in experimental section for photovoltaic devices, except that the metal electrode was replaced by palladium (50 nm). The dark current of the SCLC devices was measured under ambient by using an Agilent 4155B semiconductor parameter analyzer. The mobilities were determined by fitting the dark current to the model of a single carrier SCL current with field dependent mobility, which is described as

$$J = \frac{9}{8}\varepsilon_0\varepsilon_r\mu_0 \exp\left(0.891\gamma\sqrt{\frac{V}{L}}\right)\frac{V^2}{L^3}$$

where J is the current, μ_0 is the zero-field mobility, γ is the field activation factor, ε_0 is the permittivity of free space, ε_r is the relative permittivity of the material, V is the effective voltage, and L is the thickness of the active layer,. In simulation, ε_r was assumed to be 3 for hole-only devices and 4.5 for electron-only devices, which is a typical value for organic materials and fullerene. The effective voltage can be obtained by subtracting the built-in voltage (V_{BI}) and the voltage drop (V_{RS}) from the substrate's series resistance from the applied voltage (V_{APPL}), $V=V_{APPL}-V_{BI}-V_{RS}$. V_{BI} values of 0 V and 0.5 V were used for electron-only and hole-only devices, respectively, which provided best fits to the log(*J*) – log(V) curves. The series resistance to our substrates was determined from the reference device without the active layer, i.e. a device configuration of ITO/Al/Ca/Al and ITO/PEDOT:PSS/Pd , and was found to be ca. 3.84 Ω for electron-only devices and 20.38 Ω for hole-only devices. Active layer films with variable thickness have been applied and the thickness of the film (L) was measured by using atomic force microscopy, which are 85nm for pristine PCPDT-FBT film, 110nm for bilayer film, and 80nm for BHJ.

5.3 Results and Discussion

5.3.1 *Bilayer Devices perform as good as bulk-heterojunction devices*

5.3.1.1 Devices Characteristics

Optimized device performance of BHJ and bilayer devices in both conventional and inverted structures are summarized in In the conventional structure, the bilayer device proves to have a similar efficiency as BHJ for exciton generation, charge separation, transport, and collection. Inverted structure devices have a better IQE on all wavelength range than conventional structure devices, and the bilayer inverted device shows to be the best one in

electronic processes. The result indicates that the bilayer films have a sufficient interface between polymer and fullerene for efficient exciton dissociation. Also, it demonstrates that the bilayer film in an inverted structure provides better charge transport and collection.

Table 5-1, and the J-V data is shown in Figure 5-4. Bilayer devices show performances comparable to BHJ devices, both in the conventional and inverted structures. The bilayer devices have a short-circuit current density (J_{sc}) of 14.4 mA cm^{-2} in the conventional structure, and 16.4 mA cm^{-2} in an inverted structure. The BHJ devices show similar J_{sc}s of ~15mA cm^{-2} in both conventional and inverted structures. Due to the limited exciton diffusion length of organic materials, only excitons generated within ~10-20 nm from the interface between donor and acceptor would contribute to photocurrent generation. The high J_{sc}s in the bilayer structure indicates a good penetration of $PC_{71}BM$ into polymer film with nano-scale phase separation. The V_{oc}s for the BHJ devices are 0.74-0.75 V, which are slightly higher than that of bilayer devices (0.73V in conventional structure and 0.71V in inverted structure). This may be due to the difference in polymer:fullerene ratio in these optimized devices,[179] which will be analyzed later. FFs of bilayer devices in both structures are higher than their corresponding BHJ devices. Bilayer films are believed to naturally have better continuity of charge transporting phases in vertical direction, and the higher FFs may be contributed by better charge transport in bilayer films, which will be discussed later based on SCLC result. Surprisingly, even the bilayer films start with a layout of polymer film at bottom and fullerene film at top , which is not expected to form favorable vertical phase separation in an inverted structure, the final device of the inverted bilayer structure shows better photovoltaic performance.

To further compare bilayer and BHJ devices, external quantum efficiency (EQE) is measured and shown in Figure 5-5. In a conventional structure, BHJ and bilayer devices show similar EQE spectra. Inverted structure devices generally have higher EQE than conventional ones, and the bilayer device have a further enhanced EQE on the fullerene absorption region compared to BHJ devices in an inverted structure. This is consistence with the increased J_{sc}s in inverted devices, especially in inverted bilayer devices.

The difference in the EQE spectra can be attributed to either a difference in absorption or internal quantum efficiency (IQE), since

$$\eta_{EQE} = \eta_{abs} \times \eta_{IQE},$$

where η_{abs} is the fraction of incident light intensity absorbed by active layer.

To compare the absorption difference in bilayer and BHJ films, direct UV-Vis absorption has been measured for active layer films on substrate of ITO/PEDOT as in convention structure, or ITO/ZnO as in inverted structure, and shown in Figure 5-6. All of the devices are optimized to achieve best PCE, and the UV-Vis absorption shows that they have different thicknesses and polymer: fullerene contents. In BHJ films, the ratio of polymer to fullerene will change the absorption, morphology and charge mobility at the same time, thus the optimized condition will be a balance between nanoscale phase separation and bi-continuous network formation, and also try to capture the maximum amount of photons. In bilayer films, the PCPDT-FBT and $PC_{71}BM$ layers can be controlled and optimized independently, to better balance their optical and electrical properties. Since devices in each structure are optimized separately, due to the different electric field distribution and interface modification, the optimized thickness for the conventional structure is ~90 nm, while for the inverted structure, it is ~110 nm. All of these can contribute to

the differences of active layers' absorption.

Films utilized in inverted structure show enhanced absorption, from both BHJ and bilayer devices. However, the fraction of incident light intensity absorbed by the films is influenced by all the layers in the device due to the optical interference effect. Therefore, the independently measured absorbance of BHJ films cannot be counted on to represent the absorption of the active layers in devices. To determine the individual contribution of the active layer on optical absorption, proper optical modeling is needed.[151] Here, transfer matrix formalism is used to calculate the interference of reflected and transmitted light waves at each interface in the stack based on the wavelength-dependent complex index of refraction (<n>+i<k>) of each material.[32][33][59] The imaginary part of the complex index of refraction <k> could be measured directly by UV-Vis spectrometry and the real part <n> is measured by variable angle spectroscopic ellipsometry (VASE) for each layer (shown in Figure 5-7). Based on the *n* and *k* values for each layer, the fraction of light absorbed by the BHJ films in both conventional and inverted device structures are calculated and summarized in Figure 5-8. The fractions of incident light absorbed by different active layers are quite different from the measured UV-Vis absorption spectra. The main difference of the absorbed fraction between bilayer films and BHJ films is in the 600-860 nm region, where bilayer films have a lower absorption fraction. Thus, we conclude that the higher EQE generated by the inverted structure, especially in the bilayer inverted device, is not a result of better absorption.

IQE, the ratio of charges extracted from a device to the number of photons absorbed by the active layer, provides a useful way to isolate electronic loss mechanisms from light coupling and parasitic absorption losses in devices.[180] IQE is calculated from the measured EQE spectrum and the absorption fraction obtained from optical modeling, and is shown in Figure 5-9. In the

conventional structure, the bilayer device proves to have a similar efficiency as BHJ for exciton generation, charge separation, transport, and collection. Inverted structure devices have a better IQE on all wavelength range than conventional structure devices, and the bilayer inverted device shows to be the best one in electronic processes. The result indicates that the bilayer films have a sufficient interface between polymer and fullerene for efficient exciton dissociation. Also, it demonstrates that the bilayer film in an inverted structure provides better charge transport and collection.

Table 5-1Performance of BHJ and bilayer devices in conventional and inverted structure devices based on PCPDT-FBT and PC71BM.

Structure	Active Layer	V_{oc} [V]	J_{sc} [mA cm^{-2}]	FF	PCE [%]
Conventional	BHJ	0.75	15.0	0.49	5.57
Conventional	Bilayer	0.73	14.4	0.52	5.51
Inverted	BHJ	0.74	15.5	0.47	5.35
Inverted	Bilayer	0.71	16.4	0.50	5.84

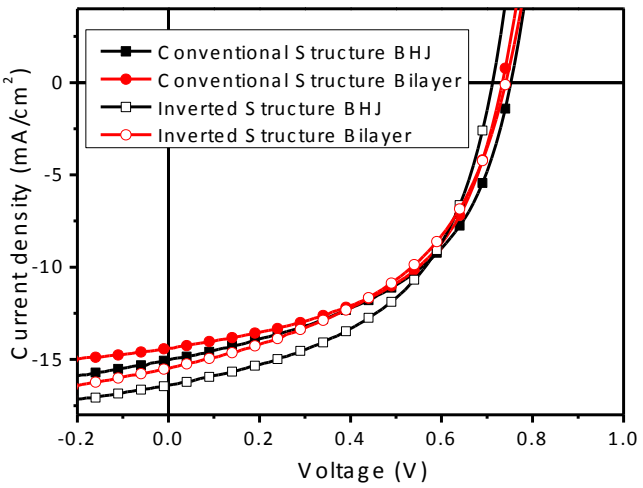

Figure 5-4 J-V characteristics of BHJ and bilayer films in conventional and inverted structure devices based on PCPDT-FBT and PC71BM.

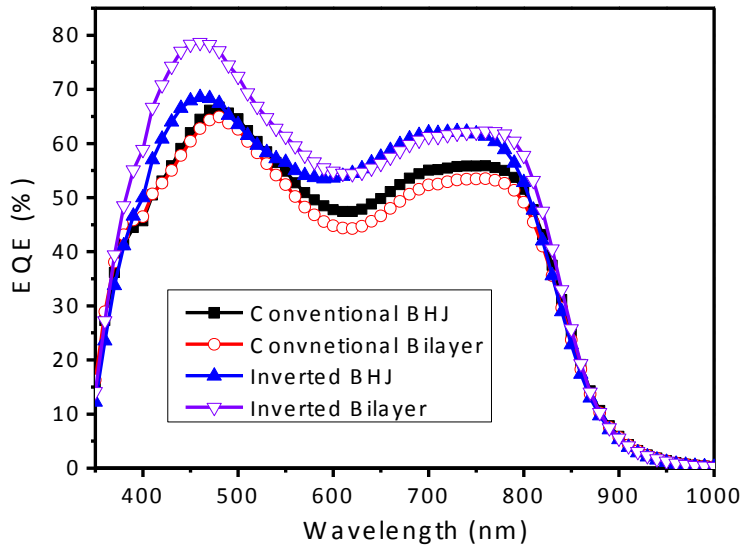

Figure 5-5 External quantum efficiency of BHJ and bilayer films in conventional and inverted structure devices based on PCPDT-FBT and PC71BM.

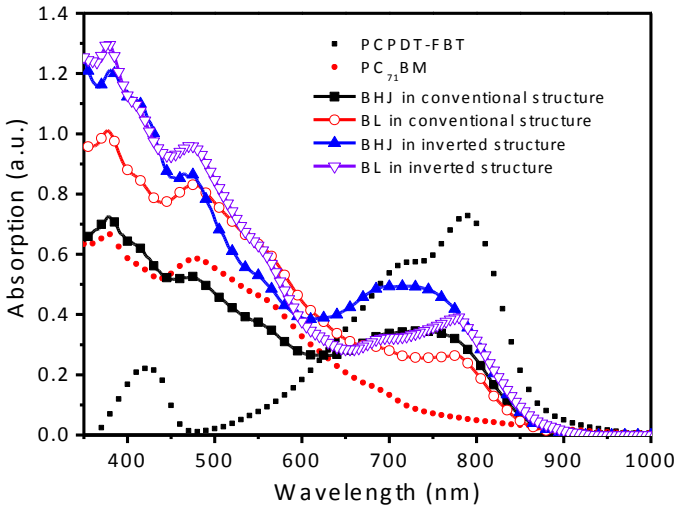

Figure 5-6 Direct absorption spectrum of BHJ and bilayer films in conventional and inverted structure devices based on PCPDT-FBT and PC71BM, together with the pristine PCPDT-FBT film and PC71BM film.

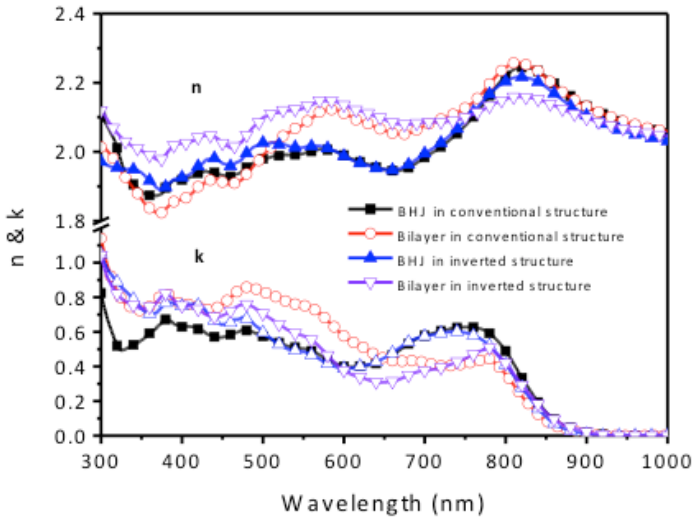

Figure 5-7 Complex index of refraction's real part n and imaginary part k of BHJ and bilayer films in conventional and inverted structure devices based on PCPDT-FBT and $PC_{71}BM$.

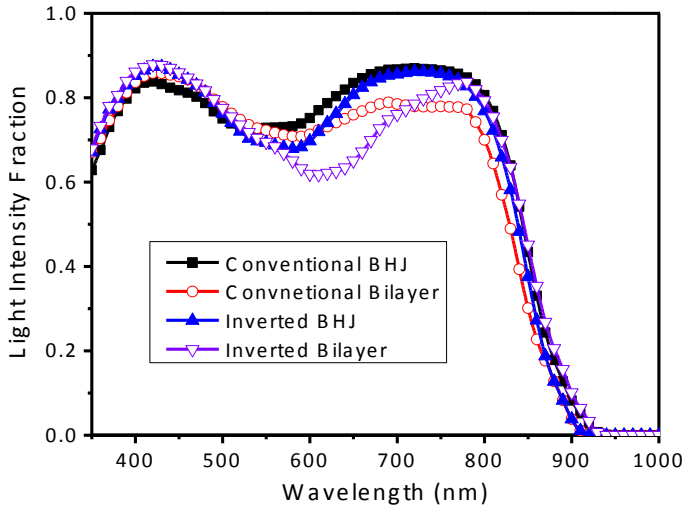

Figure 5-8 Calculated light intensity absorption fraction by the transfer matrix optical model of BHJ and bilayer films in conventional and inverted structure devices based on PCPDT-FBT and PC71BM.

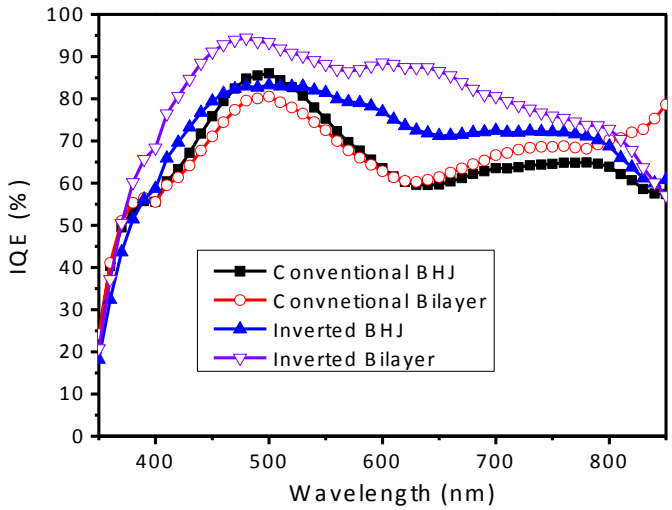

Figure 5-9 Internal quantum efficiency of BHJ and bilayer films in conventional and inverted structure devices based on PCPDT-FBT and PC71BM.

5.3.2 *Bilayer films show good donor/acceptor interdiffusion*

5.3.2.1 PL measurement

In order to prove a good mixture of $PC_{71}BM$ with PCPDT-FBT in the bilayer structure, the photoluminescence (PL) quenching properties of the PCPDT-FBT in PCPDT-FBT/$PC_{71}BM$ bilayer sample was measured, and compared to the BHJ samples. The PL quenching efficiencies of active layers (QE_{active}) were calculated using the equation:

$$QE_{active} = \frac{PL_{polymer} - PL_{active}}{PL_{polymer}} \times 100\% \quad (1)$$

where $PL_{polymer}$ is the PL intensity for the equivalent amount of PCPDT-FBT in the active layer without the presence of $PC_{71}BM$ and the PL_{active} is the measured PL intensity of the bilayer or BHJ films.[172] Noted that, during the deposition of the $PC_{71}BM$ from DCB/*o*-xylene co-solvents, part of the PCPDT-FBT film will be dissolved and removed, thus the amount of polymer in the bilayer film will be different from the original deposited polymer film. The absorption (as shown in Figure 5-10(a)) at 790 nm of each film is used to quantify the content of PCPDT-FBT in both the BHJ and bilayer films, where PCPDT-FBT has a strong absorption peak and $PC_{71}BM$ does not absorb light. By comparing the absorption at 790nm of the pristine PCPDT-FBT film of known thickness with BHJ and bilayer films, and testing the same PCPDT-FBT film's PL intensity, the PL intensity of an equivalent amount of the polymer in these two active layers are calculated. The PCPDT-FBT film has a strong emission band at 850nm. After depositing $PC_{71}BM$, the quenching efficiency of the bilayer film is 98.0%. As a control, in the BHJ film, 96.3% of PCPDT-FBT PL is quenched (as shown in Figure 5-10 (b)). The quenching efficiency of the bilayer film is comparable to the BHJ film, which indicates that a substantial amount of $PC_{71}BM$ is diffused into the polymer layer, allowing for very efficient exciton

quenching.

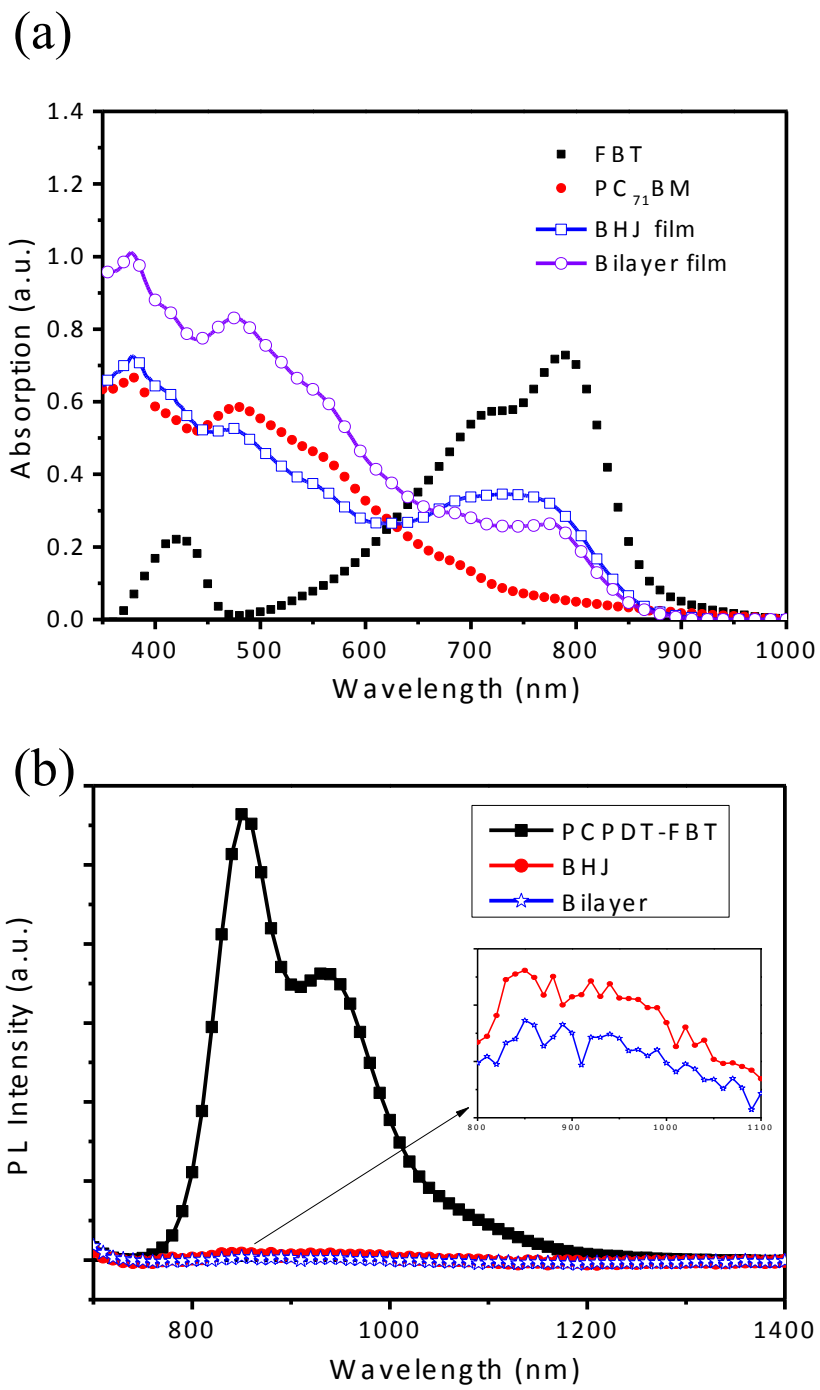

Figure 5-10 (a) UV-Vis and (b) photoluminescence of pristine PCPDT-FBT, BHJ and bilayer films.

5.3.2.2 XPS depth profile

The depth profile of composition variation in active layer films were probed by analyzing surface chemical composition with XPS, and using Ar^+ sputtering of the films to achieve depth resolution. Monochromatized Al K-Alpha X-ray were used during the scans, therefore sampling depth is limited to top 5 nm for each scan. After each scan, Ar^+ sputtering is used to remove top surfaces of the films, sub-surfaces were exposed and further analyzed by XPS. Scannings and sputterings were cycled until complete removal of the films, thus depth profiles of chemical compositions were obtained. The PCPDT-FBT to $PC_{71}BM$ weight ratio is calculated from the S/C atomic ratios. To calibrate the sputtering rate and to estimate the damage in the sample upon sputtering, 85nm of PCPDT-FBT film on ITO was tested and the S/C signal ratio was determined. A sputtering rate of 1.2nm min^{-1} was used, and the consistency in the PCPDT-FBT stoichiometry throughout the analysis with different depth indicates that in every scan, the signal comes from a surface without being affected by the sputtering process.[181] Thus the XPS data provides a reliable measurement of the sample composition as function of probing depth. When sputtering the active layers, the sputtering rate for PCPDT-FBT and $PC_{71}BM$ were assumed to be similar. The composition of PCPDT-FBT and $PC_{71}BM$ is calculated by measuring the content of carbon and sulfur, comparing the collected S/C signal from blending films to pristine PCPDT-FBT film, and considering the molecular formulas of PCPDT-FBT and $PC_{71}BM$. The vertical composition profiles of active layers are shown in Figure 5-11. The top surface of all blend films was found to be enriched with the polymer. The concentration reaches a constant value after the first 6 nm, and remains almost unchanged throughout the layers. This data clearly shows that the bilayer films generated from sequential deposition of the polymer and fullerene form vertically homogeneous films similar to that of BHJ film. In addition, , all the blended films are covered with a polymer-rich skin. This thin layer should be able to provide better hole collection

selectivity, thus will be favored for an inverted structure with holes collected by the top electrode. This phenomenon can be considered as a possible reason for higher IQE in an inverted structure.

Additionally, the BHJ films in both conventional and inverted structures have ~25% of PCPDT-FBT, which is consistent with the processing solution PCPDT-FBT:$PC_{71}BM$ ratio, as of 1:3. The bilayer film in an inverted structure has lower polymer content, and the bilayer film in the conventional structure shows the lowest PCPDT-FBT weight percentage, which are consistence with UV-Vis absorption. PCPDT-FBT in these two bilayer films are ~19% and ~12% of total film weight, respectively.

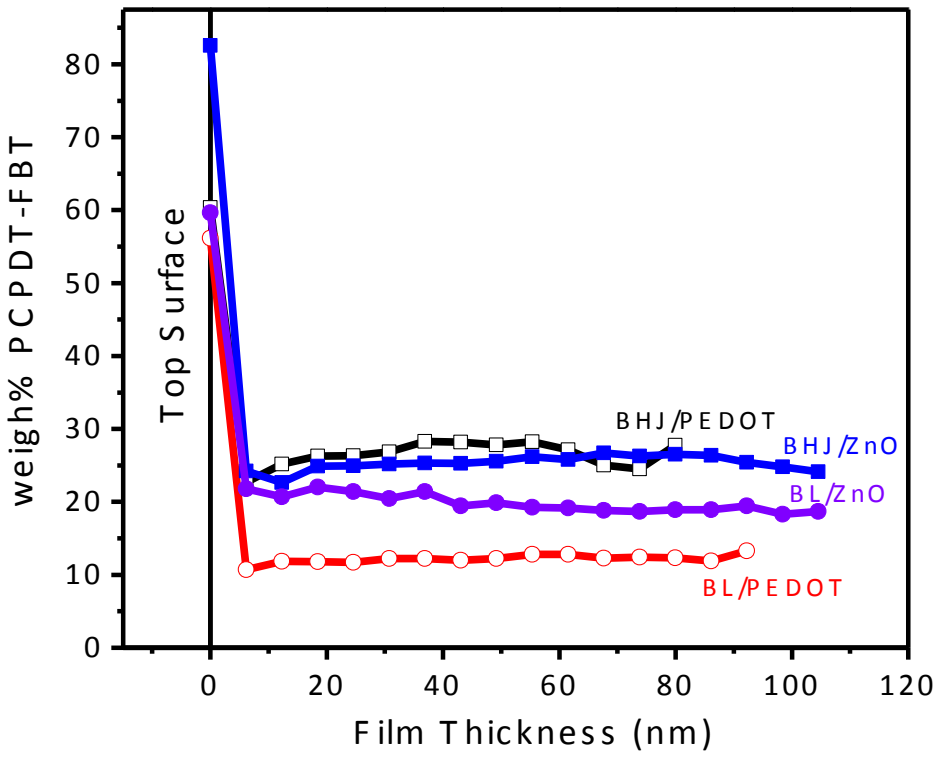

Figure 5-11 XPS depth profile of BHJ and bilayer films in conventional and inverted structure devices based on PCPDT-FBT and PC71BM.

5.3.2.3 Variable angle spectroscopic ellipsometry measurements

Further verification of the vertical composition profile is achieved through variable angle spectroscopic ellipsometry (VASE) measurements.[40][182] Effective medium approximation (EMA) ascribed to Bruggeman[183] is utilized to describe the mixtures of materials with known *n* and *k*. The EMA is a physical model that describes the macroscopic properties of a medium based on the properties and the relative fractions of its components. In the Bruggeman model, the effective dielectric function of the mixture is given by the equation:

$$0 = (1-f)\frac{\varepsilon_1 - \varepsilon}{\varepsilon_1 + 2\varepsilon} + f\frac{\varepsilon_2 - \varepsilon}{\varepsilon_1 + 2\varepsilon}$$

where $\langle\varepsilon\rangle$ is the effective dielectric function of the blending medium, ε_1 and ε_2 are the dielectric functions of the two media subject to mixing, and f is the volume ratio of material 2.

Dielectric function of PCPDT-FBT and $PC_{71}BM$ pristine films has been measured using VASE and shown in Figure 5-12. Uniaxial orientation of PCPDT-FBT is taken into account to obtain its dielectric function,[184] while the $PC_{71}BM$ is isotropic. The complex index of refraction ($\langle n\rangle+i\langle k\rangle$) for blending films have already been shown in Figure 5-12, and dielectric function $\langle\varepsilon\rangle = \langle\varepsilon_1\rangle+i\langle\varepsilon_2\rangle = (\langle n\rangle+i\langle k\rangle)^2$. A simple model of single layer EMA mix of the PCPDT-FBT/$PC_{71}BM$ layer is first proposed. "Root mean square errors" (MSEs) of the fitted data with experimental data ~6 are given for tested samples, showing a reasonably good fitting of this model with experimental data. By changing the model from simple EMA mix to linear gradient of polymer/fullerene in a vertical direction, concentration gradient slope of less than 0.01 as the fitting results in all films indicate a homogenous vertical distribution of polymer/fullerene.

Finally, a model of EMA mix of the PCPDT-FBT/$PC_{71}BM$ layer topped with a PCPDT-FBT-rich film is considered to be the best fitted model. The volume ratio fraction of polymer in the EAM mix film, the thickness of EMA mix layer, the thickness of the top PCPDT-FBT layer, and the surface roughness is set to be the fitting parameters. This model fitted very well with experimental data by giving MSEs of the fitted data with experimental data all less than 4. The calculated vertical composition profile is shown in Figure 5-13.

The top PCPDT-FBT-rich layers have a thickness of 3-5nm for different active layer films. The BHJ films have a volume content of PCPDT-FBT 34-35% throughout the layer, while the bilayer films contain less polymer content, which is 9.0% for conventional structure and 17.7% for the inverted structure by volume. This data is consistence with XPS depth profile of composition variation by weight percentage.

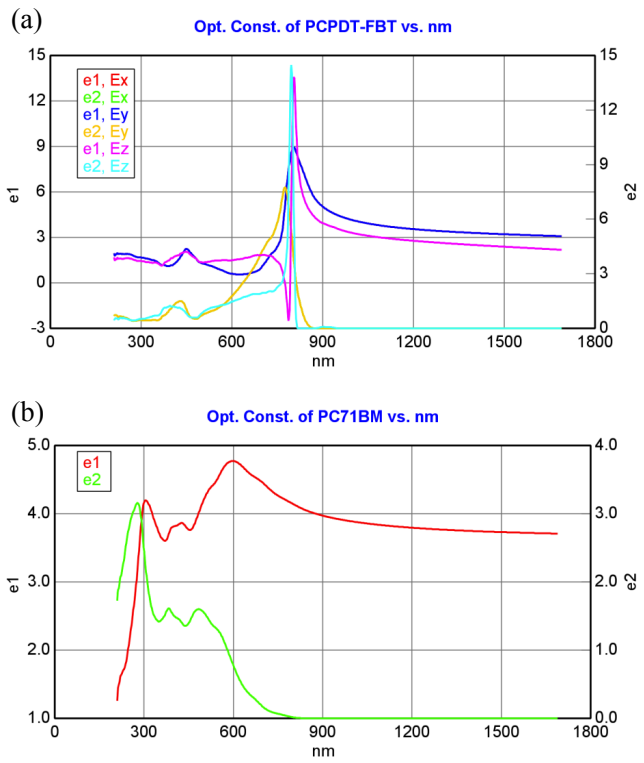

Figure 5-12 Dielectric function's real part ε1 and imaginary part ε2 of BHJ and bilayer films in conventional and inverted structure devices based on PCPDT-FBT and $PC_{71}BM$.

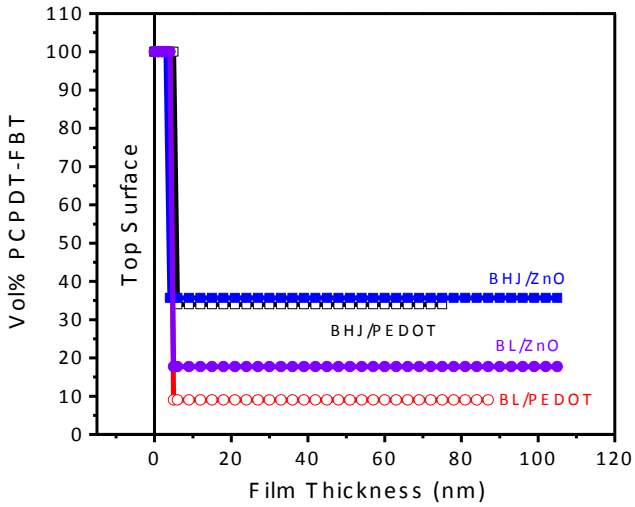

Figure 5-13 Ellipsometry determined depth profile of composition in BHJ and bilayer films in conventional and inverted structure devices based on PCPDT-FBT and PC71BM

5.3.3 *Better exciton dissociation/charge separation and collection in bilayer films*

5.3.3.1 SCLC mobility measurement

The charge transport properties in both the BHJ and bilayer structures were studied based on both hole-only devices with the configuration of ITO/PEDOT:PSS/BHJ/Pd and electron-only devices with the configuration of ITO/Al/BHJ/Ca/Al. Figure 5-14 shows the log scale J-V characteristics in the dark for both BHJ and bilayer devices. The J-V curves were fitted with the SCLC model to calculate both hole and electron mobilities. Pristine PCPDT-FBT polymer performs as a good hole transporting material, with a hole mobility of 6.85×10-4 cm2V-1s-1, and much lower electron mobility of 4.47×10-6 cm2V-1s-1. After spin casting PC71BM on top, the film shows bipolar characteristic with electron mobility increased to 1.80×10-4 cm2V-1s-1, and hole mobility also increased to1.89×10-3 cm2V-1s-1. The two orders of magnitude increasing in electron mobility is obviously contributed to the deposition and diffusion of PC71BM. Since SCLC is measuring charge mobility in a vertical direction, this is also evidence of PC71BM penetration into PCPDT-FBT film. The improved hole mobility can be attributed to the intercalation of PC71BM into polymer films. After PC71BM diffused into the PCPDT-FBT film, its intercalation between polymer side chains may inhibit the coiling of the polymer chains and therefore increase the conjugation length, intermolecular interactions, and thus improve the hole mobility.[15][16] After annealing, the hole mobility does not significantly change, which is calculated to be 2.64×10-3 cm2V-1s-1, while the electron mobility increased about 34 times compared to that of the film before annealing, which is 6.10×10-3 cm2V-1s-1. The increased electron mobility after annealing may be attributed to the further inter-diffusion and increased crystallinity of the fullerene. Since the electron and hole mobilities are on the same magnitude, a balanced charge transport is obtained in bilayer structure. As a comparison, the mobility of the

BHJ film has also been measured. The BHJ film has similar hole mobility as the bilayer film, which is 3.04×10-3 cm2V-1s-1. However, the electron mobility of 4.30×10-5 cm2V-1s-1 is significantly lower than that of the bilayer structure. The dramatically improved in electron mobility in bilayer film could be due to two reasons: first, the bilayer film shows a higher fullerene ratio than the BHJ film, which can contribute to the improvement of electron mobility. Second, the bilayer films are believed to have better continuity of charge transporting phases in vertical direction compared to BHJ films, which provides better electron transport pathways.

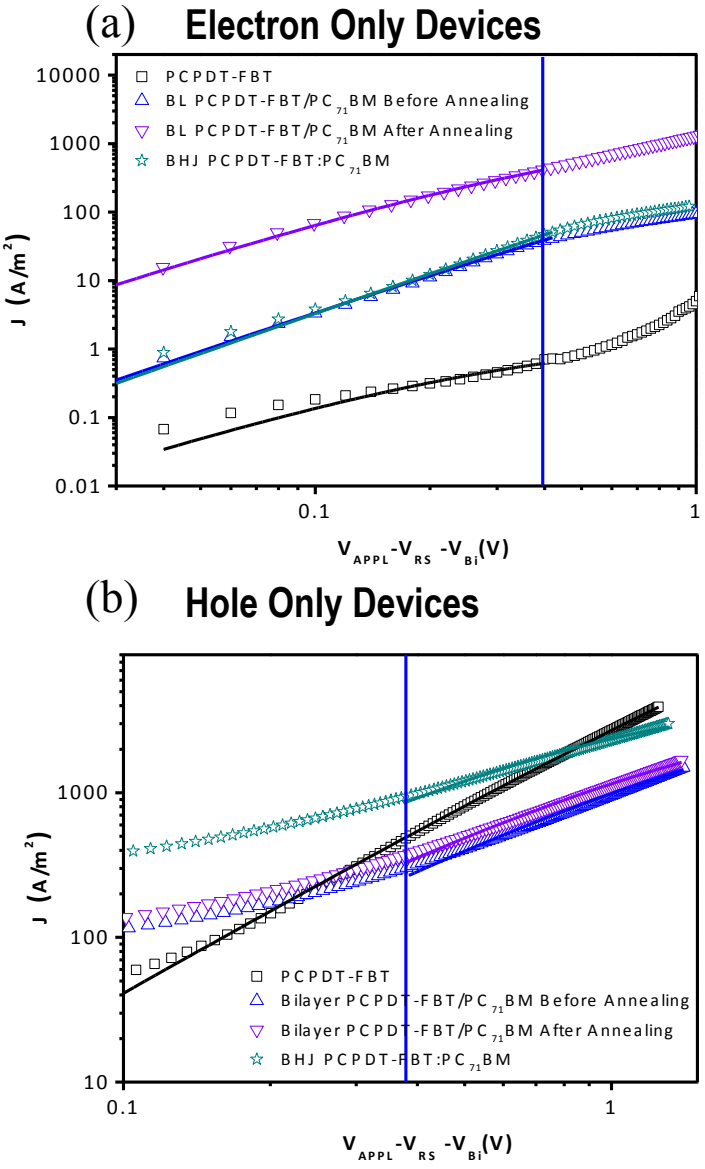

Figure 5-14 Measured J-V characteristics under dark for (a) electron-only and (b) hole-only devices consisting of pristine PCPDT-FBT, bilayer and BHJ films. The bias is corrected for built-in Voltage V_{Bi}, arising from difference in the work function of the contacts,

5.3.3.2 Polymer chain stacking indicated by UV-Vis absorption

Another factor that can contribute to the improved IQE in the bilayer structure can be attributed to the stronger π-π stacking of polymer chains. We have demonstrated that in the UV-Vis absorption spectrum of PCPDT-FBT, the peak at ~776nm is believed to be the result of π-π stacking. By normalizing the absorption of the active layer films and pristine PCPDT-FBT film at 722nm, as shown in

Figure 5-15, bilayer films clearly show a peak at ~776nm, but BHJ do not have any shoulder peak around that wavelength, no matter in a conventional or inverted structure. The bilayer film in inverted structure shows a stronger peak in this region, which may be due to the higher polymer ratio compare to that of the conventional structure. This phenomenon indicates the polymer chain stacking of the PCPDT-FBT is maintained even though PC71BM diffuses into the polymer film. When casting from a mixed solution of polymer and fullerene, the PCPDT-FBT chain stacking in the BHJ film is decreased by the presence of the PC71BM molecules, which may hinder the π−π stacking of the polymer chains.[185]

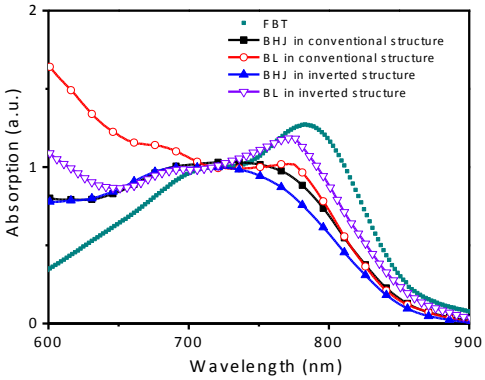

Figure 5-15 Normalized absorption spectrum of BHJ and bilayer films in conventional and inverted structure devices based on PCPDT-FBT and PC71BM, together with the pristine PCPDT-FBT film and PC71BM film.

Chapter 6. METAL GRID/CONDUCTING POLYMER HYBRID TRANSPARENT ELECTRODE FOR INVERTED POLYMER SOLAR CELLS [55]

6.1 INTRODUCTION

ITO is the most commonly used transparent metal oxide electrode because it offers good transparency in the visible range of the solar spectrum as well as good electrical conductivity. However, there are several deficiencies exist for using ITO as transparent conducting electrode such as poor mechanical properties of ITO-coated plastic substrates , limited conductivity for fabricating high-efficiency and large-area solar cells, limited availability of indium and complicated vacuum sputtering process [4] tend to increase the cost for ITO. These limitations set a potential barrier for the commercialization of low-cost organic solar cells. To alleviate this problem, alternative materials for transparent conducting electrode are needed to replace ITO. There has been some research on exploring conductive polymer [187], carbon nanotubes,[188] graphene[189], and silver nanowires[190] as potential candidates to replace ITO. However, lower transparency and higher sheet resistance compared to ITO strongly hinder their use for transparent electrode. Metal grids have also been investigated as a promising alternative for transparent electrode. [54][191] Utilizing microfluidic deposition and nanoimprinting methods, metal grids coated substrates have been used for fabricating conventional PSCs with PCE as high as 2% that can be achieved by optimizing the grid geometry and device configuration.

Previously, inverted architecture PSC without encapsulation using ITO and evaporated silver (Ag) as anode has been proved to be more stable in ambient than the conventional devices using sensitive metal on the top as cathode. [144] Moreover, poly(3,4-ethylenedioxythiophene):

poly(styrenesulfonate) (PEDOT:PSS) has also been demonstrated by Hau *et al.* as a potential replacement of ITO for fabricating inverted PSCs. [192] However, the relatively high sheet resistance of PEDOT:PSS compared to ITO may limited the performance of OPV devices The combination of conductive metal grids with PEDOT:PSS may provide a good solution to solve this problem and obtain ITO-free and ambient stable PSCs.

Here, we report a simple method to fabricate high-efficiency ITO-free inverted structure PSCs using a metal grid/conducting polymer hybrid transparent electrode. By using soft lithography and chemical etching, the metal grids can be easily fabricated on substrates. The inverted device architecture is used to fabricate PSCs with Ag as anode to collect holes and zinc oxide (ZnO) as an electron selective layer at the metal grid/conducting polymer interface to help collect electrons.

6.2 EXPERIMENTAL

To prepare the metal grids, 1 nm aluminum (Al) film was deposited first followed by evaporating a 30 nm thick silver film onto the glass substrates. It was found that the very thin Al layer improves adhesion between the substrate and the Ag film.

A micropatterned photoresist (SU-8, MicroChem) film, fabricated by standard photolithography, was used as a master to replicate stamps for microcontact printing (μCP). Masters were coated with a self-assembled monolayer of (1, 1, 2, 2-tetrahydroperfluorodecyl) trichlorosilane (Sigma-Aldrich) to ensure a clean release of the cured stamp. A typical stamp was made by casting a 10:1 (v/v) mixture of polydimethyl siloxane (PDMS) and curing agent (Sylgard 184, Dow Corning) against a silanized master in an oven at 60ºC for 20 hours. The PDMS stamp was first soaked with an “ink” containing 1 mM of mercaptoundecanoic acid

(MUA) in ethanol for 30s, then brought into contact with the surface of silver for 60 sec. After the removal of the stamp, the patterned Ag film was developed by wet etching with aqueous Fe^{3+}/thiourea using the patterned self-assembled monolayer (SAM) as resist.[193] MUA was chosen because it generates a hydrophilic surface that provides better wettability for the processing of upper layer film. In addition, MUA was found to promote ohmic contact between metal and metal oxide that facilitates better charge collection. [194] The scheme for the grid fabrication is shown in Figure 6-1 (a) Scheme of metal grids fabrication using micro-contact printing and wet chemical etching (b) Optical microscope image of silver grid with 5 μm width separated by a distance of 50 μm.(a).

Three types of design patterns were utilized in this study: 1) 5 μm width lines separated by a distance of 50 μm (5 μm/50 μm), 2) 10 μm width lines separated by a distance of 100 μm (10 μm/100 μm), and 3) 20 μm width lines separated by a distance of 200 μm (20 μm/200 μm). The optical transmittance of as-fabricated Ag grids was measured by UV-Vis spectroscopy between 250 and 1200 nm (Figure 6-2). The sheet resistance for metal grids with different geometry is also measured. For comparison, the sheet resistance and transmittance of a commercial ITO is also measured as control and included in the Figure. All transmittance measurements were referenced to air.

To fabricate solar cells, the ITO substrate and the metal grids coated substrate were cleaned sequentially with detergent, de-ionized water, acetone, and isopropyl alcohol. A thin layer of ZnO nanoparticles (ZnO NPs) synthesized using the method described by Beek et al. [195] was spin- coated onto these substrates. A C_{60}-based self-assembled monolayer (C_{60}-SAM) was then deposited onto the ZnO surface using a spin-coating process as reported previously.[144] A chlorobenzene solution comprising of poly (3-hexylthiophene) (P3HT) (Rieke Metals) and [6,6]

phenyl C_{61} butyric acid methyl ester (PCBM) (American Dye Source) (60 mg/ml) with a weight ratio of (1:0.7) was then spin-coated onto the C_{60}-SAM modified ZnO NP film in an argon-filled glove box. After being annealed at 160℃ for 10 min, a 200 nm-thick of P3HT:PCBM film was obtained. A 50 nm of PEDOT:PSS film ((H. C. Starck, **CLEVIOS^{TM}** P VP 408300) was then spin-coated onto the P3HT:PCBM layer and annealed as previously reported. [142] Finally, a layer of Ag was vacuum deposited on top of PEDOT:PSS as anode to complete the inverted device structure. The device architecture is shown in Figure 6-3.

The solar cells were tested under ambient using a Keithley 2400 SMU and an Oriel Xenon lamp (450 W) with an AM 1.5 filter. The light intensity was calibrated to 100 mW/cm^2 using a calibrated standard silicon solar cell with a KG5 filter, which was calibrated at the National Renewable Energy Laboratory.

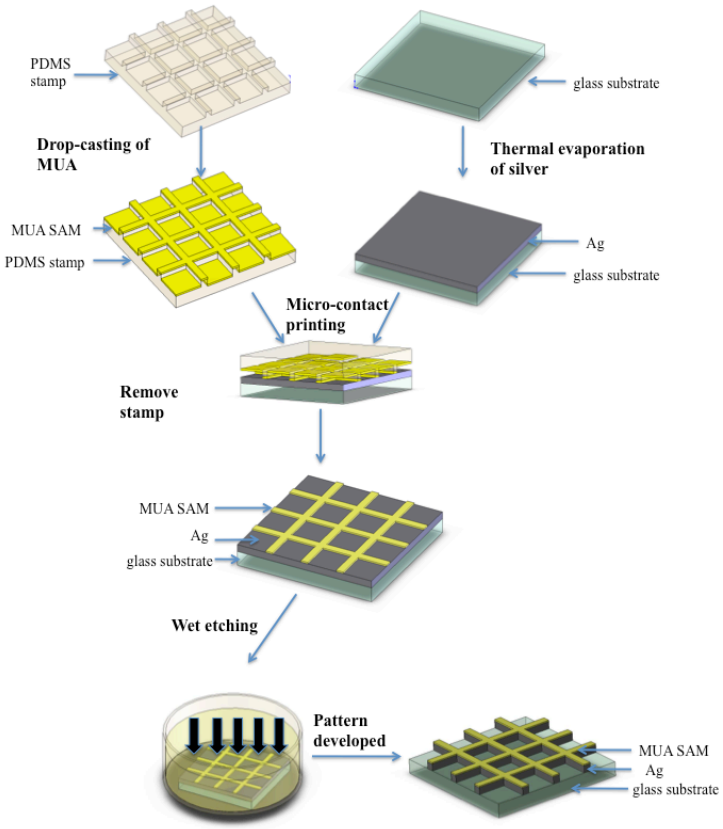

Figure 6-1 (a) Scheme of metal grids fabrication using micro-contact printing and wet chemical etching (b) Optical microscope image of silver grid with 5 μm width separated by a distance of 50 μm.

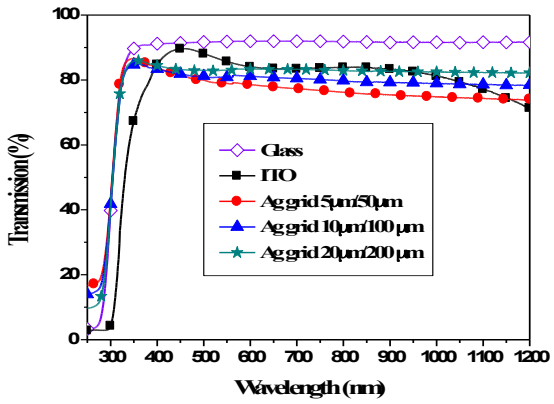

Figure 6-2 Transparency vs. wavelength of different geometry Ag grids on glass as compared to transparency of ITO and glass, as referenced against air.

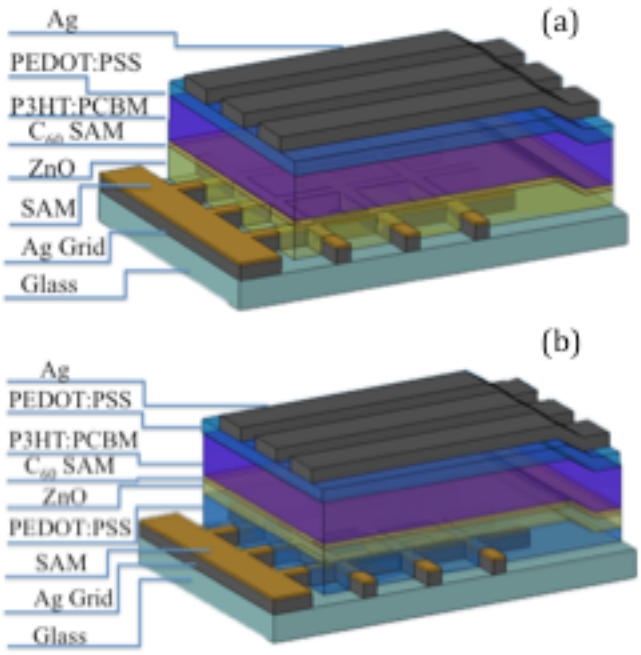

Figure 6-3 Device configuration of the polymer solar cell with (a) Ag grid and (b) Ag grid in combination with a conductive polymer PEDOT PH500 as the transparent electrode.

6.3 RESULTS AND DISCUSSION

The ITO control has a transmittance of 85.7% at 550nm. The aspect ratio of the metal lines (width to separation) of 1 to 10 was chosen to maximize the transmittance. When the transmittance of glass (~93%) is taken into account, the maximum expected transmittance of the metal grids coated glass substrate is calculated to be ~83-84%. It was found that the average transmittance of metal grid coated glass substrates in the range of 250-1200 nm is 78%, 80%, 82%, respectively for grids of 5 μm/50 μm, 10 μm/100 μm, and 20 μm/200 μm. The lower transmission may be due to some diffusion of MUA during contact printing on the metal surface, which leads to slight variation of grid geometry during the etching process. As the result, the actual Ag grid patterns expand 1-2 μm. Figure 2.2-1(b) shows the optical microscope images of an as-fabricated metal grid electrode on a glass substrate.

Another important parameter for transparent conducting electrodes is the sheet resistance. The commercial available ITO substrates have a sheet resistance of 15 Ω/ sq^{-1}, while the Ag grid electrodes exhibited sheet resistances of 9.1 Ω/sq^{-1}, 146.3 Ω/ sq^{-1}, and 254.1 Ω/ sq^{-1}, for 5 μm/50 μm, 10 μm/100 μm, and 20 μm/200 μm, respectively. Lower sheet resistances will minimize the loss of photocurrent during charge transport due to the lowered lateral resistance of the electrode. In general, the transmittance and sheet resistance for thin conductive films are related by the equation of

$$T(\lambda) = (1 + \frac{188.5}{R_s}\frac{\sigma_{op}(\lambda)}{\sigma_{DC}})^{-2}$$

Where $\sigma_{Op}(\lambda)$ is the optical conductivity (here we quoted at λ=550nm) and σ_{DC} is the conductivity of the film. $\sigma_{DC} / \sigma_{Op}$ is a commonly used term to describe transparent conductors.[25] For ITO with R_s of 15Ω/ sq^{-1} and T(550nm) of 85.7%, the $\sigma_{DC} / \sigma_{Op}$ is 156.7. The best results that have been achieved for the graphene-based films[26] and carbon nanotube[27] are 0.5 and 25,

respectively. Based on the best metal grid geometry used in this work (5 μm/50 μm), R_s = 9.1 Ω/ sq^{-1}, and T(550nm) = 79.0%, a σ_{DC}/σ_{Op} ratio as high as 165.6 could be achieved. This calculation has taken into account the absorption of glass.

The *J-V* characteristics under illumination and the solar cells performance are summarized in Figure 6-4 (a) and Table 6-1, respectively. The device with the 5 μm/50 μm Ag grid has an open-circuit voltage (V_{oc}) of 0.60 V, a short-circuit current density (J_{sc}) of 9.57 mA/cm^2, a fill factor of 0.52, and a PCE of 2.97%. The metal grid devices have comparable V_{oc} with those fabricated from the ITO substrate, however, the lower efficiency of the metal grid substrate derived device is mainly due to lower J_{sc} and fill factor, which decrease from 10.72 mA/cm^2 to 9.57 mA/cm^2, and 0.66 to 0.52, respectively.

An important parameter that needs to be considered for the design of metal grids in organic solar cells is that the charges generated from the voids between the grid lines need to be efficiently collected. The inverted device structure utilizes a ZnO NP layer as an electron selective layer between the active layer and the metal grids to collect electrons. Charges that are generated in the active layer needs to transport through the ZnO layer before being collected by the grid lines. The inhomogeneous and poor charge collection in the voids due to high sheet resistance of ZnO decrease both J_{sc} and fill factor. In addition, the lower transmittance of the 5 μm/50 μm Ag grids (~78%) compared to ITO (~85%) also contributes to the decrease of J_{sc}.

Increasing the width and separation while maintaining the same aspect ratio dramatically reduces the J_{sc} and fill-factor. The larger the separation between the metal lines, the less effective the charges can be extracted due to poor mobility and resistance of both the active layer and the ZnO layer. To alleviate the problem for poor charge collection, a PEDOT:PSS (H. C. Starck, **CLEVIOS™** PH 500) conducting polymer was inserted between the silver grids and the ZnO

layer to help collect electrons. A ~40 nm thick PEDOT:PSS film was spin-coated on top of the metal grids and annealed to form the hybrid electrode. The resulting device architecture is shown in Figure 2.3-1(b).

To demonstrate the function of the hybrid electrode, an inverted photovoltaic device with 220 nm thick PEDOT:PSS PH500 film without metal grids as the bottom electrode was fabricated to compare with the one with the hybrid electrode. The *J-V* characteristics under illumination and the solar cells performance are summarized in Figure 6-4 The current density-voltage (J-V) characteristics of polymer solar cells with (a) different Ag grids geometry (b) different Ag grids geometry combining 40nm PEDOT:PSS PH500 film measured under AM1.5 intensity of 100 mW cm-2(b) and Table 6-1, respectively. For the smaller separation Ag grids (5 μm/50 μm), the addition of the conducting PEDOT:PSS polymer layer improved the device performance to 3.21% due to the reduced lateral resistance. However, a slight decrease in J_{sc} is observed due to lower transparency of the electrode by inserting the PEDOT:PSS layer. For devices using larger separation grid lines (10 μm/100 μm and 20 μm/200 μm), the addition of the PEDOT:PSS layer significantly improved the performance of the devices. Grids with separation distance of over 10 μm cannot efficiently collect electrons with only a ZnO nanoparticle upper layer. The additional layer of PEDOT:PSS is necessary to reduce the lateral resistance so that charges can be transported from the ZnO layer to PEDOT:PSS and finally be collected by the metal electrodes. All three silver grids electrodes can achieve near 3% PCE using the additional PEDOT:PSS layer. The potential benefit of using larger size grid patterns is the ease for device fabrication especially for cost efficient industrial roll-to-roll processing. Without Ag grids, PEDOT:PSS PH 500 bottom electrode devices can only have efficiency of ~2.2% which is due to the lower fill factor caused by the high sheet resistance.

Table 6-1 Summary of PSCs performance with different Ag grids width and separation.

	V_{oc}	J_{sc}	FF	PCE	R_s	R_p
	(V)	(mA/cm^2)		(%)	($\Omega\ cm^2$)	($\Omega\ cm^2$)
ITO	0.61	10.72	0.66	4.35	0.9	780.2
Ag Grid 5μm/50μm	0.60	9.57	0.52	2.97	2.8	1341.6
Ag Grid 10μm/100μm	0.59	6.62	0.42	1.65	3.0	327.4
Ag Grid 20μm/200μm	0.58	4.33	0.49	1.00	3.1	322.1
Ag Grid 5μm/50μm -PEDOT	0.60	9.39	0.57	3.21	2.8	1118.0
Ag Grid 10μm/100μm - PEDOT	0.60	9.14	0.58	2.93	2.9	1213.2
Ag Grid 20μm/200μm - PEDOT	0.60	8.95	0.53	2.85	3.0	956.3
PEDOT	0.62	8.91	0.40	2.20	30.7	365.1

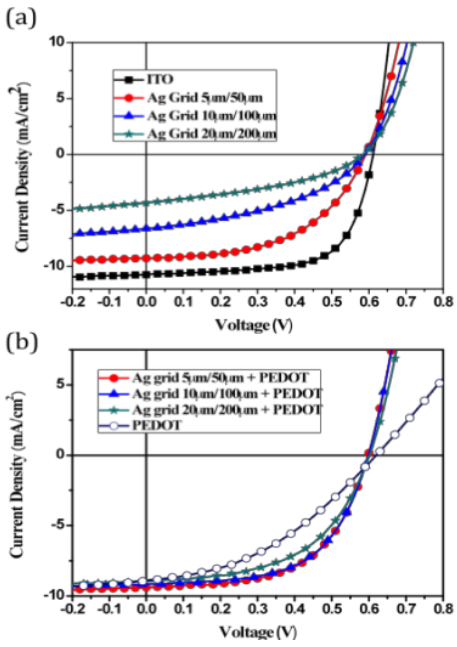

Figure 6-4 The current density-voltage (J-V) characteristics of polymer solar cells with (a) different Ag grids geometry (b) different Ag grids geometry combining 40nm PEDOT:PSS PH500 film measured under AM1.5 intensity of 100 mW cm-2

6.4 CONCLUSIONS

In conclusion, we have demonstrated that silver metal grid electrodes fabricated by micro-contact printing and wet chemical etching can replace conventional ITO electrodes for fabricating organic solar cells. The patterned metal electrodes on glass show high optical transmittance as well as good electrical conductivity. Organic solar cells with optimized grid geometry shows encouraging device performance. It was also found that silver grid electrodes with smaller width and separation with the same aspect ratio facilitated better charge collection from the ZnO NP layers leading to increased FF, J_{sc} and PCE. By adding a PEDOT:PSS PH500 conducting polymer between Ag grid and ZnO, even devices with larger Ag grid spacing can

achieve good performance. The use of inexpensive Ag grids compared to ITO allows the possibility of employing roll-to-roll process to realize low-cost, large-area organic solar cells.

Chapter 7. INTERFACIAL ENGINEERING OF ULTRA THIN METAL TRANSPARENT ELECTRODE IN FLEXIBLE ORGANIC PHOTOVOLTAIC CELLS

7.1 INTRODUCTION

Optoelectronic devices based on thin films of organic semiconductor have attracted substantial interests due to the potential to achieve flexible and lightweight devices by low cost processing. In particularly, one important class of the thin film optoelectronic devices is polymer solar cells (PSCs). PSCs is considered as a promising approach for economic alternative to energy conversion,[5][196][197] and has been rapidly developed with new light harvesting materials generation [110][198] and advanced architectures designed.[131][132][199]

Currently, Indium Tin Oxide (ITO) is the most commonly used commercial available transparent electrode, as it combines both high optical transparency in the visible range (~82%) and low resistivity (~10-20Ω/□ on glass). However, ITO is becoming one of the limiting factors for device performance as well as flexibility for the new generation optoelectronic devices, due to its limited conductivity on flexible substrates (~60Ω/□) and poor mechanical ductility. Plus, the price of ITO is increasing in recent years as a result of limited availability of indium.[45][46] Alternative materials for transparent electrode is necessary and has been widely studied, including other transparent conducting oxide,[47][48] carbon nanotubes,[49] graphene,[50] conducting polymers,[51][52] metal nanowires or meshes,[53] patterned metal grids,[54]–[57] and ultra thin metal films (UTMF).[58]–[61] But few of these electrodes have yielded devices that perform comparable to ITO. Among them, metal grids and UTMF combine the characteristics of high electrical conductivity as well as good mechanical ductility. Comparing with patterned metal

grids, the UTMF simplifies the processing without complicated patterning, thus offers large area deposition capability, and considered as the most viable candidate for ITO replacement. Within all metals attempted, silver is recognized as the best choice for UTMF due to its lowest resistivity (1.62μΩ cm), atmospherically stability, and extremely ductile (only surpassed by Au).

The optical transparency and conductivity of UTMFs highly depends on films thickness.[58] Transparency is exponentially decreased with film thickness, ~10nm or less is required for Ag films to achieve reasonable transparency for visible light. Meanwhile, Ag is known to prefer 3D island growth and therefore the percolation threshold of Ag layers deposited by thermal evaporation is also typically around 10-12nm nominal thickness.[200] The sheet resistance relies on the continuity of films and decreased with films thickness increasing. Thus, for the application of UTMFs as transparent electrode, it is critical to decrease the percolation threshold of Ag layers deposition, facilitate the continuous film formation, thus improve the film quality to get maximized transparency as well as minimized sheet resistance.

The quality of ultra thin Ag films is governed by the nucleation and growth kinetics of metal on substrate, and can be controlled by the seed layer and deposition conditions. It is known that the poor wettability of Ag on electrically insulating substrates (i.e., glass, Polyethylene naphthalate (PEN)) often leads to high resistance and poor transparency due to unfavorable disparity in surface energy and poor adhesion with the substrate.[61] An adequate seed layer is needed to improve the film quality for desired conductivity and optical quality. Deposit a seed layer of transparent metal oxide with low wetting angle for molten Ag is reported as one of the choices to circumvent this problem. In particularly, metal oxide / thin metal /metal oxide tri-layer structure has been realized as a promising way to improve the transparency due to interference effect.[60][201]–[203] A layer of molecules designed to enhance metal nucleation by interaction with

both the substrate and the incoming metal atom is also a way to suppress surface diffusion and promote the growth of continuous ultra thin metal films.[61]

Here, we demonstrate a novel protocol to prepare ultra thin silver films with extraordinary smooth surface, high conductivity and optically transparency, by combining metal oxide / thin metal / metal tri-layer structure with interfacial modification of designed molecule. Furthermore, to functioning the tri-layer structured UTMF as a platform for PSCs, sophisticated interfacial engineering method is applied at necessary interfaces, as which plays a critical roll in determining device performance.[7] With improved energy level alignment and electrical contact attributed from the interfacial modification, UTMFs with tri-layer structure were successfully integrated into PSCs with superior device performance that even exceeds using ITO as electrode, on both glass substrates and flexible substrates.

7.2 EXPERIMENTAL

The substrates (glass and ITO coated glass: Colorado Concept Coating LLC, PEN: Teonex Q65FA, ITO-coated plastic: Bayview Optics) were cleaned with detergent, de-ionized water, acetone, and isopropyl alcohol. After drying, the glass and ITO coated glass substrates were air-plasma treated for 20 seconds to remove any residual organic materials. ZnO precursor prepared using the method described by Sun *et al*. was spin-coated onto the pre-cleaned ITO-coated glass substrates, and films were annealed at 200°C (for glass) or 150°C (for PEN) for 1 hour in air. Self-assembled monolayer of MUA or lauric acid is deposited by spin coating form a 1mM solution of the molecules in ethanol, followed by rinsing with pure solvent of ethanol. Ag films of 10nm were applied by thermal evaporation at 5 Å s^{-1} at vacuum pressure < 10^{-6} torr. After thermal evaporation, another layer of MUA is spin coated as before. The transmission spectra of

the electrodes were measured in air by using a perkin-Elmer Lambda-9 UV/VIS spectrometer, while an Alessi four point probe was used to measure the sheet resistance.

ZnO precursor from zinc acetylacetonate hydrate (purchased from Aldrich and used as received) dissolved in ethanol (20 mg mL-1) is spin casted onto the pre-cleaned ITO surface and subsequently baked at 130 ºC for 10 min in air to achieve 20nm films. The substrates were then transferred into a nitrogen-filled glovebox. The C_{60}-SAM was deposited on the ZnO surface by spin coating from a 1mM solution of the molecules in tetrahydofuran(THF)/ chlorobenzene (CB) (1:1 *v*/*v*) followed by rinsing with pure THF solvent.Subsequently, PIDT-PhanQ:$PC_{71}BM$ active layer (ca. 70 nm) was spin-coated on the PEDOT:PSS layer from a homogeneous solution. The solution was prepared by dissolving the polymer and fullerene at weight ratios of 1:3.2 in o-dichlorobenzene overnight and filtered through a PTFE filter (0.2 μm). The substrates were annealed at 110 °C for 10 min prior to electrode deposition. At the final stage, the substrates were pumped down to high vacuum ($< 1 \times 10^{-6}$ Torr), and Molybdenum trioxide (5 nm) topped with silver (120 nm) was thermally evaporated onto the active layer.

The current-voltage (I-V) characteristics of unencapsulated photovoltaic devices were measured under ambient conditions using a Keithley 2400 source-measurement unit. An Oriel xenon lamp (450 Watt) with an AM1.5 G filter was used as the solar simulator. The light intensity was set to 1 sun (100 mW cm^{-2}) using a calibrated Hamamatsu silicon diode with a KG5 color filter, which can be traced to the National Renewable Energy Laboratory (NREL). The EQE system uses a lock-in amplifier (Stanford Research Systems SR830) to record the short-circuit current under chopped monochromatic light.

7.3 RESULTS AND DISCUSSION

To fabricate tri-layer structured UTMF, ZnO was utilized as metal oxide seed layer for Ag deposition due to its reasonable wetting angle for molten Ag and good transparent to visible light. Plus, it also allows easily solution processing over glass or plastic substrates, which makes it available for scaled up roll-to-roll processing in the future. With a seed layer of sol-gel-derived ZnO film, continuous silver film of 10nm can be thermally evaporated with sheet resistance of 13.59 Ω/□ and root-mean-square roughness of 2.68nm (Figure 7-1**(b)**). To further improve the quality of thin silver films, 11-mercaptoundecanoic acid (MUA) molecule was applied on top of sol-gel-derived ZnO here as the molecular adhesive for Ag deposition. Thiol functional group of MUA is well known to have a strong affinity for Ag, and carboxylic acid can couple with native hydroxyl groups on ZnO. MUA can be easily deposited on ZnO by simple and rapid spin coating method to form a self-assembled monolayer (SAM). This SAM layer modified the growth kinetics, producing highly conductive Ag films (8.61Ω/□) with a remarkable low root-mean-square roughness (0.59nm) (Figure 7-1 **(c)**). With the adhesion of MUA, the UTMF were exceptionally robust towards ultrasonic agitation with common cleaning solvents (Table 7-1), which makes UTMFs fabricated by this method potentially widely applicable for a variety of large area applications as a stable and ultra-smooth substrate electrodes.

As comparison, lauric acid was also applied on ZnO with $–CH_3$ terminal group towards Ag. Ag films on lauric acid modified ZnO with nominal thickness of 10nm gave sheet resistivity of 10.87Ω/□, but rough surface with root-mean-square roughness of 9.38nm is observed (Figure 7-1 (d)). Unlike the isolated island film morphology of Ag on glass, continuous Ag film has been formed here, which is revealed by the low sheet resistivity, yet the film coverage is un-homogenous, which can be clearly seen from AFM topography image. It has been reported in

UTMFs, the electrical conductivity shows no obvious correlation with film roughness, since the grain size, which could affect sheet resistivity, is defined by the ultra thin thickness. But for transparent electrode application, smoother surface is still favored since surface roughness could exacerbate scattering and increase the likelihood of parasitic current shunting in PSCs.[58]

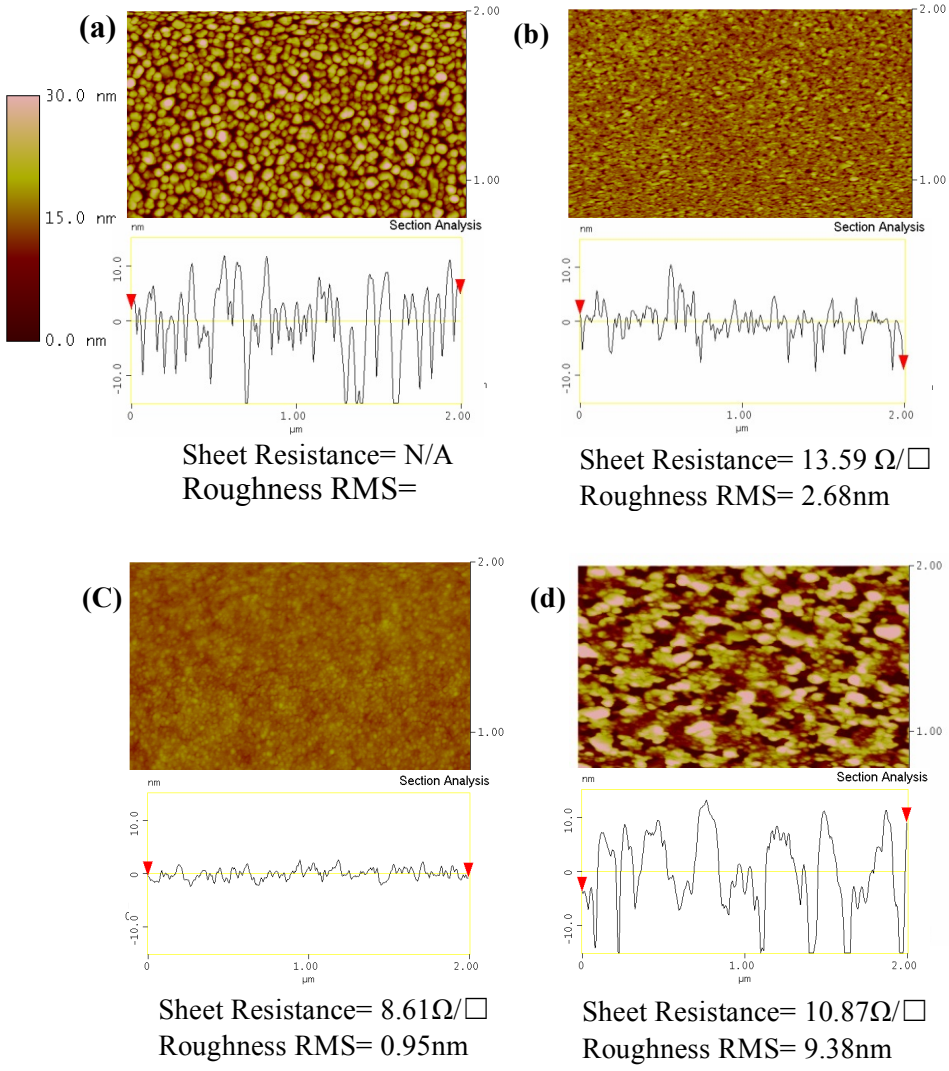

Figure 7-1 AFM images of ultra thin Ag films on top of (a) glass (b) glass/ZnO (c) glass / ZnO / MUA (d) glass/ZnO/Lauric acid

*Table 7-1 Sheet resistance **(Ω/□)** of Ag films supported on glass/ZnO substrates with and without the adhesion layer of MUA before and after ultrasonic agitation for 10 minutes in three common solvents and thermal annealing at 130°C for 5minutes.*

Electrode	After deposition	Sonication in water	Sonication in Acetone	Sonication in IPA	Annealing at 130°C
Without MUA	13.59	15.01	16.32	16.02	14.83
With MAU	8.61	8.92	8.43	8.60	7.21

To avoid oxidation and morphology change of thin Ag films by high temperature annealing in ambient, ZnO films with a low-temperature processing method[204] were capped on UTMFs to form the metal oxide / thin metal /metal oxide tri-layer structure. Transparency was tested for these tri-layer structured UTMFs, together with ITO on glass substrates as Figure 7-2 (a). With the same deposition condition and 10nm thickness as target, Ag films on glass with isolated island domains exhibited a dip at ~450nm due to the excitation of surface plasmons. Ag films on ZnO gave maximum transparency of 78% at 400nm with gradual decreasing as wavelength increased. A dip at ~450nm still can be observed, which possibly indicates un-completed coverage of Ag. By inserting an adhesion layer of MUA, the transparency of this tri-layer structured UTMF was enhanced by over 10% and achieved comparable transparency as ITO in the spectral range of 400nm $\leq \lambda \leq$ 600nm. The higher optical transparency could be due to dramatically reduced scattering as a result of exceptional smooth surface. In longer wavelength above 600nm, the spectral transmission is lower for this tri-layer structured UTMF compared to the ITO reference, due to its absorption and flection. However, reduced transmission of electrode does not always imply reduced absorption in light harvesting layer of PSCs. As we will show later, the increased reflection of UTMF helps to create a strong resonant cavity between the two silver electrodes, resulting in increased light harvesting in this lower transmission range. As a

contrast, a rougher silver film growth on lauric acid exhibited lower transparency attributed to the strong scatting.

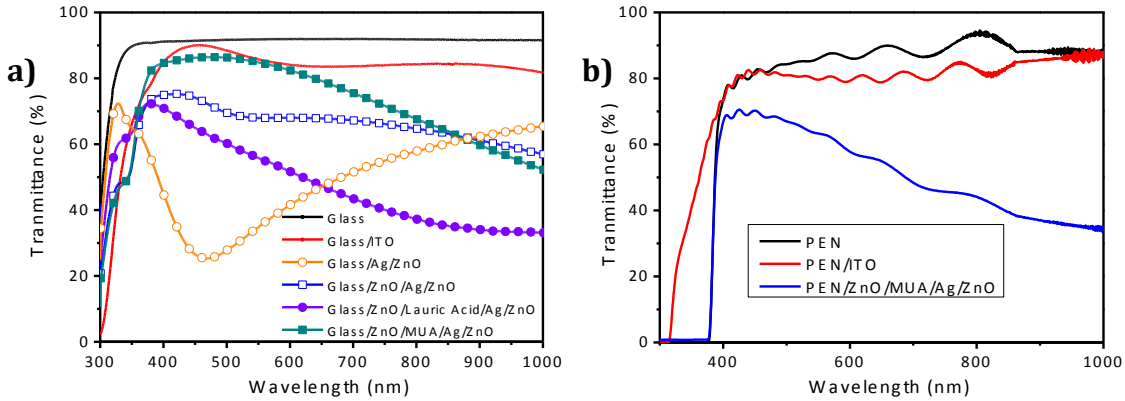

Figure 7-2 Transmission spectra of (a) UTMF electrodes on glass with different adhesion layers for Ag, together with glass and ITO (b) tri-layer structured UTMF electrode on PEN, together with glass and ITO

To illustrate the compatibility with flexible substrate, UTMFs with this tri-layer structure also have been fabricated in the same way on PEN. Similar sheet resistant of Ag films on PEN (9.00Ω/□) can be achieved as on glass substrates, which dramatically outperforms the 60Ω/□ for the ITO on PEN. A lower transmittance was observed compared with tri-layer structured UTMF on glass as Figure 7-2 **(b)**. The reasons for lower transmittance of UTMF on PEN could be: first, the optical transparency of PEN substrate fluctuates between 80% to 85%, which is lower than that of glass as 90%. In addition, the suggested continuous operating temperature of PEN is around 155° C, which requires a decreasing of the annealing temperature for sol-gel-derived ZnO seed layer. Thus, instead of 200° C processing, the sol-gel-derived ZnO seed films was annealed at 150° C, which resulted in lower refractive index of n~1.5, comparing with n~1.7 of 200°

processing, and results in a lower transparency of the tri-layer structured UTMFs with interference effect.

To demonstrate the viability of these UTMF electrodes as a direct replacement for ITO in PSCs, they were incorporated into devices based on the following device architecture: glass or PEN / ZnO (40nm) / Ag(10nm) / ZnO (20nm) / PIDT-PhanQ:$PC_{71}BM$ (70nm) / MoO3(5nm) / Ag (120nm) (Figure 7-3 **(a)**). The active layer was based on the bulk-heterojunction films of PIDT-PhanQ, which is a well characterized photoactive material system in our group and capable of delivering PCE over 6%.[99][162][205] The reference devices were made with the same device structure but using commercially available ITO-coated (120nm) glass substrates or PEN substrates as the transparent electrodes. By reversing the polarity of charge collection in the conventional structure, this inverted structure is widely recognized with better air stability.[142] At the same time, the top ZnO layer in tri-layer UTMF electrode perfectly fitted into the device architecture to serve as both an optical spacer as well as an electron transport layer.

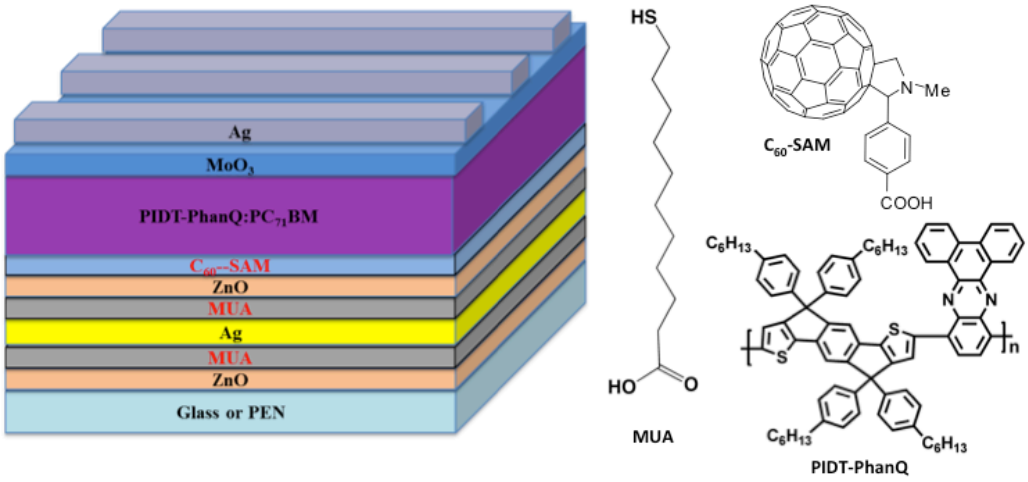

Figure 7-3 schematic structures of the PSC devices showing the order of the layers and molecular structure of MUA, C_{60}-SAM with photoactive material PIDT-PhanQ

To best utilized the tri-layer structured UTMF in this device architecture, except the MUA layer between the seed layer of ZnO and thin silver film, additional interface modification with designed SAMs also plays a critical role for optimized device performance. It was reported by our previous study that the unfavorable electrical contact between ZnO and Ag electrode would lead to a poor diode characteristic, and a monolayer of alkanethiols with dipole pointing away from the metal can decrease the work function of Ag to 3.8eV, the metal-sulfur bond also can decrease in contact resistance at the molecular junction.[41] Thus a layer of MUA was also employed here between Ag and top ZnO to tune the energy alignment by forming a favorable interfacial dipole. Also, a fullerene SAM with carboxylic acid functional group was inserted to the interface between top ZnO and BHJ to enhance electronic coupling of the inorganic/organic interface and improve charge selectivity.[144]

A summary of the electric parameters of the PSCs is shown in Table 7-2 and Figure 7-4 **(a)**. It is evident from these results that PSCs employing UTMF glass electrodes exhibited PCE higher than that of the devices employing ITO glass electrodes. Both open-circuit voltage (V_{oc}) and fill factor (FF) are similar in these two types of devices, while the short-circuit current (J_{sc}) with UTMF contributed to the performance improvement. External quantum efficiency was measured here (Figure 7-4 **(b)**) and dramatically spectral differences have been observed. In the spectral range $350nm \leq \lambda \leq 480nm$, the EQE for device on UTMF is lower than that on ITO. However, in the spectral range $480nm \leq \lambda \leq 700nm$, the solar cells employing UTMF electrode surpass ITO based devices with a peak value of 18% enhancement at $\lambda = 660nm$.

Table 7-2 Performance of devices with ITO electrodes and tri-layer structured UTMF electrodes on both glass and PEN substrates.

Electrode	V_{oc} [V]	J_{sc} [mA cm^{-2}]	FF	PCE [%]
ITO on glass (15Ω/□)	0.87	11.6	0.64	6.38
UTMF on glass (8.6Ω/□)	0.87	12.0	0.63	6.59
ITO on plastic (60Ω/□)	0.82	11.9	0.57	5.58
UTMF on plastic (9Ω/□)	0.87	11.0	0.64	6.04

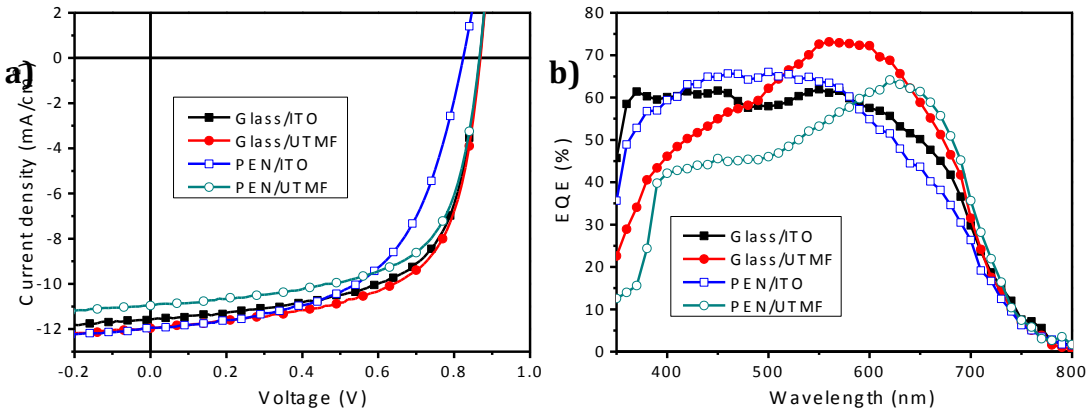

Figure 7-4 (a) J-V characteristics and (b) EQE of devices with ITO electrode and tri-layer structured UTMF electrode on both glass and PEN

Photon harvesting is closely related to the electric field intensity. Thus, to understand the EQE spectral changes, simulated field intensity profiles versus position and wavelength (Figure 7-6) for glass PSCs on UTMF and ITO were generated by transfer matrix formalism calculation respectively (the complex refractive index is shown in Figure 7-5). For device based on UTMF, a resonant cavity was formed between the two Ag electrodes in the spectral range of 600nm ≤ λ ≤ 720nm, which is appropriately in the absorption range of PIDT-PhanQ, with the intensity peak

spatially situated close to the center of BHJ films in vertical direction. This enhancement in optical field intensity lead the increase of photo harvesting in this spectral region, and resulted in the enhancement of EQE spectrum. For PSC on ITO electrode, no strong optical resonance was observed. Further, the light intensity absorption in photoactive layers (Figure 7-7) was also calculated based on transfer matrix formalism with electrode of UTMF and ITO. The simulation result clearly shows that the coherent light trapping results in a red shift of the absorption, and it has been translated into the EQE spectral.

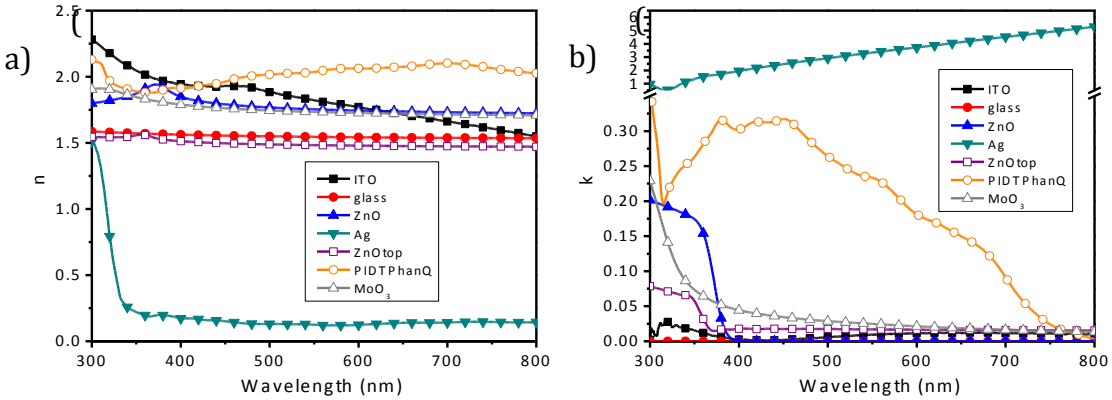

Figure 7-5 Complex index of refraction's (a) real part n and (b) imaginary part k

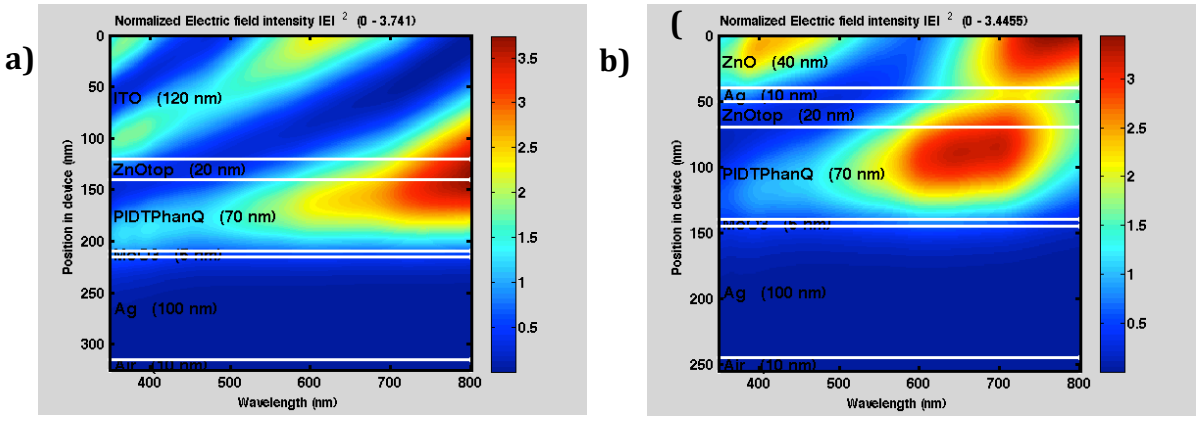

Figure 7-6 Electric field calculated by transfer matrix formalism considering a unitary incoming intensity for devices with (a) ITO cathode and (b) tri-layer structured UTMF cathode on glass substrates.

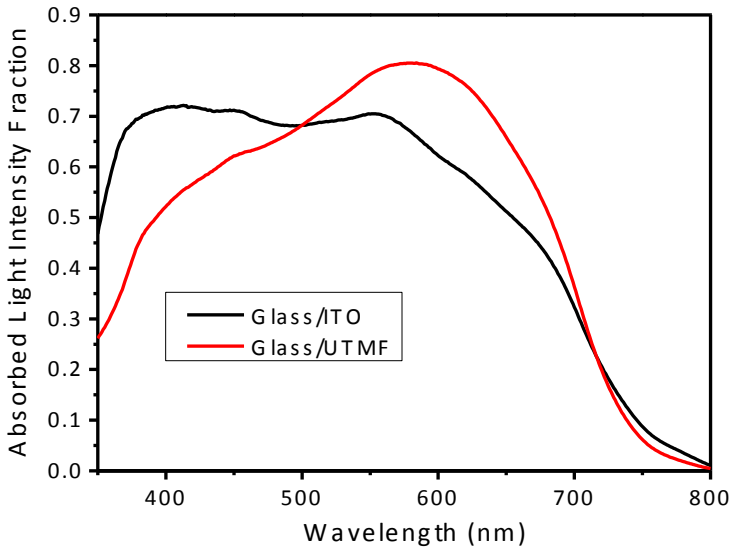

Figure 7-7 calculated light intensity absorption fractions of active layers by the transfer matrix formalism within device employing ITO cathode and tri-layer structured UTMF cathode.

Device performance on tri-layer structured UTMFs without appropriate interface modified has also been summarized in Table 7-3 and Figure 7-8. Without modify the interface between silver electrode and electron transporting layer of top ZnO, devices show a lower V_{oc} of 0.84V, and a dramatically decreasing of FF as of 0.56, which indicates the unflavored electrical contact. With the absence of C_{60}-SAM underneath BHJ film, the poor diode characteristic with all three electric parameters reduced proved that the C_{60}-SAM contributed to better electronic coupling of the inorganic/organic interface, mediate forward charge transfer and reduced charge recombination at the interface, which leads to improved photocurrent and charge selectivity.

Table 7-3 Performance of devices on tri-layer structured UTMF electrodes with and without interfacial modifications between Ag/top ZnO and top ZnO/BHJ.

Electrode	V_{oc} [V]	J_{sc} [mA cm^{-2}]	F F	PCE [%]
UTMF on glass (8.6Ω/□)	0.87	12.0	0.63	6.59
UTMF on glass without MUA	0.84	11.9	0.56	5.64
UTMF on glass without C60-SAM	0.82	11.4	0.56	5.23

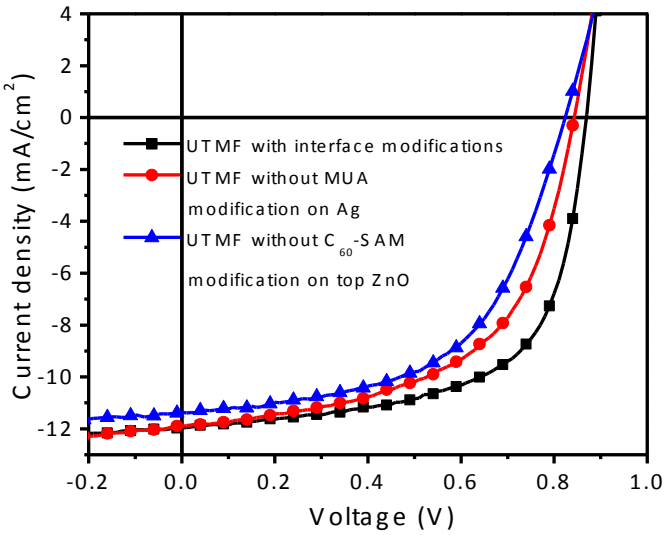

Figure 7-8 J-V characteristics of PSCs on tri-layer structured UTMF electrode with and without interfacial modifications between Ag/top ZnO and top ZnO/BHJ.

Comparing with the un-significant improvement from UTMF to ITO on glass substrates, on plastic substrates of PEN, devices with UTMF electrodes gave PCE of 6.04%, as devices with ITO electrodes only showed PCE of 5.64% (as **Table 1** and Figure 7-4**)**. Devices with UTMFs on PEN substrates showed lower optical transparency than plastic ITO, however, a significant

better conductivity is provided as (9.00Ω/□), comparing with 60Ω/□ of ITO. Thus, a lower J_{sc} of 11.0mA/cm^2 is observed, comparing to 11.9mA/cm^2 of devices employing ITO on PEN, and 12.0mA/cm^2 of devices with UTMF on glass, as a result of transparency decreasing. At the same time, the better conductivity of electrode contributes to the FF improvement from 0.57 to 0.64.

To evaluate possible degradation that may be caused by mechanical bending of flexible PSCs, a series of tests have been performed on devices with ITO and UTMF electrode on PEN using a cylinder (radius R = 0.55cm) to keep the same bending curvature, as shown in Figure 7-9. ITO based flexible PSCs exhibited a dramatic decrease of its performance starting from the first bending and continued to decrease when bending cycles proceed. Starting with PCE of 5.58%, ITO based flexible PSC degraded to 0.3% PCE after 200 bending cycles. In contrast, the performance of the device with UTMF electrode showed excellent stability even after 200 bending cycles, with limited changes of PCE from 6.04% to 5.58%. Thus, we proved that the tri-layer structured UTMFs affords much improved flexibility and compatibility with flexible substrates, as a result of the excellent ductile nature of thin metal films.

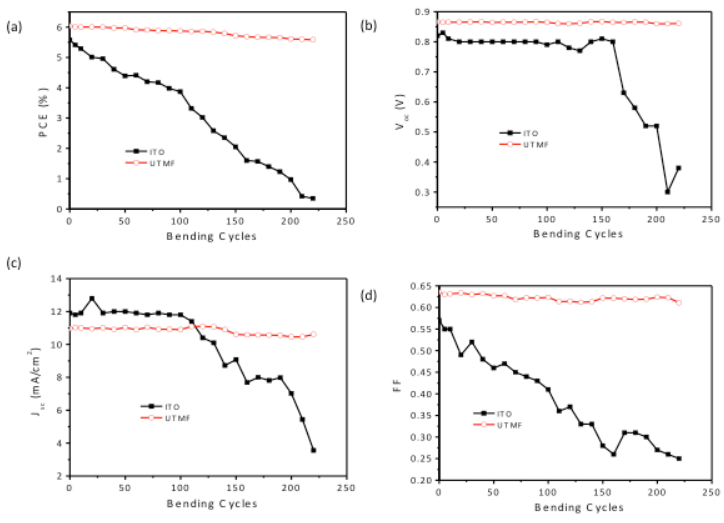

Figure 7-9 Effect of continuous bending over the (a) PCE and (b) V_{oc} (c) J_{sc} (d) FF of the flexible PSCs using both ITO and tri-layer structured UTMF electrodes.

7.4 CONCLUSIONS

In conclusion, we have developed a rapid and simple method for the fabrication of highly transparent ultra thin silver films on both glass and plastic substrates, based on ZnO/Ag/ZnO tri-layer structure and self-assembled monolayer interfacial modification. The resulting films are highly transparent (>80% 400-600nm) and electrically conductive (8.61Ω/□) with a remarkable low surface roughness. With appropriate device architecture and interface engineering, PSCs with tri-layer structured UTMFs achieved performance higher than those with ITO electrode on both glass and plastic substrates. The flexible devices on UTMFs also showed excellent bending stability compared to devices fabricated on ITO electrodes. The EQE of these cells revealed the superior device performances attributed to the coherent light trapping effect in devices with UTMF electrodes.

REFERENCE

[1] C.J. Brabec, J.R. Durrant, *MRS Bulletin* **2008**, *33*, 670.

[2] S.E. Shaheen, D.S. Ginley, Gh.E. Jabbour, *MRS Bulletin* **2005**, *30*, 11.

[3] E. Bundgaard, F.C. Krebs, *Sol. Energy Mater. Sol. Cells* **2007**, *91*, 954–985.

[4] D. Ginley, M.A. Green, R. Collins, *Mrs Bulletin* **2008**, *33*, 355–364.

[5] *ASTM G173-03: Standard Tables for Reference Solar Spectral Irradiances: Direct Normal and Hemispherical on 37° Tilted Surface*

[6] B.C. Thompson, J.M.J. Frechet, *Angew. Chem. Int. Ed* **2008**, *47*, 58.

[7] V. Shrotriya, G. Li, Y. Yao, T. Moriarty, K. Emery, Y. Yang, *Advanced Functional Materials* **2006**, *16*, 2016–2023.

[8] H.-L. Yip, A.K.-Y. Jen, *Energy & Environmental Science* **2012**, *5*, 5994.

[9] G. Li, R. Zhu, Y. Yang, *Nature Photonics* **2012**, *6*, 153–161.

[10] X. Yang, J. Loos, *Macromolecules* **2007**, *40*, 1353–1362.

[11] C.W. Tang, *Applied Physics Letters* **1986**, *48*, 183.

[12] S.-H. Chan, Y.-S. Hsiao, L.-I. Hung, G.-W. Hwang, H.-L. Chen, C. TIng, C.-P. Chen, *Marcomolecules* **2010**.

[13] H. Hoppe, M. Niggemann, C. Winder, J. Kraut, R. Hiesgen, A. Hinsch, D. Meissner, N.S. Sariciftci, *Advanced Functional Materials* **2004**, *14*, 1005–1011.

[14] J.K. van Duren, X. Yang, J. Loos, C.W. Bulle-Lieuwma, A.B. Sieval, J.C. Hummelen, R.A. Janssen, *Advanced Functional Materials* **2004**, *14*, 425–434.

[15] G. Dennler, A.J. Mozer, G. Ju\vska, A. Pivrikas, R. Österbacka, A. Fuchsbauer, N.S. Sariciftci, *Organic Electronics* **2006**, *7*, 229–234.

[16] A.C. Mayer, M.F. Toney, S.R. Scully, J. Rivnay, C.J. Brabec, M. Scharber, M. Koppe, M. Heeney, I. McCulloch, M.D. McGehee, *Advanced Functional Materials* **2009**, *19*, 1173–1179.

[17] N.C. Cates, R. Gysel, J.E.P. Dahl, A. Sellinger, M.D. McGehee, *Chem. Mater.* **2010**, *22*, 3543–3548.

[18] J. Huang, G. Li, Y. Yang, *Applied Physics Letters* **2005**, *87*, 112105–112105.

[19] G. Li, S. Vishal, J. Huang, Y. Yao, T. Moriarty, K. Emery, Y. Yang, *Nat. Mater.* **2005**, *4*, 864.

[20] S.E. Shaheen, C.J. Brabec, N.S. Sariciftci, F. Padinger, T. Fromherz, J.C. Hummelen, *Appl. Phys. Lett.* **2001**, *78*, 841.

[21] X. Yang, J.K. van Duren, R.A. Janssen, M.A. Michels, J. Loos, *Macromolecules* **2004**, *37*, 2151–2158.

[22] T. Martens, J. D'Haen, T. Munters, Z. Beelen, L. Goris, J. Manca, M. D'Olieslaeger, D. Vanderzande, L. De Schepper, R. Andriessen, *Synthetic Metals* **2003**, *138*, 243–247.

[23] Y. Yang, *Adv. Func. Mater.* **2007**, *17*, 1636.

[24] H. Hoppe, M. Drees, W. Schwinger, F. Schaffler, N.S. Sariciftcia, *Synthetic Metals* **2005**, *152*, 117.

[25] M. Reyes-Reyes, K. Kim, J. Dewald, R. López-Sandoval, A. Avadhanula, S. Curran, D.L. Carroll, *Organic Letters* **2005**, *7*, 5749–5752.

[26] X. Yang, J. Loos, S.C. Veenstra, W.J.H. Verhees, M.M. Wienk, J.M. Kroon, M.A.J. Michels, R.A.J. Janssen, *Nano Lett.* **2005**, *5*, 579–583.

[27] Y. Zhao, Z. Xie, Y. Qu, Y. Geng, L. Wang, *Applied Physics Letters* **2007**, *90*, 043504–043504.

[28] V.D. Mihailetchi, H. Xie, B. de Boer, L.M. Popescu, J.C. Hummelen, P.W.M. Blom, L.J.A. Koster, *Appl. Phys. Lett.* **2006**, *89*, 012107.

[29] J. Peet, J.Y. Kim, N.E. Coates, W.L. Ma, D. Moses, A.J. Heeger, G.C. Bazan, *Nat. Mater.* **2007**, *6*, 497–500.

[30] J.K. Lee, W. li Ma, C.J. Brabec, J. Yuen, J.S. Moon, J.Y. Kim, K. Lee, G.C. Bazan, A.J. Heeger, *JACS* **2008**, *130*, 3619.

[31] C.V. Hoven, X.-D. Dang, R.C. COffin, J. Peet, T.-Q. Nguyen, G.C. Bazan, *Adv. Mater.* **2010**, *22*, E63.

[32] Y. Yao, J. Hou, Z. Xu, G. Li, Y. Yang, *Adv. Func. Mater.* **2008**, *18*, 1783.

[33] L.A.A. Pettersson, L.S. Roman, O. Inganas, *J. Appl. Phys.* **1999**, *86*, 487.

[34] P. Peumans, A. Yakimov, S.R. Forrest, *J. Appl. Phys.* **2003**, *93*, 3693.

[35] S. Albrecht, S. Schäfer, I. Lange, S. Yilmaz, I. Dumsch, S. Allard, U. Scherf, A. Hertwig, D. Neher, *Organic Electronics* **2012**, *13*, 615–622.

[36] Y. Long, *Solar Energy Materials and Solar Cells* **2011**, *95*, 3400–3407.

[37] T. Ameri, G. Dennler, C. Waldauf, P. Denk, K. Forberich, M.C. Scharber, C.J. Brabec, K. Hingerl, *J. Appl. Phys.* **2008**, *103*, 084506.

[38] F.C. Chen, J.L. Wu, Y. Hung, *Appl. Phys. Lett.* **2010**, *96*, 193304.

[39] L.-M. Chen, Z. Xu, Z. Hong, Y. Yang, *J. Mater. Chem.* **2010**.

[40] Z. Xu, L.-M. Chen, G. Yang, C.-H. Huang, J. Hou, Y. Wu, G. Li, C.-S. Hsu, Y. Yang, *Adv. Func. Mater.* **2009**, *19*, 1227.

[41] M. Campoy-Quiles, T. Ferenczi, T. Agostinelli, P.G. Etchegoin, Y. Kim, T.D. Anthopoulos, P.N. Stavrinou, D.D.C. Bradley, J. Nelson, *Nat Mater* **2008**, *7*, 158–164.

[42] H.-L. Yip, S.K. Hau, N.S. Baek, A.K.-Y. Jen, *Applied Physics Letters* **2008**, *92*, 193313–193313.

[43] H.-L. Yip, S.K. Hau, N.S. Baek, H. Ma, A.K.-Y. Jen, *Advanced Materials* **2008**, *20*, 2376–2382.

[44] B. Bulliard, S.-G. Ihn, S. Yun, Y. Kim, D. Choi, J.-Y. Choi, M. Kim, M. Sim, J.-H. Park, W. Choi, K. Cho, *Adv. Func. Mater.* **2011**, *20*, 4381.

[45] S.K. Hau, H.-L. Yip, H. Ma, A.K.-Y. Jen, *Appl. Phys. Lett.* **2008**, *93*, 233304.

[46] O. Inganäs, *Nature Photonics* **2011**, *5*, 201–202.

[47] C.G. Granqvist, *Solar Energy Materials and Solar Cells* **2007**, *91*, 1529–1598.

[48] E. Fortunato, D. Ginley, H. Hosono, D.C. Paine, *Mrs Bulletin* **2007**, *32*, 242–247.

[49] H. Kim, J.S. Horwitz, W.H. Kim, A.J. Mäkinen, Z.H. Kafafi, D.B. Chrisey, *Thin Solid Films* **2002**, *420*, 539–543.

[50] R.C. Tenent, T.M. Barnes, J.D. Bergeson, A.J. Ferguson, B. To, L.M. Gedvilas, M.J. Heben, J.L. Blackburn, *Advanced Materials* **2009**, *21*, 3210–3216.

[51] J. Wu, H.A. Becerril, Z. Bao, Z. Liu, Y. Chen, P. Peumans, *Applied Physics Letters* **2008**, *92*, 263302–263302.

[52] Z. Tang, L.M. Andersson, Z. George, K. Vandewal, K. Tvingstedt, P. Heriksson, R. Kroon, M.R. Andersson, O. Inganäs, *Advanced Materials* **2012**, *24*, 554–558.
[53] Y. Xia, K. Sun, J. Ouyang, *Advanced Materials* **2012**.
[54] J.-Y. Lee, S.T. Connor, Y. Cui, P. Peumans, *Nano Letters* **2008**, *8*, 689–692.
[55] K. Tvingstedt, O. Inganäs, *Advanced Materials* **2007**, *19*, 2893–2897.
[56] J. Zou, H.-L. Yip, S.K. Hau, A.K.-Y. Jen, *Appl. Phys. Lett.* **2010**, *96*, 203301.
[57] D.S. Ghosh, T.L. Chen, V. Pruneri, *Applied Physics Letters* **2010**, *96*, 041109.
[58] M.-G. Kang, M.-S. Kim, J. Kim, L.J. Guo, *Advanced Materials* **2008**, *20*, 4408–4413.
[59] B. O'Connor, C. Haughn, K.-H. An, K.P. Pipe, M. Shtein, *Applied Physics Letters* **2008**, *93*, 223304.
[60] J.-F. Salinas, H.-L. Yip, C.-C. Chueh, C.-Z. Li, J.-L. Maldonado, A.K.-Y. Jen, *Advanced Materials* **2012**, ASAP.
[61] N.P. Sergeant, A. Hadipour, B. Niesen, D. Cheyns, P. Heremans, P. Peumans, B.P. Rand, *Advanced Materials* **2012**, *24*, 728–732.
[62] H.M. Stec, R.J. Williams, T.S. Jones, R.A. Hatton, *Advanced Functional Materials* **2011**, *21*, 1709–1716.
[63] Y. Zhang, J. Zou, H.-L. Yip, Y. Sun, J.A. Davies, K.-S. Chen, O. Acton, A.K.-Y. Jen, *Journal of Materials Chemistry* **2011**, *21*, 3895.
[64] J. Chen, Y. Cao, *Acc. Chem. Res.* **2009**, *42*, 1709–1718.
[65] Y.-J. Cheng, S.-H. Yang, C.-S. Hsu, *Chem. Rev.* **2009**, *109*, 5868.
[66] J. Hou, H.Y. Chen, S. Zhang, G. Li, Y. Yang, *J. Am. Chem. Soc.* **2008**, *130*, 16144–16145.
[67] E. Wang, L. Wang, L. Lan, C. Luo, W. Zhuang, J. Peng, Y. Cao, *Applied Physics Letters* **2008**, *92*, 033307–033307.
[68] J. Peet, J.Y. Kim, N.E. Coates, W.L. Ma, D. Moses, A.J. Heeger, G.C. Bazan, *Nat Mater* **2007**, *6*, 497–500.
[69] D. Muhlbacher, M. Scharber, M. Morana, Z. Zhu, D. Waller, R. Gaudiana, C. Brabec, *Adv. Mater.* **2006**, *18*, 2884.
[70] A.J. Moulé, A. Tsami, T.W. Bünnagel, M. Forster, N.M. Kronenberg, M. Scharber, M. Koppe, M. Morana, C.J. Brabec, K. Meerholz, *Chemistry of Materials* **2008**, *20*, 4045–4050.
[71] I.H. Jung, H. Kim, M.-J. Park, B. Kim, J.-H. Park, E. Jeong, H.Y. Woo, S. Yoo, H.-K. Shim, *Journal of Polymer Science Part A: Polymer Chemistry* **2010**, *48*, 1423–1432.
[72] J. Hou, H.Y. Chen, S. Zhang, G. Li, Y. Yang, *Journal of the American Chemical Society* **2008**, *130*, 16144–16145.
[73] M.C. Scharber, M. Koppe, J. Gao, F. Cordella, M.A. Loi, P. Denk, M. Morana, H.-J. Egelhaaf, K. Forberich, G. Dennler, R. Gaudiana, D. Waller, Z. Zhu, X. Shi, C.J. Brabec, *Adv. Mater.* **2010**, *22*, 367–370.
[74] E. Zhou, Q. Wei, S. Yamakawa, Y. Zhang, K. Tajima, C. Yang, K. Hashimoto, *Macromolecules* **2009**, *43*, 821–826.

[75] E. Zhou, M. Nakamura, T. Nishizawa, Y. Zhang, Q. Wei, K. Tajima, C. Yang, K. Hashimoto, *Macromolecules* **2008**, *41*, 8302.

[76] G. Zhang, Y. Fu, Q. Zhang, Z. Xie, *Chemical Communications* **2010**, *46*, 4997–4999.

[77] C.H. Woo, P.M. Beaujuge, T.W. Holcombe, O.P. Lee, J.M. Fréchet, *Journal of the American Chemical Society* **2010**, *132*, 15547.

[78] Y. Zou, A. Najari, P. Berrouard, S. Beaupré, B. Réda Aïch, Y. Tao, M. Leclerc, *Journal of the American Chemical Society* **2010**, *132*, 5330–5331.

[79] Y. Zhang, S.K. Hau, H.-L. Yip, Y. Sun, O. Acton, A.K.-Y. Jen, *Chem. Mater.* **2010**, *22*, 2696.

[80] J.K. Lee, W.L. Ma, C.J. Brabec, J. Yuen, J.S. Moon, J.Y. Kim, K. Lee, G.C. Bazan, A.J. Heeger, *J. Am. Chem. Soc.* **2008**, *130*, 3619–3623.

[81] J.S. Moon, C.J. Takacs, S. Cho, R.C. Coffin, H. Kim, G.C. Bazan, A.J. Heeger, *Nano Letters* **2010**.

[82] Ro.C. Coffin, J. Peet, J. Rogers, G.C. Bazan, *Nature Chemistry* **2009**, *1*, 657.

[83] H. Hoppe, N.S. Sariciftci, *J. Mater. Chem.* **2006**, *16*, 45.

[84] Y. Zhang, J. Zou, H.-L. Yip, K.-S. Chen, D.F. Zeigler, Y. Sun, A.K.-Y. Jen, *Chemistry of Materials* **2011**, *23*, 2289–2291.

[85] W. Zhang, J. Smith, S.E. Watkins, R. Gysel, M. McGehee, A. Salleo, J. Kirkpatrick, S. Ashraf, T. Anthopoulos, M. Heeney, I. Mcculloch, *Journal of the American Chemical Society* **2010**, *132*, 11437.

[86] C.-P. Chen, S.-H. Chan, T.-C. Chao, C. Ting, B.-T. Ko, *Journal of the American Chemical Society* **2008**, *130*, 12828.

[87] Y.-C. Chen, C.-Y. Yu, Y.-L. Fan, L.-I. Hung, C.-P. Chen, C. Ting, *Chemical Communications* **2010**, *46*, 6503–6505.

[88] S.-H. Chan, C.-P. Chen, T.-C. Chao, C. Ting, C.-S. Lin, B.-T. Ko, *Macromolecules* **2008**, *41*, 5519–5526.

[89] J. Zhang, W. Cai, F. Huang, E. Wang, C. Zhong, S. Liu, M. Wang, C. Duan, Ti. Yang, Y. Cao, *Macromolecules* **2011**, *44*.

[90] E. Zhou, J. Cong, K. Tajima, K. Hashimoto, *Chemistry of Materials* **2010**, *22*, 4890.

[91] L.J. Lindgren, F. Zhang, M. Andersson, S. Barrau, S. Hellström, W. Mammo, E. Perzon, O. Inganäs, M.R. Andersson, *Chemistry of Materials* **2009**, *21*, 3491.

[92] E. Wang, L. Hou, Z. Wang, S. Hellström, F. Zhang, O. Inganäs, M.R. Andersson, *Advanced Materials* **2010**, *22*, 5240–5244.

[93] F. Zhang, J. Bijleveld, E. Perzon, K. Tvingstedt, S. Barrau, O. Inganäs, M.R. Andersson, *Journal of Materials Chemistry* **2008**, *18*, 5468–5474.

[94] A. Gadisa, W. Mammo, L.M. Andersson, S. Admassie, F. Zhang, M.R. Andersson, O. Inganäs, *Advanced Functional Materials* **2007**, *17*, 3836–3842.

[95] Y. Liang, Y. Wu, D. Feng, S.-T. Tsai, H.-J. Son, G. Li, L. Yu, *J. Am. Chem. Soc.* **2009**, *131*, 56.

[96] T.M. Clarke, J.R. Durrant, *Chem. Rev.* **2010**, 222.

[97] M.C. Scharber, C.J. Brabec, *Adv. Mater.* **2006**, *18*, 789.

[98] Y. Zhang, J. Zou, H.-L. Yip, K.-S. Chen, J.A. Davies, Y. Sun, A.K.-Y. Jen, *Macromolecules* **2011**, *44*, 4752–4758.

[99] S. Günes, H. Neugebauer, N.S. Sariciftci, *Chem. Rev.* **2007**, *107*, 1324–1338.

[100] Y. Zhang, J.Y. Zou, H.L. Yip, K.S. Chen, D.F. Zeigler, Y. Sun, A.K.. Jen, *J. Mater. Chem.* **2011**, *23*, 2289.

[101] M.M. Wienk, J.M. Kroon, W.J. Verhees, J. Knol, J.C. Hummelen, P.A. van Hal, R.A. Janssen, *Angewandte Chemie* **2003**, *115*, 3493–3497.

[102] C.J. Brabec, A. Cravino, D. Meissner, N.S. Sariciftci, T. Fromherz, M.T. Rispens, L. Sanchez, J.C. Hummelen, *Advanced Functional Materials* **2001**, *11*, 374–380.

[103] D. Veldman, S.C. Meskers, R.A. Janssen, *Advanced Functional Materials* **2009**, *19*, 1939–1948.

[104] B.P. Rand, D.P. Burk, S.R. Forrest, *Physical Review B* **2007**, *75*, 115327.

[105] K. Vandewal, K. Tvingstedt, A. Gadisa, O. Inganäs, J.V. Manca, *Nature Materials* **2009**, *8*, 904–909.

[106] C. He, C. Zhong, H. Wu, R. Yang, W. Yang, F. Huang, G.C. Bazan, Y. Cao, *J. Mater. Chem.* **2010**, *20*, 2617–2622.

[107] J. Luo, H. Wu, C. He, A. Li, W. Yang, Y. Cao, *Applied Physics Letters* **2009**, *95*, 043301–043301.

[108] N. Blouin, A. Michaud, D. Gendron, S. Wakim, E. Blair, R. Neagu-Plesu, M. Belletête, G. Durocher, Y. Tao, M. Leclerc, *Journal of the American Chemical Society* **2008**, *130*, 732–742.

[109] Y. Zhang, J. Zou, C.-C. Cheuh, H.-L. Yip, A.K.-Y. Jen, *Macromolecules* **2012**, *45*, 5427–5435.

[110] H.-Y. Chen, J. Hou, S. Zhang, Y. Liang, Y. Liang, G. Yang, Y. Ynag, L. Yu, Y. Wu, G. Li, *Nat. Photonics* **2009**, *3*, 649.

[111] Y. Liang, Z. Xu,, J. Xia, S.-T. Tsai, Y. Wu, G. Li, C. Ray, L. Yu, *Adv. Mater.* **2010**, *22*, E135.

[112] T.-Y. Chu, J. Lu, S. Beaupre, Y. Zhang, J.-R. Pouliot, S. Wakim, J. Zhou, M. Leclerc, Z. Li, J. Ding, Y. Tao, *J. Am. Chem. Soc.* **2011**, *133*, 4250.

[113] C. Piliego, T.W. Holcombe, J.D. Douglas, C.H. Woo, P.M. Beaujuge, J.M.J. Fréchet, *J. Am. Chem. Soc.* **2010**, *132*, 7595–7597.

[114] M.-S. Su, C.-Y. Kuo, M.-C. Yuan, U.-S. Jeng, C.-J. Su, K.-H. Wei, *Adv. Mater.* **2011**, *23*, 3315–3319.

[115] L. Huo, J. Hou, S. Zhang, H.-Y. Chen, Y. Yang, *Angew. Chem. Int. Ed* **2010**, *49*, 1500.

[116] Z. Zhu, D. Waller, R. Gaudiana, M. Morana, D. Mühlbacher, M. Scharber, C. Brabec, *Macromolecules* **2007**, *40*, 1981–1986.

[117] F.C. Krebs, *Solar Energy Materials and Solar Cells* **2009**, *93*, 1636–1641.

[118] H. Zhou, L. Yang, A.C. Stuart, S.C. Price, S. Liu, W. You, *Angew. Chem. Int. Ed.* **2011**, *50*, 2995–2998.

[119] S.C. Price, A.C. Stuart, L. Yang, H. Zhou, W. You, *J. Am. Chem. Soc.* **2011**, *133*, 4624.

[120] S. Alem, T.-Y. Chu, S.C. Tse, S. Wakim, J. Lu, R. Movileanu, Y. Tao, F. Belanger, D. Desilets, S. Beaupré, M. Leclerc, S. Rodman, D. Waller, R. Gaudiana, *Organic Electronics* **2011**, *12*, 1788.

[121] W. Cai, M. Wang, J. Zhang, E. Wang, T. Yang, C. He, J.S. Moon, H. Wu, X. Gong, Y. Cao, *The Journal of Physical Chemistry C* **2011**, *115*, 2314.

[122] K. Kawano, J. Sakai, M. Yahiro, C. Adachi, *Solar Energy Materials and Solar Cells* **2009**, *93*, 514.

[123] C.M. Amb, S. Chen, K.R. Graham, J. Subbiah, C. e. Small, F. So, J.R. Reynolds, *J. Am. Chem. Soc.* **2011**, *133*, 10062.

[124] C.-D. Park, T.A. Fleetham, J. Li, B.D. Vogt, *Organic Electronics* **2011**, *12*, 1465–1470.

[125] C.N. Hoth, R. Steim, P. Schilinsky, S.A. Choulis, S.F. Tedde, O. Hayden, C.J. Brabec, *Organic Electronics* **2009**, *10*, 587–593.

[126] J. Zhao, A. Swinnen, G. Van Assche, J. Manca, D. Vanderzande, B.V. Mele, *The Journal of Physical Chemistry B* **2009**, *113*, 1587–1591.

[127] Z. He, C. Zhang, X. Xu, L. Zhang, L. Huang, J. Chen, H. Wu, Y. Cao, *Adv. Mater.* **2011**, *23*, 3086–3089.

[128] Z. He, C. Zhong, X. Huang, W.-Y. Wong, H. Wu, L. Chen, S. Su, Y. Cao, *Advanced Materials* **2011**, *23*, 4636–4643.

[129] J.H. Seo, A. Gutacker, Y. Sun, H. Wu, F. Huang, Y. Cao, U. Scherf, A.J. Heeger, G.C. Bazan, *Journal of the American Chemical Society* **2011**, *132*, 8416.

[130] K.M. O'Malley, C.-Z. Li, H.-L. Yip, A.K.-Y. Jen, *Advanced Energy Materials* **2011**, *2*, 82–86.

[131] Y. Li, J. Zou, H.-L. Yip, Y. Zhang, C. Li, C.-C. Chueh, J. Intermann, Y. Xu, P.-W. Liang, Y. Chen, A.K.-Y. Jen, *Macromolecules* **n.d.**, *Submitted*.

[132] Z. He, Ch. Zhong, S. Su, M. Xu, H. Wu, Y. Cao, *Nat. Photonics* **2012**, *6*, 591.

[133] L. Dou, J. You, J. Yang, C.-C. Chen, Y. He, S. Murase, T. Moriarty, K. Emery, G. Li, Y. Yang, *Nature Photonics* **2012**, *6*, 180–185.

[134] V.S. Gevaerts, A. Furlan, M.M. Wienk, M. Turbiez, R.A.J. Janssen, *Advanced Materials* **2012**, *24*, 2130–2134.

[135] W. Li, W.C. Roelofs, M.M. Wienk, R.A. Janssen, *Journal of the American Chemical Society* **2012**.

[136] H.N. Tsao, D.M. Cho, I. Park, R.H. Michael, A. Mavrinskiy, D.Y. Yoon, R. Graf, W. Pisula, H.W. Spiess, K. Müllen, *Journal of the American Chemical Society* **2011**, *133*, 2605.

[137] T. Lei, J.-H. Dou, J. Pei, *Advanced Materials* **n.d.**, *24*, 5347.

[138] L. Yang, J.R. Tumbleston, H. Zhou, H. Ade, W. You, *Energy & Environmental Science* **2013**, *6*, 316.

[139] A. Gadisa, W.D. Oosterbaan, K. Vandewal, J.-C. Bolsée, S. Bertho, J. D'Haen, L. Lutsen, D. Vanderzande, J.V. Manca, *Advanced Functional Materials* **2009**, *19*, 3300–3306.

[140] Z. Li, S.-W. Tsang, X. Du, L. Scoles, G. Robertson, Y. Zhang, F. Toll, Y. Tao, J. Lu, J. Ding, *Advanced Functional Materials* **2011**, *21*, 3331–3336.

[141] B. Burkhart, P.P. Khlyabich, B.C. Thompson, *Macromolecules* **2012**, *45*, 3740–3748.

[142] J. Zou, H.-L. Yip, Y. Zhang, Y. Gao, S.-C. Chien, K. O'Malley, C.-C. Chueh, H. Chen, A.K.-Y. Jen, *Advanced Functional Materials* **2012**, n/a–n/a.

[143] S.K. Hau, H.-L. Yip, N.S. Baek, J. Zou, K. O'Malley, A.K.-Y. Jen, *Appl. Phys. Lett.* **2008**, *92*, 253301.
[144] S.K. Hau, H.-L. Yip, O. Acton, N.S. Baek, H. Ma, A.K.-Y. Jen, *J. Mater. Chem.* **2008**, *18*, 5113.
[145] S.K. Hau, H.-L. Yip, H. Ma, A.K.-Y. Jen, *Appl. Phys. Lett.* **2008**, *93*, 233304.
[146] T. Ameri, G. Dennler, C. Waldauf, A. Hamed, A. Seemann, K. Forberich, J. Hauch, M. Scharber, K. Hingerl, C.J. Brabec, *Adv. Func. Mater.* **2010**, *20*, 1592.
[147] K.-S. Chen, Y. Zhang, H.-L. Yip, Y. Sun, J.A. Davies, C. Ting, C.-P. Chen, A.K.-Y. Jen, *Org. Electron.* **2011**, *Accepted*.
[148] C.-H. Hsieh, Y.-J. Cheng, P.-J. Li, C.-H. Chen, M. Dubosc, R.-M. Liang, C.-S. Hsu, *J. Am. Chem. Soc.* **2010**, *132*, 4887–4893.
[149] Y.-J. Cheng, C.-H. Hsieh, Y. He, C.-S. Hsu, Y. Li, *J. Am. Chem. Soc.* **2010**, *132*, 17381.
[150] S. Yanming, J. Seo, Ch.J. Takacs, J. Seifter, Heeger Alan J, *Adv. Mater.* **2011**, *23*, 1679.
[151] W.J.E. Beek, M.M. Wienk, M. Kemerink, X. Yang, R.A.J. Janssen, *J. Phys. Chem. B* **2005**, *109*, 9505–9516.
[152] G.F. Burkhard, E.T. Hoke, M.D. McGehee, *Adv. Mater.* **2010**, *22*, 3293.
[153] Y. Gao, H.-L. Yip, S.K. Hau, K.M. O'Malley, N.C. Cho, H. Chen, A.K.-Y. Jen, *Appl. Phys. Lett.* **2010**, *97*, 203306.
[154] Y. Gao, H.-L. Yip, K.-S. Chen, K.M. O'Malley, O. Acton, Y. Sun, G. Ting, H. Chen, A.K.-Y. Jen, *Adv. Mater.* **2011**, *23*, 1903.
[155] S.K. Hau, H.L. Yip, J.Y. Zou, A.K.. Jen, *Org. Electron.* **2009**, *10*, 1401–1407.
[156] G. Dennler, M.C. Scharber, C.J. Brabec, *Adv. Mater.* **2009**, *21*, 1323.
[157] C.J. Brabec, N.S. Sariciftci, J.C. Hummelen, *Adv. Func. Mater.* **2001**, *11*, 15.
[158] F.C. Krebs, *Organic Electronics* **2009**, *10*, 761–768.
[159] J. Chen, Y. Cao, *Accounts of Chemical Research* **2009**, *42*, 1709–1718.
[160] J.J.M. Halls, C.A. Walsh, N.C. Greenham, E.A. Marseglia, R.H. Friend, S.C. Moratti, *Nature* **1995**, *376*.
[161] G. Yu, J. Gao, J.C. Hummelen, F. Wudl, A.J. Heeger, *Science* **1995**, *270*, 1789.
[162] Y. Sun, S.-C. Chien, H.-L. Yip, K.-S. Chen, Y. Zhang, J.A. Davies, F.-C. Chen, B. Lin, A.K.-Y. Jen, *Journal of Materials Chemistry* **2012**, *22*, 5587.
[163] K.-S. Chen, H.-L. Yip, C.W. Schlenker, D.S. Ginger, A.K.-Y. Jen, *Organic Electronics* **2012**, *13*, 2870–2878.
[164] Y. Zhang, H.-L. Yip, O. Acton, S.K. Hau, F. Huang, A.K.-Y. Jen, *Chemistry of Materials* **2009**, *21*, 2598–2600.
[165] D.S. Germack, C.K. Chan, R.J. Kline, D.A. Fischer, D.J. Gundlach, M.F. Toney, L.J. Richter, D.M. DeLongchamp, *Macromolecules* **2010**, *43*, 3828–3836.
[166] W.-R. Wu, U.-S. Jeng, C.-J. Su, K.-H. Wei, M.-S. Su, M.-Y. Chiu, C.-Y. Chen, W.-B. Su, C.-H. Su, A.-C. Su, *ACS Nano* **2011**.
[167] S.S.V. Bavel, M. Barenklau, G. de With, H. Hoppe, J. Loos, *Adv. Func. Mater.* **2010**, *20*, 1458.

[168] A.J. Moule, K. Meerholz, *Adv. Func. Mater.* **2009**, *19*, 3028.
[169] K.H. Lee, P.E. Schwenn, A.R.G. Smith, H. Cavaye, P.E. Shaw, M. James, K.B. Krueger, I.R. Gentle, P. Meredith, P.L. Burn, *Adv. Mater.* **2011**, *23*, 766–770.
[170] A.L. Ayzner, C.J. Tassone, S.H. Tolbert, B.J. Schwartz, *J. Phys. Chem. C* **2009**, *113*, 20050–20060.
[171] J.S. Moon, C.J. Takacs, Y. Sun, A.J. Heeger, *Nano Lett.* **2011**.
[172] D.H. Wang, J.S. Moon, J. Seifter, J. Jo, J.H. Park, O.O. Park, A.J. Heeger, *Nano Lett.* **2011**, *11*, 3163.
[173] C. Rochester, S.A. Mauger, A.J. Moule, *J. Phys. Chem. C* **2012**.
[174] V.S. Gevaerts, L.J.A. Koster, M.M. Wienk, R.A.J. Janssen, *ACS Appl. Mater. Interfaces* **2011**, *3*, 3252.
[175] D. Chen, F. Liu, C. Wang, A. Nakahara, T.P. Russell, *Nano Lett.* **2011**, *11*, 2071.
[176] D.H. Wang, D.-G. Choi, K.-J. Lee, O.O. Park, J.H. Park, *Langmuir* **2010**, *26*, 9584–9588.
[177] D.H. Wang, H.K. Lee, D.-G. Choi, J.H. Park, O.O. Park, *Applied Physics Letters* **2009**, *95*, 043505.
[178] D.H. Wang, J.K. Kim, O.O. Park, J.H. Park, *Energy & Environmental Science* **2011**, *4*, 1434.
[179] N.D. Treat, M.A. Brady, G. Smith, M.F. Toney, E.J. Kramer, C.J. Hawker, M.L. Chabinyc, *Advanced Energy Materials* **2011**, *1*, 82–89.
[180] K. Vandewal, K. Tvingstedt, A. Gadisa, O. Inganäs, J.V. Manca, *Nature Materials* **2009**, *8*, 904–909.
[181] G.F. Burkhard, E.T. Hoke, S.R. Scully, M.D. McGehee, *Nano Lett.* **2009**, *9*, 4037–4041.
[182] Y. Vaynzof, D. Kabra, L. Zhao, L.L. Chua, U. Steiner, R.H. Friend, *ACS Nano* **2010**.
[183] M.V. Madsen, K.O. Sylvester-Hvid, B. Dastmalchi, K. Hingerl, K. Norrman, T. Tromholt, M. Manceau, D. Angmo, F.C. Krebs, *The Journal of Physical Chemistry C* **2011**.
[184] D. Bruggeman, *Ann. Phys.* **1935**, *416*, 665–679.
[185] D.M. DeLongchamp, R.J. Kline, D.A. Fischer, L.J. Richter, M.F. Toney, *Advanced Materials* **2011**, *23*, 319–337.
[186] A. Swinnen, I. Haeldermans, P. Vanlaeke, J. D'Haen, J. Poortmans, M. D'Olieslaeger, J.V. Manca, *The European Physical Journal Applied Physics* **2006**, *36*, 251–256.
[187] J. Cui, A. Wang, N.L. Edleman, J. Ni, P. Lee, N.R. Armstrong, T.J. Marks, *Adv. Mater.* **2001**, *13*, 1476.
[188] S.-I. Na, S.-S. Kim, J. Jo, D. Kim, *Adv. Mater.* **2008**, *20*, 4061.
[189] M.W. Rowell, M.A. Topinka, M.D. McGehee, H.-J. Prall, G. Dennler, N.S. Sariciftci, L. Hu, G. Gruner, *Appl. Phys. Lett.* **2006**, *88*, 233506.
[190] G. Eda, Y.-Y. Lin, S. Miller, C.-W. Chen, W.-F. Su, M. Chhowalla, *Appl. Phys. Lett.* **2008**, *92*, 233305.
[191] J.-Y. Lee, S.T. Connor, Y. Cui, P. Peumans, *Nano Lett.* **2008**, *8*, 689–692.
[192] M.-G. Kang, M.-S. Kim, J. Kim, L.J. Guo, *Adv. Mater.* **2008**, *20*, 4408.
[193] S.K. Hau, H.-L. Yip, J. Zou, A.K.-Y. Jen, *Org. Electron.* **2009**, *10*, 1401.

[194] J.M. McLellan, M. Geissler, Y. Xia, *J. Am. Chem. Soc.* **2004**, *126*, 10830–10831.
[195] H.-L. Yip, S.K. Hau, N.S. Baek, A.K.-Y. Jen, *Appl. Phys. Lett.* **2008**, *92*, 193313.
[196] W.J.E. Beek, M.M. Wienk, M. Kemerink, X. Yang, R.A.J. Janssen, *J. Phys. Chem. B* **2005**, *109*, 9505–9516.
[197] G. Dennler, M.C. Scharber, C.J. Brabec, *Advanced Materials* **2009**, *21*, 1323–1338.
[198] C.J. Brabec, S. Gowrisanker, J.J.M. Halls, D. Laird, S. Jia, S.P. WIlliams, *Adv. Mater.* **2010**, *22*, 3839.
[199] Y.-X. Xu, C.-C. Chueh, H.-L. Yip, F.-Z. Ding, Y.-X. Li, C.-Z. Li, X. Li, W.-C. Chen, A.K.-Y. Jen, *Advanced Materials* **2012**, *24*, 5356–6361.
[200] T. Ameri, G. Dennler, C. Lungenschmied, C.J. Brabec, *Energy Environ. Sci.* **2009**, *2*, 347.
[201] R.S. Sennett, G.D. Scott, *JOSA* **1950**, *40*, 203–210.
[202] J.C.C. Fan, *Applied Physics Letters* **1974**, *25*, 693.
[203] H. Cho, C. Yun, J.-W. Park, S. Yoo, *Organic Electronics* **2009**, *10*, 1163–1169.
[204] D.R. Sahu, J.-L. Huang, *Thin Solid Films* **2006**, *515*, 876–879.
[205] C.-Y. Chang, Y.-J. Cheng, S.-H. Hung, J.-S. Wu, W.-S. Kao, C.-H. Lee, C.-S. Hsu, *Advanced Materials* **2012**, *24*, 549–553.
[206] J. Zou, H.-L. Yip, Y. Zhang, Y. Gao, S.-C. Chien, K. O'Malley, C.-C. Chueh, H. Chen, A.K.-Y. Jen, *Advanced Functional Materials* **2012**, *22*, 2804–2811.